IOP Publishing Reports on Progress in Physics
Rep. Prog. Phys. **77** (2014) 106901 (49pp) doi:10.1088/0034-4885/77/10/106901

Review Article

Indirect techniques in nuclear astrophysics: a review

R E Tribble[1], **C A Bertulani**[2], **M La Cognata**[3], **A M Mukhamedzhanov**[1] **and C Spitaleri**[3,4]

[1] Cyclotron Institute, Texas A&M University, College Station, TX 77843, USA
[2] Department of Physics, Texas A&M University-Commerce, Commerce, TX 75429, USA
[3] Istituto Nazionale di Fisica Nucleare, Laboratori Nazionali del Sud, 95123 Catania, Italy
[4] Dipartimento di Fisica e Astronomia, Università di Catania, 95123 Catania, Italy

E-mail: r-tribble@tamu.edu

Received 19 February 2014, revised 4 August 2014
Accepted for publication 20 August 2014
Published 13 October 2014

Abstract

In this review, we discuss the present status of three indirect techniques that are used to determine reaction rates for stellar burning processes, asymptotic normalization coefficients, the Trojan Horse method and Coulomb dissociation. A comprehensive review of the theory behind each of these techniques is presented. This is followed by an overview of the experiments that have been carried out using these indirect approaches.

Keywords: nuclear reactions, stellar burning, explosive hydrogen burning

(Some figures may appear in colour only in the online journal)

1. Introduction

Understanding the origin of the elements is one of the key scientific questions facing researchers in nuclear physics and astronomy in the twenty first century. Intimately tied to this is the issue of stellar evolution and the fate of objects as close to our world as our Sun. Over 70 years ago, the concept that hydrogen and helium burning are the sources for energy production in stars was postulated by Bethe (1939). A byproduct of this burning process is the production of new elements. We know today that a large number of different reactions are involved in element production, many of which take place on rather short-lived nuclei during explosive processes that occur in the cosmos. For over 50 years, experimentalists have worked to quantify stellar reaction rates on systems involving stable beams and stable targets. Until rather recently, very little experimental information was available for reaction rates on radioactive nuclei. This is now changing with the development of new indirect techniques to determine these rates and new radioactive beam facilities that are expanding the possibilities for both direct and indirect studies.

Nucleosynthesis in the Universe, i.e. the ‘cooking’ processes that produce the elements of the periodic chart (Weizsäcker 1937), proceeds through a variety of reactions and decays such as (p,γ), (n,γ), (^{3}He,γ), (α,γ), (p,α), (α,p), (n,α), (α,n), beta decays, reactions induced by gamma-quanta (photodisintegration), and neutrinos. Determining the rates of these processes at stellar energies is the major part of the subject of nuclear astrophysics.

Many of the important stellar reactions occur in cycles, as described by Rolfs and Rodney (1988). These cycles are typically ones that burn hydrogen through proton-γ capture reactions and beta decays. The carbon–nitrogen–oxygen, or CNO, cycle is an example of a cycle that occurs once carbon is produced in a star. The CNO cycle reactions produce much more heat from burning hydrogen than the p–p chain reactions, which are the reactions in the first stage of hydrogen burning. The increased energy production heats up the star and can eventually lead to even more rapid burning through the hot-CNO cycle. This is typically the first step in a thermal runaway that eventually produces new nuclei through explosive hydrogen burning. Similar cycles of reactions occur for helium burning and also can lead to explosive processes.

0034-4885/14/106901+49$88.00

The conditions under which the majority of astrophysical reactions proceed in stellar environments make it difficult or impossible to measure them under the same conditions in the laboratory. For example, the astrophysical reactions between charged nuclei occur at energies much lower than the Coulomb barrier, which often makes the cross section of the reaction too small to measure. This is due to the very small barrier penetration factor from the Coulomb force, which produces an exponential fall off of the cross section as a function of energy. Many years ago, the astrophysical S-factor was adopted as a way to characterize cross sections by removing the Coulomb penetration factor based on an s-wave, or zero angular momentum capture. The S-factor, $S(E)$, is defined through the relationship

$$\sigma(E) = E^{-1}\exp(-2\pi\eta)S(E). \tag{1.1}$$

where $\sigma(E)$ is the energy dependent cross section and $\eta = (Z_1Z_2e^2/\hbar)\sqrt{\mu/2E}$ with Z being the charges of the two nuclei, E the relative kinetic energy of the interacting particles, and μ their reduced mass. For an s-wave capture reaction, the S-factor is nearly independent of energy and is typically the quantity that is used to extrapolate to low energies. For the reactions that cannot be measured directly, the quantities to determine are the energies and strengths of the resonant states that contribute to the reaction rate and the normalization of the tail of the overlap function.

Typically reactions that are of interest for nuclear astrophysics are measured in the laboratory at energies much higher than those relevant to stellar processes. As noted above, an extrapolation down to stellar energies must then be done. In this way, rates are predicted for reactions in the region of interest, the so-called Gamow window (for details on this see Rolfs and Rodney (1988)), which is the name for the energy window that results in the maximum reaction rate due to the convolution of the Maxwell–Boltzmann energy distribution of the particles and the cross section of a reaction. However, such extrapolations may result in significant uncertainty. Recently at the underground laboratory in Gran Sasso, Italy, a collaboration using a low-energy accelerator has succeeded in measuring the cross section for some reactions involving stable beams and targets to significantly lower energies than has previously been achieved (Broggini 2010). But still extrapolation to astrophysical energies is usually required. Another problem plagues measurements of charged particle reaction rates at low energy. Electron screening distorts the cross section measured in the laboratory compared to the actual rate that applies in stellar plasma. Similarly neutron-induced reactions on unstable short-lived nuclei cannot be measured directly in the laboratory today.

Indirect techniques have been developed over the past several decades to provide ways to determine reaction rates that cannot be measured in the lab. The important information that is needed to determine the reaction rate for reactions that are dominated by a nuclear resonance is the energy of the resonance and its decay width in the appropriate initial and final channels. This information can often be determined by nuclear spectroscopy measurements and either particle or gamma decay measurements from the resonance state. Applications of this approach have been undertaken with both stable and radioactive beams. A review of this approach for determining stellar reaction rates can be found in Smith and Rhem (2001).

In this review we address three different commonly used indirect techniques to obtain the information about astrophysical reactions, the asymptotic normalization coefficient (ANC) method, the Trojan Horse method (THM), and the Coulomb dissociation (CD) method. The ANC method focuses on determining the normalization of the tail of the overlap function. The ANC for a nuclear level determines the direct capture reaction rate associated with that level. For some reactions, this dominates over resonant capture. In other reactions, direct capture often interferes with resonant capture, which can be very important in determining the overall rate at stellar energies. Including both direct and resonant capture in a consistent framework can be done through an R-matrix analysis (Mukhamedzhanov *et al* 2011) if the relevant information is available. The THM provides a way to determine the reaction rate for rearrangement reactions by obtaining the cross section for a binary process through the use of a surrogate 'Trojan Horse' particle. The CD technique uses the virtual photon flux from the interaction of a high-energy ion with a very heavy target to dissociate the heavy ion. The dissociation is an inverse process to a capture-gamma reaction that takes place in a stellar environment. Measurements of the dissociation cross section can be used to infer the reaction rate of radiative capture processes at stellar energies. All three of these methods provide information on stellar reaction rates at very low energy without requiring an extrapolation of data from higher energies.

These three indirect techniques have in common an underlying connection to nuclear reaction theory. Thus the review will begin with a theoretical overview for the three processes, which will be followed by examples of the use of each of the techniques in probing reaction rates in stellar environments.

2. Theoretical considerations

2.1. The ANC technique

Direct capture reactions of astrophysical interest often involve systems where the binding energy of the captured particles is low, so the capture occurs through the tail of the nuclear overlap function in the corresponding two-body channel. The shape of this tail is dictated by the Coulomb interaction. Hence, the capture rate may be calculated accurately if one knows the amplitude of the tail, which is given by the ANC. The role of the ANC in nuclear astrophysics was first discussed in Mukhamedzhanov and Timofeyuk (1990), and Xu *et al* (1994), where it was underscored that the ANC determines the overall normalization of peripheral radiative capture reactions. These papers paved the way for using the ANC method as an indirect technique in nuclear astrophysics (see also Mukhamedzhanov *et al* (2001)).

The ANC can be determined from peripheral transfer reactions at energies above the Coulomb barrier or at sub-Coulomb energies and can be used to calculate peripheral radiative capture reactions. It constitutes a powerful indirect method in nuclear astrophysics. Cross sections of the reactions above the Coulomb barrier are many orders of magnitude larger than direct capture reaction cross sections at astrophysical energies. The sub-Coulomb barrier cross sections are lower than those above the barrier but are still significantly larger than the cross sections at astrophysical energies. The ANC method has been extensively used in the analysis of many important astrophysical reactions (see, for example, Mukhamedzhanov *et al* (1997, 2003a, 2003b, 2006, 2008b, 2011), Gagliardi *et al* (1999), Azhari *et al* (2001), Tang *et al* (2004), Banu *et al* (2009) and Al-Abdullah *et al* (2010) and references therein). If a radiative capture reaction is peripheral and the astrophysical factor is accurately measured the ANC can be determined from the experimental data (Igamov and Yarmukhamedov 2007). The role of the ANC in nuclear astrophysics has been underscored in a recent review of solar reaction rates (Adelberger *et al* 2011).

Many important astrophysical reactions proceed through a sub-threshold resonance, which is a bound state in the entry channel, but can decay emitting a photon or a nuclear fragment. The partial width of the sub-threshold resonance is proportional to the ANC (Mukhamedzhanov and Tribble 1999). In some cases knowledge of the ANC allows one to determine the interference sign of the resonant and non-resonant radiative capture amplitudes. In other uses, the ANC method combined with the THM opens up new possibilities to exploit astrophysical processes (La Cognata *et al* 2012). The ANCs can be used to determine the spectroscopic factors (SFs) (Mukhamedzhanov and Nunes 2005, Pang *et al* 2007). The ANC and the SFs also can be used to determine cross sections for direct (n,γ) capture processes (Mukhamedzhanov *et al* 2008a).

2.1.1. ANCs. ANCs have been studied in few-nucleon systems and 1p-shell nuclei for many years. But the relation between peripheral transfer reaction cross sections and ANCs and the importance of this relation as an indirect technique to measure astrophysical radiative capture rates has only recently been stressed. Usually the distorted-wave Born approximation (DWBA) is used to analyze peripheral transfer reactions. However, in the conventional DWBA, the transfer reaction amplitude is parametrized in terms of SFs rather than ANCs. We articulate here the difference between and the relationship that connects ANCs and SFs. We also address an important consistency issue—the parametrization of a DWBA cross section in terms of SFs is appropriate for non-peripheral transfer reactions, but in such cases, several of the assumptions underlying traditional DWBA treatments are questionable.

The ANC is a fundamental nuclear characteristic important both in nuclear reactions and nuclear structure. The ANC enters the theory in two ways. In the Schrödinger formalism of the wave functions and interaction potentials, the ANC is the amplitude of the overlap function of the bound-state wave functions of the initial and final nuclei. In the scattering theory the residue of the $S-$matrix for the elastic scattering, $x + A$ (throughout the text these symbols represent arbitrary nuclei), is expressed in terms of the ANC. The first comprehensive review about the overlap functions was given in Blokhintsev *et al* (1977) (see also Locher and Mizutani (1978) and Blokhintsev *et al* (1984)). Here we will briefly recall the necessary equations for the overlap functions, ANC and spectroscopic functions, which are important for application of the ANC method as an indirect technique in nuclear astrophysics.

In scattering theory the residue at the poles of the elastic scattering S matrix corresponding to bound states (Kramers 1938, Perelomov *et al* 1966) or resonances (Dolinsky and Mukhamedzhanov 1977) can be expressed in terms of the ANC:

$$S^{J_F}_{l_F j_F; l_F j_F} \xrightarrow{k \to k^p_{xA}} \frac{A_{l_F j_F}}{k_{xA} - k^p_{xA}} \tag{2.1}$$

with the residue

$$A^{J_F}_{l_F j_F} = -\mathrm{i}^{2l_F+1} \mathrm{e}^{\mathrm{i}\pi\eta^p_{xA}} (C^F_{xAl_F j_F J_F})^2, \tag{2.2}$$

where $C^F_{xAl_F j_F J_F}$ is the ANC for the virtual or real decay $F \to x + A$ in the channel with the relative orbital angular momentum l_F of x and A, the total angular momentum j_F of x and total angular momentum J_F of the system $x + A$, $\boldsymbol{k}_{xA}$ is the relative momentum of particles x and A. If $F = (xA)$ is a bound state,

$$\eta^p_{xA} \equiv \eta^{\mathrm{bs}}_{xA} = \frac{Z_x Z_A e^2 \mu_{xA}}{\kappa^F_{xA}} \tag{2.3}$$

is the Coulomb parameter for the bound state $F = (xA)$, $k^p_{xA} = \mathrm{i}\kappa^F_{xA}$, $\kappa^F_{xA} = \sqrt{2\mu_{xA}\varepsilon^F_{xA}}$ is the bound-state wave number, $\varepsilon^F_{xA} = m_x + m_A - m_F$ is the binding energy for the virtual decay $F \to x + A$, $Z_i e$ and m_i is the charge and mass of particle i, and μ_{xA} is the reduced mass of x and A. Throughout the paper we use the system of units with $\hbar = c = 1$. Note that singling out the factor $\mathrm{e}^{\mathrm{i}\pi\eta^p_{xA}}$ in the residue makes the ANC for bound states real.

If F is a resonance, that is the decay $F \to x + A$ is real, then

$$\eta^p_{xA} = i\eta^R_{xA}, \qquad \eta^R_{xA} = \frac{Z_x Z_A e^2 \mu_{xA}}{k_{xA(R)}} \tag{2.4}$$

is the Coulomb parameter for the resonance state with complex relative momentum $k^p_{xA} = k_{xA(R)}$, $k_{xA(R)} = \sqrt{2\mu_{xA} E_{xA(R)}}$, $E_{xA(R)}$ is the resonance energy in the system $x + A$ of the resonance state $F = (xA)$. Equations (2.1) and (2.2) are valid for both bound-state poles and resonances (Dolinsky and Mukhamedzhanov 1977) and provide the most general and model-independent definition of the ANC.

In the case of the Breit–Wigner resonance ($\mathrm{Im} k_{xA(R)} \ll \mathrm{Re}\, k_{xA(R)} = k^0_{xA(R)}$) the residue of the elastic scattering S-matrix element in terms of the resonance width is (Dolinsky and Mukhamedzhanov 1977)

$$A^{J_F}_{l_F j_F} = -\mathrm{i}\mathrm{e}^{2\mathrm{i}\delta^p_{l_F j_F J_F}(k^0_{xA})} \frac{\mu_{xA}}{k^0_{xA(R)}} \Gamma_{xAl_F j_F J_F}, \tag{2.5}$$

where $\delta^p_{l_F j_F J_F}(k^0_{xA})$ is the potential (non-resonance) scattering phase shift at the real resonance relative momentum $k^0_{xA(R)}$.

Equation (2.2) in the Breit–Wigner resonance case takes the form

$$A_{l_F j_F}^{J_F} = -\mathrm{i}^{2l_F+1}\mathrm{e}^{-\pi\eta_{xA}^{(0)}}(C_{xAl_F j_F J_F}^{F})^2, \tag{2.6}$$

where $\eta_{xA}^{(0)} = Z_x Z_A e^2 \mu_{xA}/k_{xA(R)}^0$. Then the ANC and the partial width of the resonance are related by

$$(C_{xAl_F j_F J_F}^{F})^2 = (-1)^{-l_F}\mathrm{e}^{\pi\eta_{xA}^{(0)}}\mathrm{e}^{\mathrm{i}2\delta_{l_F j_F J_F}^{p}(k_{xA(R)}^0)}\frac{\mu_{xA}\Gamma_{xAl_F j_F J_F}}{k_{xA(R)}^0}. \tag{2.7}$$

For a sub-threshold resonance (a nuclear level that is a bound state in the entry channel and a resonance in the exit channel), the connection between the ANC and the partial width, calculated at the relative momentum of particles x and A, k_{xA}, is given by Mukhamedzhanov and Tribble (1999) as

$$\Gamma_{xAl_F j_F J_F}(k_{xA}) = P_{l_F}(k_{xA}R_{xA})\frac{W_{-\eta_{xA}^{\mathrm{bs}},l_F+1/2}^2(2\kappa_{xA}^F R_{xA})}{\mu_{xA}R_{xA}}$$
$$\times(C_{xAl_F j_F J_F}^{F})^2, \tag{2.8}$$

where $P_{l_F}(k_{xA}R_{xA})$ is the barrier penetrability, $W_{-\eta_{xA}^{bs},l_F+1/2}\times(2\kappa_{xA}^F R_{xA})$ is the Whittaker function for the bound state $F = (xA)$ and R_{xA} is the channel radius. Correspondingly, the reduced width is determined by

$$\gamma_{xAl_F j_F J_F}^2 = \frac{W_{-\eta_{xA}^{\mathrm{bs}},l_F+1/2}^2(2\kappa_{xA}^F R_{xA})}{2\mu_{xA}R_{xA}}(C_{xAl_F j_F J_F}^{F})^2. \tag{2.9}$$

Note that in the R-matrix method the peripheral part of the radiative capture amplitude is expressed in terms of the reduced width rather than the ANC (Barker and Kajino 1991). However, the reduced width is model dependent, because it depends on the channel radius, R_{xA}, while the ANC is not.

Note that the definition of the ANC as the residue in the pole, equation (2.1), is based only on the analytic and unitary character of the $S-$matrix and is valid both in the non-relativistic quantum mechanics and field theory. However, there is another, more familiar but less universal definition of the ANC, which is based on the Schrödinger formalism of the wave functions and potentials. In this formalism the ANC is defined as the amplitude of the tail of the overlap function of the bound-state wave functions of F, A and a. The overlap function is given by (in the isospin formalism)

$$I_{xA}^F(\boldsymbol{r}_{xA}) = \langle\psi_c|\varphi_F(\xi_A,\xi_x;\boldsymbol{r}_{xA})\rangle$$
$$= \binom{A}{x}^{\frac{1}{2}}\langle\varphi_A(\xi_A)\varphi_x(\xi_x)|\varphi_F(\xi_A,\xi_x;\boldsymbol{r}_{xA})\rangle$$
$$= \sum_{l_F m_{lF} j_F m_{j_F}}\langle J_A M_A j_F m_{j_F}|J_F M_F\rangle\langle J_x M_x l_F m_{l_F}|j_F m_{j_F}\rangle$$
$$\times Y_{l_F m_{l_F}}(\hat{\boldsymbol{r}}_{xA})I_{xAl_F j_F J_F}^F(r_{xA}). \tag{2.10}$$

Here

$$\psi_c = \sum_{m_{j_F} m_{l_F} M_A M_x}\langle J_A M_A j_F m_{j_F}|J_F M_F\rangle\langle J_x M_x l_F m_{lF}|j_F m_{j_F}\rangle$$
$$\times\hat{A}_{xA}\{\varphi_A(\xi_A)\varphi_x(\xi_x)Y_{l_F m_{l_F}}(\hat{\boldsymbol{r}}_{xA})\} \tag{2.11}$$

is the two-body $x + A$ channel wave function in the jj coupling scheme, $\langle j_1 m_1 j_2 m_2|jm\rangle$ is the Clebsch–Gordan coefficient, $\hat{A}_{xA}$ is the antisymmetrization operator between the nucleons of nuclei x and A; $\varphi_i(\xi_i)$ represents the fully antisymmetrized bound-state wave function of nucleus i with ξ_i being a set of the internal coordinates including spin–isospin variables, J_i and M_i are the spin and spin projection of nucleus i. Also $\boldsymbol{r}_{xA}$ is the radius-vector connecting the centers of mass of nuclei x and A where $\hat{\boldsymbol{r}}_{xA} = \boldsymbol{r}_{xA}/r_{xA}$, $Y_{l_F m_{l_F}}(\hat{\boldsymbol{r}}_{xA})$ is the spherical harmonics, and $I_{xAl_F j_F J_F}^F(r_{xA})$ is the radial overlap function. The summation over l_F and j_F is carried out over the values allowed by the angular momentum and parity conservation in the virtual process $F \to A + x$. The radial overlap function is given by

$$I_{xAl_F j_F J_F}^F(r_{xA})$$
$$= \langle\hat{A}_{xA}\{\varphi_A(\xi_A)\varphi_x(\xi_x)Y_{l_F m_{l_F}}(\hat{\boldsymbol{r}}_{xA})\}|\varphi_F(\xi_A,\xi_x;\boldsymbol{r}_{xA})\rangle$$
$$= \binom{A}{x}^{1/2}\langle\varphi_A(\xi_A)\varphi_x(\xi_x)Y_{l_F m_{l_F}}(\hat{\boldsymbol{r}}_{xA})|\varphi_F(\xi_A,\xi_x;\boldsymbol{r}_{xA})\rangle. \tag{2.12}$$

Equation (2.12) follows from a trivial observation that, because φ_F is fully antisymmetrized, the antisymmetrization operator $\hat{A}_{xA}$ can be replaced by the factor $\binom{A}{x}^{1/2}$. Here, in contrast to Blokhintsev *et al* (1977), we absorb this factor into the radial overlap function.

The tail of the radial overlap function ($r_{xA} > R_{xA}$) in the case of the normal asymptotic behavior is given by

$$I_{xAl_F j_F J_F}^F(r_{xA}) \xrightarrow{r_{xA}>R_{xA}} C_{xAl_F j_F J_F}^F\frac{W_{-\eta_{xA}^{\mathrm{bs}},l_F+1/2}(2\kappa_{xA}^F r_{xA})}{r_{xA}}$$
$$\xrightarrow{r_{xA}\to\infty} C_{xAl_F j_F J_F}^F\frac{\mathrm{e}^{-\kappa_{xA}^F r_{xA}-\eta_{xA}^{bs}\ln(2\kappa_{xA}^F r_{xA})}}{r_{xA}}. \tag{2.13}$$

Correspondingly, for the resonance case

$$I_{xAl_F j_F J_F}^F(r_{xA}) \xrightarrow{r_{xA}>R_{xA}} C_{xAl_F j_F J_F}^F\frac{W_{-\mathrm{i}\eta_{xA}^R,l_F+1/2}(-2\mathrm{i}k_{xA(R)}r_{xA})}{r_{xA}}$$
$$\xrightarrow{r_{xA}\to\infty} C_{xAl_F j_F J_F}^F\frac{\mathrm{e}^{-\mathrm{i}k_{xA(R)}r_{xA}-\mathrm{i}\eta_{xA}^R\ln(-2\mathrm{i}k_{xA(R)}r_{xA})}}{r_{xA}}. \tag{2.14}$$

The proof of the fundamental connection between the residue $A_{l_F j_F}^{J_F}$ in the bound-state pole of the elastic scattering S matrix and the amplitude $C_{xAl_F j_F J_F}^F$ of the tail of the overlap function was presented first by Kramers (1938) and later by Heisenberg (1946), Möller (1946) and Hu (1948). Note that in these works the ANC was the amplitude of the bound-state wave function of two structureless particles. The proof of this relationship for charged particles was given by Perelomov *et al* (1966). Finally, the extension of this relationship to bound states and resonances for charged particles was presented by Dolinsky and Mukhamedzhanov (1977).

2.1.2. Coulomb renormalization of the ANC.

The study of ANCs of astrophysical interest often requires the use of weak radioactive beams, which generally involves more difficult and less accurate experiments than ones with stable beams. The higher intensities of stable beams means that they can be used at energies below the Coulomb barrier where the sensitivity to optical potentials, which are the main source of uncertainty for ANCs determined from transfer reactions, is minimized. The

ANCs for the neutron removal from a nucleus whose mirror is of astrophysical interest for proton removal can be determined from transfer experiments with stable beams. These neutron ANCs can be related in a model independent way by charge symmetry of nuclear forces to the proton ANCs. Here we address the Coulomb renormalization of the ANCs allowing one to connect the proton and neutron ANCs for mirror nuclei.

The repulsive Coulomb interaction between the charged particles creates the barrier, which results in the appearance of the factor $r_{xA}^{-\eta_{xA}^{bs}}$ in the asymptotic behavior of the radial overlap function, see (2.13), leading to its faster decrease. The decrease of the asymptotic part of the overlap function leads to an increase of the ANC. It was shown by Blokhintsev *et al* (1984) that the main Coulomb renormalization factor (CRF) of the ANC is given by

$$\mathcal{R}_1 = \left[\frac{\Gamma(l_F + 1 + \eta_{xA}^{\rm bs})}{l_F!}\right]^2 . \tag{2.15}$$

We can introduce the Coulomb renormalized ANC $\tilde{C}^F_{xAl_Fj_FJ_F}$ for the virtual decay $F \to A + x$, in which the main CRF is eliminated. It is related to the conventional ANC as

$$C^F_{xAl_Fj_FJ_F} = \frac{\Gamma(l_F + 1 + \eta_{xA}^{\rm bs})}{l_F!}\tilde{C}^F_{xAl_Fj_FJ_F} . \tag{2.16}$$

Let us introduce also the Coulomb renormalized Whittaker function:

$$\begin{aligned}&\widetilde{W}_{-\eta_{xA}^{\rm bs}, l_F+1/2}(2\kappa^F_{xA} r_{xA})\\ &\quad = \frac{l_F!}{\Gamma(l_F + \eta_{xA}^{\rm bs} + 1)} W_{-\eta_{xA}^{\rm bs}, l_F+1/2}(2\kappa^F_{xA} r_{xA}) .\end{aligned} \tag{2.17}$$

Then the tail of the overlap function can be rewritten in terms of the renormalized ANC and Whittaker function as

$$\begin{aligned}I^F_{xA\,l_Fj_FJ_F}(r_{xA}) &\xrightarrow{r>R_{xA}} C^F_{xAl_Fj_FJ_F}\frac{W_{-\eta_{xA}^{\rm bs}, l_F+1/2}(2\kappa^F_{xA} r_{xA})}{r_{xA}}\\ &= \tilde{C}^F_{xAl_Fj_FJ_F}\frac{\widetilde{W}_{-\eta_{xA}^{\rm bs}, l_F+1/2}(2\kappa^F_{xA} r_{xA})}{r_{xA}} .\end{aligned} \tag{2.18}$$

Timofeyuk *et al* (2003) derived an approximate ratio of the proton and neutron squares of the ANCs for mirror states

$$R_0 = \frac{(C^F_{pAl_Fj_FJ_F})^2}{(C^F_{nAl_Fj_FJ_F})^2} = \left|\frac{\mathrm{e}^{\mathrm{i}\sigma_{l_F}} F_{l_F}(\mathrm{i}\kappa^F_{pA}, R_{NA})}{\kappa^F_{pA} R_{NA}\, j_{l_F}(\mathrm{i}\kappa^{A+1}_{nA} R_{NA})}\right|^2 . \tag{2.19}$$

Here,

$$\begin{aligned}\mathrm{e}^{\mathrm{i}\sigma_{l_F}} F_{l_F}(\mathrm{i}\kappa^F_{pA}, r_{pA}) &= \mathrm{e}^{\mathrm{i}\pi\eta_{pA}^{bs}/2}\frac{\Gamma(l_F + 1 + \eta_{pA}^{\rm bs})}{2\Gamma(2l_F + 2)}(2\mathrm{i}\kappa^F_{pA} r_{pA})^{l_F+1}\\ &\quad\times \mathrm{e}_1^{-\kappa^F_{pA} r_{pA}} F_1(l_F + 1 + \eta_{pA}^{\rm bs}, 2l_F + 2; 2\kappa^F_{pA} r_{pA})\end{aligned} \tag{2.20}$$

is the regular partial Coulomb wave function at the imaginary momentum $k_{pA} = \mathrm{i}\kappa^F_{pA}$, $j_{l_F}(\mathrm{i}\kappa^{A+1}_{nA} R_{NA})$ is the spherical Bessel function at imaginary momentum $\mathrm{i}\kappa^{A+1}_{nA}$, σ_{l_F} is the Coulomb scattering phase shift. As we can see the CRF $\mathcal{R}_1^{1/2}$ appears explicitly in (2.20) confirming the results from Blokhintsev *et al* (1984).

For loosely bound states $C^F_{xAl_Fj_FJ_F}$ can be a huge number. For example, the proton binding energy of the bound state $^{21}\mathrm{Na}(\frac{1}{2}^+, E_x = 2.425\ \mathrm{MeV})$ is $\varepsilon^{^{21}\mathrm{Na}}_{p^{20}\mathrm{Ne}} = 7.1 \pm 0.6\,\mathrm{keV}$ with the bound-state Coulomb parameter, $\eta^{\rm bs}_{p^{20}\mathrm{Ne}} = 18.3$. The proton removal ANC for this state extracted from the analysis of the peripheral $^{20}\mathrm{Ne}(^3\mathrm{He}, \mathrm{d})^{21}\mathrm{Na}(2\mathrm{s}^+_{1/2})$ reaction (Mukhamedzhanov *et al* 2006) is $C^{^{21}\mathrm{Na}}_{p^{20}\mathrm{Ne}0\ 1/2\ 1/2} = 8.3 \times 10^{16}\,\mathrm{fm}^{-1/2}$. The square root of CRF for $l_F = 0$ is $\mathcal{R}_1^{1/2} = \Gamma(\eta^{\rm bs}_{p^{20}\mathrm{Ne}} + 1) = 1.56 \times 10^{16}$ resulting in the Coulomb renormalized ANC $\tilde{C}^{^{21}\mathrm{Na}}_{p^{20}\mathrm{Ne}0\ 1/2\ 1/2} = 5.32\,\mathrm{fm}^{-1/2}$, which is significantly smaller than the conventional one and close to the one generated by a pure nuclear interaction.

We also can rewrite the width of the sub-threshold resonance

$$\begin{aligned}\Gamma_{xA\,l_Fj_FJ_F} &= 2P_{l_F}(R_{xA})\gamma^2_{l_Fj_FJ_F}\\ &= P_{l_F}(R_{xA})\frac{\widetilde{W}^2_{-\eta_{xA}^{\rm bs}, l_F+1/2}(2\kappa^F_{xA} R_{xA})}{\mu_{xA} R_{xA}}(\tilde{C}^F_{xA\,l_Fj_FJ_F})^2,\end{aligned} \tag{2.21}$$

with

$$\gamma^2_{xAl_Fj_FJ_F} = \frac{\widetilde{W}^2_{-\eta_{xA}^{\rm bs}, l_F+1/2}(2\kappa^F_{xA} R_{xA})(\widetilde{C}^F_{xAl_Fj_FJ_F})^2}{2\mu_{xA} R_{xA}} . \tag{2.22}$$

An expression for the ANC also can be obtained starting from the Pinkston–Satchler equation (Pinkston and Satchler 1965), which contains the source term (Mukhamedzhanov and Timofeyuk 1990, Timofeyuk 1998). From this equation the expression for the ANC in terms of the Wronskian can be derived (Mukhamedzhanov 2012):

$$\begin{aligned}C^F_{xAl_Fj_FJ_F} &= \mathrm{e}^{-\mathrm{i}\pi\eta_{xA}^{\rm bs}/2}\frac{1}{L^{C(+)}_{l_F}(\mathrm{i}\kappa^F_{xA})}\\ &\quad\times W[I^F_{xAl_Fj_FJ_F}(r_{xA}), \varphi^C_{l_F}(\mathrm{i}\kappa^F_{xA}, r_{xA})]|_{r_{xA}=R_{xA}},\end{aligned} \tag{2.23}$$

where the Wronskian is

$$\begin{aligned}W_x(\mathrm{i}\kappa^F_{xA} r_{xA}) &= W[I^F_{xAl_Fj_FJ_F}(r_{xA}), \varphi^C_{l_F}(\mathrm{i}\kappa^F_{xA}, r_{xA})]\\ &= I^F_{xAl_Fj_FJ_F}(r_{xA})\frac{\mathrm{d}\varphi^C_{l_F}(\mathrm{i}\kappa^F_{xA}, r_{xA})}{\mathrm{d}r_{aA}}\\ &\quad-\varphi^C_{l_F}(\mathrm{i}\kappa^F_{xA}, r_{xA})\frac{\mathrm{d}I^F_{xAl_Fj_FJ_F}(r_{xA})}{\mathrm{d}r_{aA}} .\end{aligned} \tag{2.24}$$

$$\begin{aligned}\varphi^C_{l_F}(\mathrm{i}\kappa^F_{xA}, r_{xA}) &= -\frac{1}{2\kappa^F_{xA}}\Big[L^{C(-)}_{l_F}(\mathrm{i}\kappa^F_{xA}) f^{C(+)}_{l_F}(\mathrm{i}\kappa^F_{xA}, r_{xA})\\ &\quad- L^{C(+)}_{l_F}(\mathrm{i}\kappa^F_{xA}) f^{C(-)}_{l_F}(\mathrm{i}\kappa^F_{xA}, r_{xA})\Big]\\ &= r_{xA}^{l_F+1}\mathrm{e}_1^{-\kappa^F_{xA} r_{xA}} F_1(l_F + 1 + \eta^{\rm bs}_{xA}, 2l_F + 2; 2\kappa^F_{xA} r_{xA})\\ &= \mathrm{e}^{-\mathrm{i}\pi l_F/2} L^{C(+)}_{l_F}(\mathrm{i}\kappa^F_{xA})\frac{\mathrm{e}^{\mathrm{i}\sigma_{l_F}} F_{l_F}(\mathrm{i}\kappa^F_{xA}, r_{xA})}{\mathrm{i}\kappa^F_{xA}}\end{aligned} \tag{2.25}$$

is the Coulomb regular solution of the partial Schrödinger equation at imaginary momentum $\mathrm{i}\kappa^F_{xA}$,

$$f^{C(\pm)}_{l_F}(\mathrm{i}\kappa^F_{xA}, r_{xA}) = \mathrm{e}^{-\mathrm{i}\pi\eta_{xA}^{bs}/2} W_{\mp\eta^{\rm bs}_{xA}, l_F+1/2}(\pm 2\kappa^F_{xA} r_{xA}) \tag{2.26}$$

are the Jost solutions (singular at the origin $r_{xA} = 0$) and

$$L^{C(\pm)}_{l_F}(\mathrm{i}\kappa^F_{xA}) = \frac{1}{(2\mathrm{i}\kappa^F_{xA})^{l_F}}\mathrm{e}^{-\mathrm{i}\pi\eta^{\rm bs}_{xA}/2}\mathrm{e}^{\pm\mathrm{i}\pi l_F/2}\frac{\Gamma(2l_F + 2)}{\Gamma(l_F + 1 \pm \eta^{\rm bs}_{xA})} \tag{2.27}$$

are the Jost functions.

It is straightforward to see that this ANC is a real quantity because $\varphi^{C}_{l_F}(\mathrm{i}\kappa^{F}_{xA}, r_{xA})$ given by (2.25), $I^{F}_{xAl_F j_F J_F}(r_{xA})$, and $\mathrm{e}^{-\mathrm{i}\pi\eta^{bs}_{xA}/2}\frac{1}{L^{C(+)}_{l_F}(\mathrm{i}\kappa^{F}_{xA})}$ are real at the pure imaginary momentum $k_{xA} = \mathrm{i}\kappa^{F}_{xA}$.

Correspondingly, the Coulomb renormalized ANC is given by

$$\widetilde{C}^{F}_{xAl_F j_F J_F} = (2\kappa^{F}_{xA})^{l_F}\frac{\Gamma(l_F+1)}{\Gamma(2l_F+2)} \times W[I^{F}_{xAl_F j_F J_F}(r_{xA}), \varphi^{C}_{l_F}(\mathrm{i}\kappa^{F}_{xA}, r_{xA})]|_{r_{xA}=R_{xA}}. \qquad (2.28)$$

The Wronskian calculated for two independent solutions of the Schrödinger equation is constant. Because the radial overlap function $I^{F}_{xAl_F j_F J_F}(r_{xA})$ is not a solution of the Schrödinger equation in the nuclear interior, the Wronskian and, hence, the ANCs determined by (2.23) and (2.28) depend on the channel radius R_{aA}, if it is not too large. However, if the adopted channel radius is large enough, we can replace the radial overlap function by its asymptotic term, see (2.13), proportional to the Whittaker function, which determines the radial shape of the asymptotic radial overlap function and is a singular solution of the radial Schrödinger equation. $\varphi^{C}_{l_F}(\mathrm{i}\kappa^{F}_{xA}, r_{xA})$ is the independent regular solution of the same equation at large R_{xA} where the nuclear $x - A$ interaction can be neglected and the asymptotic form of (2.13) can be applied. Taking into account that $W[f^{C(+)}_{l_F}(\mathrm{i}\kappa^{F}_{xA}, r_{xA}), f^{C(-)}_{l_F}(\mathrm{i}\kappa^{F}_{xA}, r_{xA})] = 2\kappa^{F}_{xA}$, we get at large R_{xA}

$$\mathrm{e}^{-\mathrm{i}\pi\eta^{\mathrm{bs}}_{xA}/2}\frac{1}{L^{C(+)}_{l_F}(\mathrm{i}\kappa^{F}_{xA})} W[I^{F}_{xAl_F j_F J_F}(r_{xA}), \varphi^{C}_{l_F}(\mathrm{i}\kappa^{F}_{xA}, r_{xA})]|_{r_{xA}=R_{xA}} = C^{F}_{xAl_F j_F J_F}. \qquad (2.29)$$

Hence (2.23) at large R_{xA}, as expected, is verified. The main advantage of this equation is that it can be used at R_{xA}, which does not exceed the radius of nucleus $F = (xA)$. In the nuclear interior the contemporary microscopic models provide quite accurate overlap functions. Note that the ANCs calculated using (2.23) and (2.28) may depend on the adopted channel radius R_{xA} but the ratio of the mirror ANCs, as shown below, is practically insensitive to R_{xA}. This allows us to analyze the impact of the Coulomb effects on the ANC by separating the different scales of these effects.

From (2.23) we get the ratio of the squares of the proton and neutron ANCs for mirror nuclei:

$$L^{W}_{pn}(R_{NA}) = \frac{(C^{F}_{pAl_F j_F J_F})^2}{(C^{A+1}_{nAl_F j_F J_F})^2} = \left[\left(\frac{\kappa^{F}_{pA}}{\kappa^{A+1}_{nA}}\right)^{l_F}\frac{\Gamma(l_F+1+\eta^{\mathrm{bs}}_{pA})}{\Gamma(l_F+1)}\frac{W_p(\mathrm{i}\kappa^{F}_{pA}R_{NA})}{W_n(\mathrm{i}\kappa^{A+1}_{nA}R_{NA})}\right]^2. \qquad (2.30)$$

Here $W_p(\mathrm{i}\kappa^{F}_{pA}R_{NA})(W_n(\mathrm{i}\kappa^{A+1}_{nA}R_{NA}))$ is the Wronskian calculated for the proton (neutron) at the channel radius R_{NA}. To get the proton (neutron) Wronskian we can just replace $x \to p$ ($x \to n$) in (2.24).

For the neutron Wronskian

$$\varphi_{l_F}(\mathrm{i}\kappa^{A+1}_{nA}, r_{nA}) = r^{l_F+1}_{nA}\mathrm{e}^{-\kappa^{A+1}_{nA}r_{nA}}\,{}_1F_1(l_F+1, 2l_F+2;\ 2\kappa^{A+1}_{nA}r_{nA}), \qquad (2.31)$$

$\kappa^{A+1}_{nA} = \sqrt{2\mu_{nA}\varepsilon^{A+1}_{nA}}$ is the wave number of the bound state $A+1 = (nA)$ of the isobaric analog state of the bound state $F = (pA)$.

The calculation of the ratio of the mirror nucleon ANCs requires knowledge of the microscopic radial overlap functions. Equation (2.19) obtained in Timofeyuk *et al* (2003) can be used when the overlap functions are not available. We show here how to obtain (2.19) starting from (2.30) (Mukhamedzhanov 2012). First, as it was pointed out in Timofeyuk *et al* (2003), in the nuclear interior the Coulomb interaction varies very little in the vicinity of R_{NA} and its effect leads only to shifting of the nucleon binding energy. Hence, we assume that $\varphi^{C}_{l_F}(\mathrm{i}\kappa^{F}_{xA}, r_{xA})$ and $\varphi_{l_F}(\mathrm{i}\kappa^{F}_{xA}r_{xA})$ behave similarly at $r_{NA} \approx R_{NA}$ except for the overall normalization, that is

$$\varphi^{C}_{l_F}(\mathrm{i}\kappa^{F}_{pA}r_{pA}) = \frac{\varphi^{C}_{l_F}(\mathrm{i}\kappa^{F}_{pA}R_{NA})}{\varphi_{l_F}(\mathrm{i}\kappa^{A+1}_{nA}R_{NA})}\varphi_{l_F}(\mathrm{i}\kappa^{A+1}_{nA}r_{pA}). \qquad (2.32)$$

Then (2.30) reduces

$$L^{W'}_{pn}(R_{NA}) = \frac{(C^{F}_{pAl_F j_F J_F})^2}{(C^{A+1}_{nAl_F j_F J_F})^2} \approx \left[\left(\frac{\kappa^{F}_{pA}}{\kappa^{A+1}_{nA}}\right)^{l_F}\frac{\Gamma(l_F+1+\eta^{\mathrm{bs}}_{pA})}{\Gamma(l_F+1)}\frac{\varphi^{C}_{l_F}(\mathrm{i}\kappa^{F}_{pA}, R_{NA})}{\varphi_{l_F}(\mathrm{i}\kappa^{A+1}_{nA}, R_{NA})} \times \frac{W[I^{F}_{pAj_F J_F}(r_{pA}), \varphi_{l_F}(\mathrm{i}\kappa^{A+1}_{nA}, r_{pA})]|_{r_{pA}=R_{NA}}}{W[I^{A+1}_{nAl_F j_F J_F}(r_{nA}), \varphi_{l_F}(\mathrm{i}\kappa^{A+1}_{nA}, r_{nA})]|_{r_{nA}=R_{NA}}}\right]^2. \qquad (2.33)$$

Neglecting the difference between the proton and neutron mirror overlap functions in the nuclear interior, we obtain the approximate ratio of the squares of the mirror ANCs from Timofeyuk *et al* (2003)

$$L_{pn}(R_{NA}) = \frac{(C^{F}_{pAl_F j_F J_F})^2}{(C^{A+1}_{nAl_F j_F J_F})^2} \approx \left[\left(\frac{\kappa^{F}_{pA}}{\kappa^{A+1}_{nA}}\right)^{l_F}\frac{\Gamma(l_F+1+\eta^{\mathrm{bs}}_{pA})}{\Gamma(l_F+1)}\frac{\varphi^{C}_{l_F}(\mathrm{i}\kappa^{F}_{pA}, R_{NA})}{\varphi_{l_F}(\mathrm{i}\kappa^{A+1}_{nA}, R_{NA})}\right]^2. \qquad (2.34)$$

It is important to understand the physics causing the difference between the proton and neutron mirror ANCs. First of all, the proton ANC is affected by the main CRF, $\mathcal{R}_1$ (see (2.15)). Eliminating this major factor from the proton ANC we obtain the ratio of the squares of the Coulomb renormalized proton and neutron ANCs:

$$\tilde{L}^{W}_{pn}(R_{NA}) = \frac{(\widetilde{C}^{F}_{pAl_F j_F J_F})^2}{(C^{A+1}_{nAl_F j_F J_F})^2} = \left[\left(\frac{\kappa^{F}_{pA}}{\kappa^{A+1}_{nA}}\right)^{l_F}\frac{W_p(\mathrm{i}\kappa^{F}_{pA}, R_{NA})}{W_n(\mathrm{i}\kappa^{A+1}_{nA}, R_{NA})}\right]^2. \qquad (2.35)$$

This ratio still may be far from unity. After we removed the main CRF, $\mathcal{R}_1$, there are two more remaining CRFs, which determine the difference between the proton and neutron mirror ANCs. The second factor appears because of the difference in the proton and neutron binding energies. The dependence of the ANC on the binding energy is exponential. Because the binding energy of the neutron analog state is larger than the corresponding proton binding energy, the renormalized squared proton ANC $(\widetilde{C}^{F}_{pAl_F j_F J_F})^2$ is lower than $(\widetilde{C}^{A+1}_{nAl_F j_F J_F})^2$, and the second CRF decreases the proton ANC: the bigger the difference $\varepsilon^{A+1}_{nA} - \varepsilon^{F}_{pA}$, the stronger the decrease of the proton ANC. The third CRF, which increases the proton ANC compared to the neutron one, is generated by the fine Coulomb effects (the effects left after removal the main CRF and difference in the binding energies) and is minor compared to the first two CRFs. Now after this discussion we can rewrite (2.35) as

$$\tilde{L}^{W}_{pn}(R_{NA}) = \widetilde{\mathcal{R}}^{W}_{2}\widetilde{\mathcal{R}}^{W}_{3}, \tag{2.36}$$

where

$$\widetilde{\mathcal{R}}^{W}_{2} = \left[\left(\frac{\kappa^{F}_{pA}}{\kappa^{A+1}_{nA}}\right)^{l_F} \frac{W_n(i\kappa^{F}_{pA}R_{NA})}{W_n(i\kappa^{A+1}_{nA}R_{NA})}\right]^2 \tag{2.37}$$

and

$$\widetilde{\mathcal{R}}^{W}_{3} = \left|\frac{W_p(\mathrm{i}\kappa^{F}_{pA}R_{NA})}{W_n(\mathrm{i}\kappa^{F}_{pA}R_{NA})}\right|^2. \tag{2.38}$$

To calculate the binding energy effect $\widetilde{\mathcal{R}}^{W}_{2}$ on the ratio of the ANCs, it is sufficient to replace the proton Wronskian $W_p(\mathrm{i}\kappa^{F}_{pA}R_{NA})$ in (2.35) by the neutron one $W_n(\mathrm{i}\kappa^{F}_{pA}R_{NA})$ that is calculated at the proton binding energy. To calculate the impact of the fine Coulomb effects it is sufficient to consider the ratio of the squared proton and neutron Wronskians both calculated at the proton binding energy. For the ratio of the ANCs $\tilde{L}_{pn}$ considered in Timofeyuk *et al* (2003), we get

$$\tilde{L}_{pn} = \widetilde{\mathcal{R}}_{2}\widetilde{\mathcal{R}}_{3}, \tag{2.39}$$

where

$$\widetilde{\mathcal{R}}_{2} = \left[\left(\frac{\kappa^{F}_{pA}}{\kappa^{A+1}_{nA}}\right)^{l_F} \frac{\varphi_{l_F}(\mathrm{i}\kappa^{F}_{pA}, R_{NA})}{\varphi_{l_F}(\mathrm{i}\kappa^{A+1}_{nA}, R_{NA})}\right]^2 \tag{2.40}$$

is the CRF determining the effect of the binding energy, while

$$\widetilde{\mathcal{R}}_{3} = \left[\frac{\varphi^{C}_{l_F}(\mathrm{i}\kappa^{F}_{pA}, R_{NA})}{\varphi_{l_F}(\mathrm{i}\kappa^{F}_{pA}, R_{NA})}\right]^2 \tag{2.41}$$

is the CRF determining the fine Coulomb effects. Thus we can express the squared proton ANC in terms of the mirror squared neutron one as

$$(C^{F}_{pAl_F j_F J_F})^2 = \mathcal{R}_1\widetilde{\mathcal{R}}^{W}_{2}\widetilde{\mathcal{R}}^{W}_{3}(C^{A+1}_{nAl_F j_F J_F})^2 \tag{2.42}$$

or

$$(C^{F}_{pAl_F j_F J_F})^2 = \mathcal{R}_1\widetilde{\mathcal{R}}_{2}\widetilde{\mathcal{R}}_{3}(C^{A+1}_{nAl_F j_F J_F})^2 \tag{2.43}$$

depending on whether we use the Wronskian approach or the simplified version in (2.34). Here we took into account that the quantum numbers of the proton and neutron analog states are the same.

In figure 1 the comparison of the ratio of the squared proton and neutron ANCs for mirror nuclei ^{41}Sc and ^{41}Ca is shown.

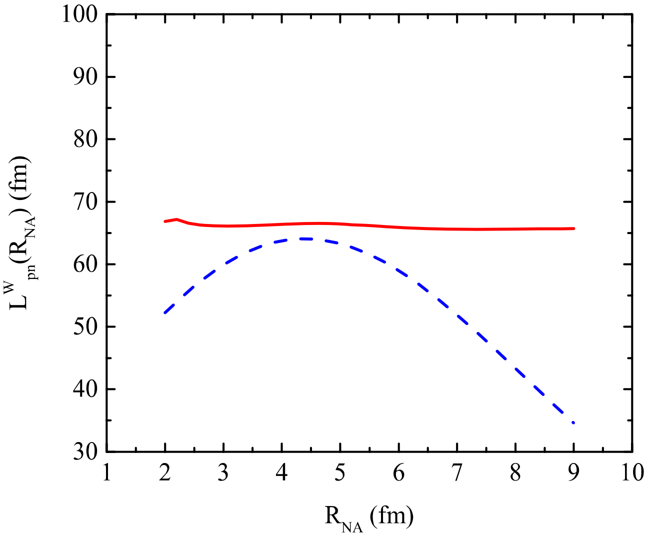

Figure 1. Ratio $L^{W}_{pn}(R_{NA})$ of the square of the proton ANC for the virtual decay between the ground states of $^{41}Sc \to {}^{40}$Ca + p to the square of the neutron ANC for the mirror nucleus virtual decay $^{41}Ca \to {}^{40}$Ca + n as a function of the channel radius. The solid red line is from the Wronskian method from (2.30) with the overlap functions taken from Timofeyuk (2011); the dashed blue line is the approximated result (2.34) as in Timofeyuk *et al* (2003).

In the Wronskian method, the microscopic proton and neutron overlap functions from Timofeyuk (2011) were used. As we can see, the Wronskian method provides the ratio, which is nearly independent of the channel radius R_{NA}. Thus, we can use the microscopically calculated overlap functions with the wrong tail and still get a reliable ratio of the mirror ANCs using the channel radius at which these overlap functions are reasonable.

Now we consider how the Coulomb renormalization affects the proton ANC for the virtual decay $^{41}Sc \to {}^{40}$Ca + p, where $(C^{^{41}\mathrm{Sc}}_{p^{40}\mathrm{Ca}3\,7/2\,7/2})^2 = 286.9\,\mathrm{fm}^{-1}$. There are three CRFs. Dividing the proton squared ANC by each of these factors, we can eliminate step by step all three Coulomb effects eventually arriving at the neutron squared ANC. To estimate the different CRFs, we use (2.43), (2.40) and (2.41). The main CRF in this case is $\mathcal{R}_1 = 14\,311.9$. Using this gives the Coulomb renormalized square of the proton ANC as $(\widetilde{C}^{^{41}\mathrm{Sc}}_{p^{40}\mathrm{Ca}37/27/2})^2 = (C^{^{41}\mathrm{Sc}}_{p^{40}\mathrm{Ca}37/27/2})^2/\mathcal{R}_1 = 0.02\,\mathrm{fm}^{-1}$. Now we take into account the remaining two CRFs coming from the difference in the proton and neutron binding energies and the residual Coulomb effects. Because at $R_{NA} = 4.4$ fm the ratio of the proton and neutron ANCs obtained using (2.44a) is the closest to the one obtained by the Wronskian method, the remaining two Coulomb renormalizations are calculated at $R_{NA} = 4.45$ fm. The binding energy of the proton in ^{41}Sc(0.0MeV) is $\varepsilon^{^{41}\mathrm{Sc}}_{p^{40}\mathrm{Ca}} = 1.085$ MeV, while the neutron binding energy in ^{41}Ca(0.0 MeV) is $\varepsilon^{^{41}\mathrm{Ca}}_{n^{40}\mathrm{Ca}} = 8.362$ MeV. This large difference in the neutron and proton binding energies leads to a significant renormalization of the proton ANC compared to the neutron one. Dividing $(\widetilde{C}^{^{41}\mathrm{Sc}}_{p^{40}\mathrm{Ca}37/27/2})^2$ by the CRF, $\mathcal{R}_2 = 0.0011$, we get the renormalized proton ANC at the neutron binding energy, $(\widetilde{C}^{^{41}\mathrm{Sc}}_{p^{40}\mathrm{Ca}37/27/2})^2/\mathcal{R}_2 = 18.18\,\mathrm{fm}^{-1}$. Finally, dividing it by the CRF, $\mathcal{R}_3 = 4.16$, defining the residual Coulomb effects, we get the square of the neutron ANC $(C^{^{41}\mathrm{Ca}}_{n\,^{40}\mathrm{Ca}37/27/2})^2 = 4.37\,\mathrm{fm}^{-1}$. These calculations clearly demonstrate the scale of the different CRFs leading to the difference between the mirror proton and neutron ANCs.

At the end of this section we note that although equation (2.30) is exact, the accuracy of the calculated ratio of the mirror depends on the quality of the overlap function. Contemporary microscopic methods can provide quite good overlap functions in the nuclear interior but not so good in the external region. The advantage of equation (2.30) is that it can be used in the region where the overlap functions are quite reliable and in this case the calculated ratio of the mirror ANCs is also quite accurate and can be predicted with accuracy of a few percent. Different examples were considered by Mukhamedzhanov (2012) including a case when the overlap function has a node in the nuclear interior.

2.1.3. ANCs and SFs.

The overlap function introduced above is not an eigenfunction of any Hermitian Hamiltonian and is not directly associated with a probability. Hence the overlap function is not normalized to unity. The square of the norm of the radial overlap function taking into account the antisymmetrization between the nucleons of nuclei A and x

$$\mathrm{SF}_{l_F j_F J_F} = \int_0^\infty \mathrm{d}r_{Ax}\, r_{Ax}^2\, [I^F_{Ax\, l_F j_F J_F}(r_{Ax})]^2 \tag{2.44}$$

is, by definition, the SF for the configuration $(xA)_{l_F j_F J_F}$ in F. Due to the antisymmetrization between A and x absorbed in $I^F_{xA\, l_F j_F J_F}(r_{xA})$, the SF in (2.54) can be larger than unity.

There is a principal difference between the ANC and the SF. The radial overlap function dies off exponentially as $r_{xA} \to \infty$, so the main contribution to the radial integral (2.44) comes from the nuclear interior, $r_{xA} < R_{NA}$ (only for loosely bound neutrons is the external contribution important). Thus, the SF is defined predominantly by the behavior of the radial overlap function within the nucleus. In contrast, the ANC describes the peripheral properties of the overlap function since it defines the amplitude of the tail. The ANC is, of course, coupled to the internal behavior of the nuclear wave function. In the shell model, the SF is a model-dependent quantity that is sensitive to the adopted potential and to the truncations inherent in the calculations (especially coupling to the continuum). In general the SF can differ from unity since it depends on the contribution of an infinite number of channels coupled to the two-body channel $(xA)_{l_F j_F J_F}$ plus antisymmetrization effects, but in the microscopic approach, the deviation of the SF from 1 is caused only by antisymmetrization effects that engage different nonorthogonal channels. Due to these effects, the SF calculated in microscopic approaches can be larger than 1.

In the single-particle approach, the radial overlap function is approximated by a single-particle overlap function

$$\begin{aligned} I^F_{xA\, l_F j_F J_F}(r_{xA}) &\approx I^{F\,(\mathrm{sp})}_{xA\; n_F l_F j_F J_F}(r_{xA}) \\ &= [\mathrm{SF}^{(\mathrm{sp})}_{n_F l_F j_F J_F}]^{1/2}\, \varphi_{n_F l_F j_F J_F}(r_{xA}), \end{aligned} \tag{2.45}$$

where $\varphi_{n_F l_F j_F J_F}(r_{xA})$ is the normalized single-particle radial wave function of the bound state (xA) calculated in an adopted $x - A$ interaction potential (often Woods–Saxon), $\mathrm{SF}^{(\mathrm{sp})}_{n_F l_F j_F J_F}$ is called the SF of the single-particle configuration $(xA)_{n_F l_F j_F J_F}$ described by $\varphi_{n_F l_F j_F J_F}(r_{xA})$, $\boldsymbol{r}_{xA}$ is the radius-vector connecting the centers of mass of nuclei x and A. However, strictly speaking, it is nothing more than the normalization coefficient connecting the amplitude of the tail of the overlap function (ANC) and the amplitude of the tail of the single-particle wave function (single-particle ANC). Equation (2.45) is an acceptable approximation if only one configuration $(xA)_{n_F l_F j_F J_F}$ gives a dominant contribution to the wave function of nucleus F.

The introduction of the single-particle wave function brings an additional dependence on the principal quantum number n_F which is absent in the left-hand side of (2.45). Equation (2.45) is used in the conventional DWBA analysis of experimental data. Since the squares of the norms of the overlap function and the radial bound-state wave function are, correspondingly, the SF, $\mathrm{SF}_{l_F j_F J_F}$, and unity, the single-particle SF in (2.45) will equal $\mathrm{SF}_{l_F j_F J_F}$ if the bound-state wave function and the overlap function have very similar radial behavior both in the nuclear interior and exterior. However, for $r < R_{xA}$ where both the overlap function and the single-particle wave function have most of their probability, the radial dependence of the overlap function and single-particle wave function, *a priori*, are different because the overlap function is a many-particle object, whereas the single-particle wave function is a solution of the single-particle Schrödinger equation. Thus, in general $\mathrm{SF}^{(\mathrm{sp})}_{n_F l_F j_F J_F}$does not coincide with the microscopically calculated SF, $\mathrm{SF}_{l_F j_F J_F}$. Nonetheless, for $r > R_{xA}$ the radial dependences of $I_{xAl_F j_F J_F}(r_{xA})$ and $\varphi_{n_F l_F j_F J_F}(r_{xA})$ are the same and they differ only by their overall normalizations. The asymptotic behavior of the radial overlap function is given by (2.13) and the asymptotic behavior of the radial bound-state wave function is defined as

$$\begin{aligned} \varphi_{n_F l_F j_F J_F}(r_{xA}) \;&\approx\; b_{n_F l_F j_F J_F}\, \frac{W_{-\eta_F,\, l_F+1/2}(2\kappa^F_{xA} r_{xA})}{r_{xA}} \\ &\xrightarrow{r_{xA}\to\infty}\; b_{n_F l_F j_F J_F}\, \frac{\mathrm{e}^{-\kappa_{xA} r_{xA}}}{r_{xA}^{1+\eta^{\mathrm{bs}}_{xA}}}, \end{aligned} \tag{2.46}$$

where $b_{n_B l_B j_B J_F}$ is the single-particle ANC. By the proper choice of $\mathrm{SF}^{(\mathrm{sp})}_{n_F l_F j_F J_F}$, one can make (2.55) exact for $r_{xA} > R_{xA}$. Then, comparing (2.13), (2.55) and (2.56) gives the relationship connecting the single-particle SF, the ANC, and the single-particle ANC $b_{n_F l_F j_F J_F}$

$$\mathrm{SF}^{(\mathrm{sp})}_{n_F l_F j_F J_F} = \frac{(C^F_{xAl_F j_F J_F})^2}{b^2_{n_F l_F j_F J_F}}. \tag{2.47}$$

Note that equation (2.47) can be used for another approximate estimate of the ratio of the mirror ANCs. Assuming that the SFs of the mirror nucleon states are the same, we immediately arrive at

$$\frac{(C^F_{pAl_F j_F J_F})^2}{(C^F_{nAl_F j_F J_F})^2} \approx \frac{b^2_{p\,n_F l_F j_F J_F}}{b^2_{n\,n_F l_F j_F J_F}}. \tag{2.48}$$

While the ANC is an experimentally measurable quantity, the single-particle ANC $b_{n_F l_F j_F J_F}$ is not. Hence, the single-particle SF, when defined by (2.47) is model dependent. Its model dependence comes through the single-particle ANC, which is a function of the geometric parameters, radius r_0 and diffuseness a of the Woods–Saxon potential conventionally used as a single-particle potential. Furthermore, note that, unlike $\mathrm{SF}_{l_F j_F J_F}$ as defined in (2.44), $\mathrm{SF}^{(\mathrm{sp})}_{n_F l_F j_F J_F}$ in (2.47) is actually a property of the peripheral part of the nucleon overlap function.

There is another important point to note about the difference between the ANCs and SFs. In *ab initio* calculations the overlap functions are model-dependent because the adopted NN potentials are not observable. Rather there exists an infinite number of the phase equivalent NN potentials, which are related to each other via finite-range unitary transformations. It has been shown (Mukhamedzhanov and Kadyrov 2009) that the ANCs, which are the amplitudes of the asymptotic tails of the overlap functions, are invariant under finite-range unitary transformations but SFs are not. Thus even on the fundamental level there is a difference between the ANCs and SFs. The fact that SFs are not an observable does not mean that they do not provide useful information, but we always should keep in mind that the SFs are model-dependent quantities.

2.1.4. Peripheral transfer reactions and ANCs. Since the ANC is the amplitude of the tail of the overlap function, the amplitude of the peripheral reaction containing the overlap function is proportional to the ANC. Hence by normalizing the calculated cross section of the peripheral reaction to the experimental one we can determine the ANC. Due to strong absorption in the nuclear interior, heavy ion induced reactions at energies around 10 MeV/nucleon are peripheral. This absorption in the DWBA is taken into account by using the optical potentials. It turns out that even reactions such as $A(^3\mathrm{He}, \mathrm{d})B$ induced by such light projectiles as ^{3}He are peripheral due again to strong absorption.

Here we present the theoretical scheme for analysis of peripheral charged particle transfer reactions to extract ANCs within the framework of the DWBA. The DWBA approach is based on the assumptions that (i) the simplest pole diagram describes the particle transfer mechanism, at least near the main peak in the angular distribution, (ii) rescattering effects of the interacting particles in the initial and final states must be taken into account. The DWBA amplitude for the transfer reaction $a + A \to s + F$ where $a = (sx)$ is given by

$$M^{\mathrm{DW}}(\boldsymbol{k}_f,\, \boldsymbol{k}_i) = \sum_{M_x} \Big\langle \chi^{(-)}_{\boldsymbol{k}_f} I^F_{xA} |\Delta V^{(\mathrm{post,prior})}| I^a_{sx}\, \chi^{(+)}_{\boldsymbol{k}_i} \Big\rangle. \tag{2.49}$$

Here, $\boldsymbol{k}_f = \boldsymbol{k}_{sF}$, $\boldsymbol{k}_i = \boldsymbol{k}_{aA}$, and

$$\boldsymbol{k}_{12} = \frac{m_2 \boldsymbol{k}_1 - m_1 \boldsymbol{k}_2}{m_1 + m_2} \tag{2.50}$$

is the relative momentum of particles 1 and 2. Also $\chi^{(+)}_{\boldsymbol{k}_i}$ and $\chi^{(-)}_{\boldsymbol{k}_f}$ are the distorted waves in the initial and final states, correspondingly,

$$\Delta V^{(\mathrm{post})} = V_{sx} + U_{sA} - U_{sF} \tag{2.51}$$

is the post-form of the DWBA transition operator and

$$\Delta V^{(\mathrm{prior})} = U_{sA} + V_{xA} - U_{aA} \tag{2.52}$$

is the prior form of the DWBA transition operator, V_{12} is the interaction potential of nuclei 1 and 2 equal to the sum of nuclear and Coulomb potentials, U_{12} is the optical interaction potential of nuclei 1 and 2. It is assumed that all the potentials depend only on the distance between the centers of mass of nuclei 1 and 2 and not on the coordinates of the constituent nucleons. The sum in (2.49) is taken over the spin projections M_x of the transferred particle x.

The DWBA is the first-order perturbation theory in powers of the transition operator. *A priori* this matrix element is not small in the nuclear interior where the operator $\Delta V^{(\mathrm{post,prior})}$ is not small. However the interior contributions are small due to the presence of the distorted waves, which suppress the nuclear interior contribution making transfer reactions dominantly peripheral if $|k_i - k_f|/k_i \ll 1$ and the energy is large enough to have many open channels at $l_{i,f} \leqslant k_{i,f} R_{i,f}$.

Using (2.45) the conventional DWBA amplitude is parametrized in terms of the product of the SFs of the initial and final nuclei leading to the DWBA differential cross section

$$\frac{\mathrm{d}\sigma}{\mathrm{d}\Omega} = \sum_{j_F j_a} \mathrm{SF}^{(\mathrm{sp})}_{n_F l_F j_F J_F}\, \mathrm{SF}^{(\mathrm{sp})}_{n_a l_a j_a J_a} \sigma^{\mathrm{DW}}_{n_F l_F j_F J_F n_a l_a j_a J_a}, \tag{2.53}$$

where $\sigma^{\mathrm{DW}}_{n_F l_F j_F J_F n_a l_a j_a J_a}$ is the reduced DWBA cross section. For simplicity, we assumed that only one value of l contributes to the reaction at each vertex. Since $\sigma^{\mathrm{DW}}_{n_F l_F j_F J_F n_a l_a j_a J_a}$ depends on the optical potential parameters and the geometric parameters of the Woods–Saxon potentials used to calculate the bound states, the extracted values of the phenomenological SFs are also model dependent. The parameters of the optical potentials are usually fixed by analysis of elastic scattering data. It is well known that the results of such an analysis are ambiguous. But if the reaction is peripheral, the influence of the ambiguity of the optical model parameters on the value of the phenomenological SFs is not very significant. The largest uncertainty in the absolute value of the SFs arises from the strong dependence of the calculated DWBA cross section $\sigma^{\mathrm{DW}}_{n_F l_F j_F J_F n_a l_a j_a J_a}$ on the geometric parameters, r_0 and a, of the bound-state Woods–Saxon potentials used to determine the single-particle orbitals, which cannot be determined unambiguously from experimental data. The normalization of the DWBA cross section in terms of SFs has another problem, especially manifested for surface reactions. The SF is defined mainly by the behavior of the overlap function in the nuclear interior, while the dominant contribution to peripheral reactions comes from the surface and outer regions of nuclei. Hence the parametrization of the DWBA cross section in terms of SFs is not justified for peripheral reactions. For these reactions only $r_{sx} > R_{sx}$ and $r_{xA} > R_{xA}$ contribute to the DWBA radial integrals, that is, bound-state wave functions can be approximated by their asymptotic forms (2.46) as

$$\frac{\varphi_{n_F l_F j_F J_F}(r_{xA})}{b_{n_F l_F j_F J_F}} \approx \frac{W_{-\eta^{\mathrm{bs}}_{xA},\; l_F+1/2}(2\kappa^F_{xA} r_{xA})}{r_{xA}},$$

$$\frac{\varphi_{n_a l_a j_a J_a}(r_{sx})}{b_{n_a l_a j_a J_a}} \approx \frac{W_{-\eta^{\mathrm{bs}}_{xA},\; l_a+1/2}(2\kappa^a_{sx} r_{sx})}{r_{sx}}, \tag{2.54}$$

and do not depend on the geometrical parameters of the bound-state potentials. Taking into account (2.47) and (2.53), we can rewrite the DWBA cross section for the peripheral transfer in the form

$$\frac{d\sigma}{d\Omega} = \sum_{j_F\, j_a} (C^{F}_{xAl_F\, j_F\, J_F})^2\, (C^{a}_{sxl_a\, j_a\, J_a})^2\, \frac{\sigma^{\rm DW}_{n_F l_F\, j_F\, J_F n_a l_a\, j_a\, J_a}}{b^2_{n_F l_F\, j_F\, J_F}\, b^2_{n_a l_a\, j_a\, J_a}}. \tag{2.55}$$

Due to (2.54),

$$R_{l_F\, j_F\, J_F l_a\, j_a\, J_a} = \frac{\sigma^{\rm DW}_{n_F l_F\, j_F\, J_F n_a l_a\, j_a\, J_a}}{b^2_{n_F l_F\, j_F\, J_F}\, b^2_{n_a l_a\, j_a\, J_a}} \tag{2.56}$$

is nearly independent of the single-particle ANCs $b_{n_a l_a\, j_a\, J_a}$ and $b_{n_F l_F\, j_F\, J_F}$ for peripheral reactions. Thus the introduction of condition (2.47) into the standard DWBA analysis guarantees the correct absolute normalization of the peripheral reaction cross section; it is actually parametrized in terms of the product of the square of the ANCs of the initial and final nuclei $(C^{F}_{xAl_F\, j_F\, J_F})^2\, (C^{a}_{sxl_a\, j_a\, J_a})^2$, rather than SFs. Furthermore, in this form, it is insensitive to the assumed geometries of the bound-state potentials.

The angular distributions of the heavy ion induced reactions at energies well above the Coulomb barrier are forward peaked and reactions are peripheral near the main peak in the angular distribution, where they are dominated by the peripheral partial waves $l_i > k_i R_i$, $l_f > k_f R_f$. Normalization of the DWBA differential cross section to the experimental one in the region of the main peak in the angular distribution allows one to determine $(C^{F}_{xAl_F\, j_F\, J_F})^2\, (C^{a}_{sxl_a\, j_a\, J_a})^2$. Equation (2.55) represents the basis for the determination of the product of the ANCs involved in a transfer reaction. In transfer reactions, two possibilities can occur. If a and F are the same nuclei, that is, we have an elastic exchange reaction, the DWBA cross section is expressed in terms of $(C^{a}_{sxl_a\, j_a\, J_a})^4$ and this ANC can be determined by normalizing the DWBA cross section to the experimental one. If $a$and F are different nuclei, then to determine $C^{F}_{xAl_F\, j_F\, J_F}$, one has to know $C^{a}_{sxl_a\, j_a\, J_a}$ from an independent measurement. Since the ANC is a model independent quantity, the ANC $C^{a}_{sxl_a\, j_a\, J_a}$ found from any other reliable experimental source—including those found from transfer reactions involving light or heavy ions or from analysis of elastic scattering—can be used in the subsequent DWBA analysis. Besides the ambiguity of the optical potential parameters, the ANCs determined from experiments using the DWBA analysis can be affected by coupling of the different channels which should be taken into account explicitly. It has been investigated in Nunes and Mukhamedzhanov (2001) and taken into account in Mukhamedzhanov *et al* (2003a).

2.2. Introduction to the THM

The THM is a powerful indirect technique that allows one to determine the astrophysical factor for rearrangement reactions. The THM, first suggested by Baur (1986), involves obtaining the cross section of the binary process $x + A \to b + B$ at astrophysical energies by measuring the Trojan Horse (TH) reaction (the two-body to three-body process ($2 \to 3$ particles)) $a + A \to b + B + s$ in the quasi-free (QF) kinematics regime, where the 'Trojan Horse' particle, $a = (s\,x)$, which has a dominant cluster structure, is accelerated at energies above the Coulomb barrier. After penetrating the barrier, the TH-nucleus a undergoes breakup leaving particle x to interact with target A while projectile s, also called a spectator, flies away. From the measured cross section of TH reaction, the energy dependence of the binary sub-process is determined.

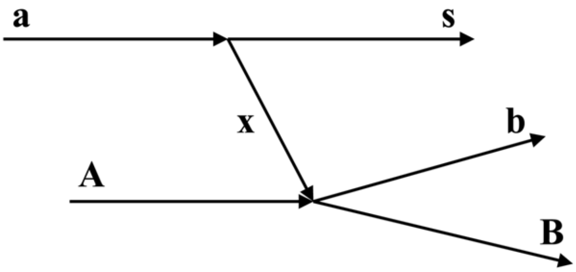

Figure 2. The diagram describing the TH reaction $a + A \to b + B + s$ in the QF kinematics.

The reaction used in the THM can proceed through different reaction mechanisms. The TH reaction mechanism shown schematically in figure 2, gives the dominant contribution to the cross section in a restricted region of the three-body phase space when the relative momentum of the fragments s and x is zero (the QF kinematical condition) or small compared to the bound state $(s\,x)$ wave number. Since the transferred particle x in the TH reaction is virtual, its energy and momentum are not related by the on-shell equation $E_x = k_x^2/(2m_x)$.

In the THM the initial channel is $a + A$, where $a = (sx)$, rather than just $x + A$. This results in three particles in the final state of the TH reaction, $b + B + s$, rather than the two-particle final state $b + B$ in the binary reaction. To increase the TH triple differential cross section the relative kinetic energy E_{aA} in the initial channel of the TH reaction should be higher than the Coulomb barrier between particles a and A. Then the probability to find nucleus a near A, which is given by the modulus square of the scattering wave function describing their relative motion, is not suppressed by the Coulomb barrier, leading to a finite probability that A can be in the proximity of x. Thus there is no additional Coulomb barrier between A and the constituent particle x of the TH-nucleus a, once the initial kinetic energy of the TH reaction is chosen to be above the $a + A$ Coulomb barrier. Usually the TH process is described as follows: the projectile a (or A), which is accelerated to an energy above the Coulomb barrier in the initial state of the TH reaction $V^{\rm CB}_{aA}$, approaches A and then breaks down in the vicinity of A. Particle x remains to interact with A while s leaves the scene as a spectator. To realize this, two additional conditions should be fulfilled. First, QF kinematics must be chosen so that the relative momentum of particles s and x is close to zero. This provides the best condition to treat s as a spectator because it minimizes the interaction between s and x by favoring the maximal distance between these particles. Second, the relative momentum k_{aA} of nuclei a and A in the entry channel of the TH reaction should be large enough that A will probe distances smaller than the distance between s and x available in the QF kinematics.

As we have noted, the Coulomb barrier suppresses the cross section at astrophysical energies making it difficult or practically impossible to measure in the laboratory. Yet another problem arises at low energies. Due to the electron screening, the Coulomb barrier penetrability increases compared to collisions of bare nuclei. Hence the results of direct measurements will be distorted by the electron screening (Assenbaum *et al* 1987, Strieder *et al* 2001). The advantage of the THM is that the extracted cross section of the binary sub-process does not contain the Coulomb barrier factor and electron screening does not play a role in the cross section. Consequently the TH cross section can be used to determine the energy dependence of the astrophysical factor, $S(E_{xA})$, of the binary process down to zero relative kinetic energy E_{xA} of the particles x and A without distortion due to electron screening (Spitaleri *et al* 2001, Lattuada *et al* 2001, La Cognata *et al* 2005). The absolute value of $S(E_{xA})$ can be found by normalization of TH data to available direct measurements at higher energies. At low energies where electron screening becomes important, comparison of the astrophysical factor determined from the THM to the direct result provides a determination of the screening potential (Spitaleri *et al* 2001, Lattuada *et al* 2001, La Cognata *et al* 2005).

The THM has been successfully applied to the bare-nucleus cross section measurements of reactions between charged particles at sub-Coulomb energies, as is discussed in a later section. The history leading to the THM comes from the theory of direct reactions (Shapiro 1967a, 1967b, 1968) and studies of the QF reaction mechanisms (Chew and Wick 1952, Furic *et al* 1972). It is an extension of the measurements of the excitation function of the three-body cross sections for QF reaction at low projectile incident energies (<70 MeV) (Lattuada *et al* 1984, 1985, Zadro *et al* 1989, Calvi *et al* 1990). A recent application of the THM has addressed the possibility of studying neutron-induced reactions at low energies on radioactive nuclei. This idea has been tested with stable beams (Tumino *et al* 2005, Gulino *et al* 2010, 2013). However, for neutron interactions, only the centrifugal barrier between the interacting nuclei exists.

In the next sections we present the theory of the TH reactions proceeding through direct and resonance binary sub-reactions. The first attempt to deliver the TH reaction theory has been done by Typel and Baur (2003), where they introduced the surface approximation. Although the idea of the surface approximation is quite attractive its practical realization requires the surface integral formalism developed in Kadyrov *et al* (2009), and has been applied to deuteron stripping reactions populating bound states and resonances by Mukhamedzhanov (2011). The developed theory of the deuteron stripping was based on DWBA and post continuum discretized coupled channels (CDCC) formalism, the surface integral formulation of the reaction theory, and the $R-$matrix method. This theory can be directly applied for analysis of the TH reactions, in which the TH-nucleus is a deuteron. It can be also extended for other TH-nuclei.

In the THM only the energy dependences and angular distribution of the three-body cross sections are measured. Normalization of the TH data is made to direct measurements available at higher energies. It allows one to determine the absolute cross sections at lower energies where direct data are not available. The absence of the absolute measurements allows us to consider the theory of the TH reactions in the plane-wave approximation (PWA), which often predicts reasonable energy dependence of the three-body cross sections (Dolinsky *et al* 1973) but is much simpler then the DWBA and CDCC approaches. In recent years, efforts have been devoted to the development of an improved THM approach that does not need the existence of direct data for normalization (La Cognata *et al* 2010a). This is of utmost importance in the case of reactions involving radioactive nuclei, since direct data are often missing or are plagued with large uncertainties. The equations presented here are obtained for the s-wave bound state $a = (sx)$.

2.2.1. Physics of the THM: QF kinematics.

Here, we describe some introductory physics of the THM, focusing on the kinematics of the 2→3 reaction $A + a \to b + B + s$ (see figure 2) that is used to determine the cross section of the $A + x \to b + B$ astrophysical reaction. To make the THM mechanism workable two conditions should be fulfilled. First, the QF kinematics should be chosen. At QF kinematics, the relative momentum of particles s and x vanishes. It provides the best condition to treat s as a spectator because it minimizes the interaction between s and x by favoring the maximal distances between these particles. The detection angles at the QF kinematics are called QF angles, and represent the best angular conditions where place detectors in a THM experiment, the probability to observe the QF mechanism being enhanced in comparison with non-QF processes.

This can be justified quantitatively. The amplitude of the diagram in figure 2 (equation (2.68)) depends on five independent Galilean invariant variables, but one of them, the rotation angle around the incident beam is not significant and can be excluded leaving only four independent invariants in the amplitude of the diagram in figure 2. These four invariants determine the complete kinematics of the THM reaction $A + a \to b + B + s$. Usually in THM experiments the angles and momenta of the final state particles b and B are measured.

Let us consider the diagram in figure 2 describing the THM mechanism. In what follows the momentum of the virtual particle x is denoted by $\boldsymbol{p}_x$ to distinguish it from on-the-energy-shell (OES) momentum $\boldsymbol{k}_x$. Also relative momentum of particles 1 and 2, where one of them is the virtual particle x, is denoted by $\boldsymbol{p}_{12}$ to distinguish it from the OES momentum $\boldsymbol{k}_{12}$ of particles 1 and 2. Then the relative kinetic energy between particles 1 and 2 is $E_{12} = k_{12}^2/2\mu_{12} \neq p_{12}^2/2\mu_{12}$, where μ_{12} is their reduced mass, $\boldsymbol{k}_j$ (E_j) stands for the momentum (energy) of the real particle j ($E_j = k_j^2/2m_j$).

From the energy and momentum conservation in the three-ray vertex $a \to s + x$ we get

$$\begin{aligned}\sigma_x &= E_x - \frac{p_x^2}{2m_x} = E_a - E_s - \varepsilon_{sx}^a - \frac{(\boldsymbol{k}_a - \boldsymbol{k}_s)^2}{2m_x}\\ &= -\left[\frac{p_{sx}^2}{2\mu_{sx}} + \varepsilon_{sx}^a\right] = E_{sx} - \frac{p_{sx}^2}{2\mu_{sx}} = -\frac{[p_{sx}^2 + (\kappa_{sx}^a)^2]}{2\mu_{sx}},\end{aligned} \tag{2.57}$$

where σ_x is the measure of the deviation of particle x from OES (for the real particle $\sigma_x = 0$), $E_{sx} = -\varepsilon^a_{sx}$, $\kappa^a_{sx} = \sqrt{2\mu_{sx}\varepsilon^a_{sx}}$ is the bound state $a = (s\,x)$ wave number, ε^a_{sx} is the binding energy for the virtual decay $a \to s + x$.

Similarly, from the energy and momentum conservation law in the $A + x \to b + B$ four-ray vertex we obtain

$$\sigma_x = E_{xA} - \frac{p^2_{xA}}{2\mu_{xA}}. \tag{2.58}$$

Then it is evident that, due to the virtual character of particle x, $E_{sx} \neq p^2_{sx}/2\mu_{sx}$ and $E_{xA} \neq p^2_{xA}/2\mu_{xA}$. The real particles are a and A in the entry channel and particles s, b and B in the exit channel, see figure 2. The relative momenta $\boldsymbol{p}_{sx}$ and $\boldsymbol{p}_{xA}$ are given by

$$\boldsymbol{p}_{sx} = \frac{m_x\boldsymbol{k}_s - m_s\boldsymbol{p}_x}{m_{sx}}, \tag{2.59}$$

and

$$\boldsymbol{p}_{xA} = \frac{m_A\boldsymbol{p}_x - m_x\boldsymbol{k}_A}{m_{xA}}. \tag{2.60}$$

The relative momentum of real particles is

$$\boldsymbol{k}_{12} = \frac{m_2\boldsymbol{k}_1 - m_1\boldsymbol{k}_2}{m_{12}}. \tag{2.61}$$

From equations (2.57) and (2.58) we get one of the important energy–momentum relationships of THM:

$$E_{xA} = \frac{p^2_{xA}}{2\mu_{xA}} - \frac{p^2_{sx}}{2\mu_{sx}} - \varepsilon^a_{sx}. \tag{2.62}$$

Thus in the THM, due to the virtual character of particle x, always we have $p^2_{xA}/(2\mu_{xA}) > E_{xA}$. In the QF kinematics, $p_{sx} = 0$ and the $x - A$ relative kinetic energy is

$$E_{xA} = \frac{p^{(0)2}_{xA}}{2\mu_{xA}} - \varepsilon^a_{sx}, \tag{2.63}$$

where $p^{(0)}_{xA}$ is the $x - A$ relative momentum in the QF kinematics.

We introduce the form factor (Blokhintsev *et al* 1977, 1984)

$$W_a(\boldsymbol{p}_{sx}) = \frac{1}{\sqrt{4\pi}} W_a(p_{sx}) = \int \mathrm{d}\boldsymbol{r}_{sx} \mathrm{e}^{\mathrm{i}\boldsymbol{p}_{sx}\cdot\boldsymbol{r}_{sx}} V_{sx}(r_{sx})\,\varphi_a(\boldsymbol{r}_{sx})$$
$$= -\frac{p^2_{sx} + (\kappa^a_{sx})^2}{2\,\mu_{sx}}\varphi_a(\boldsymbol{p}_{sx}), \tag{2.64}$$

where $\varphi_a(\boldsymbol{p}_{sx})$ is the Fourier transform of the bound-state wave function $\varphi_a(\boldsymbol{r}_{sx})$ of the bound state $a = (sx)$, $\boldsymbol{r}_{sx}$ is the radius-vector connecting the centers of mass of nuclei s and x, $V_{sx}(\boldsymbol{r}_{sx})$ is their interaction potential.

If one of the particles s or x is a neutron, the form factor is regular at $p^2_{sx} + (\kappa^a_{sx})^2 = 0$, that is

$$\varphi_a(\boldsymbol{p}_{sx}) = -2\,\mu_{sx}\frac{W_a(\boldsymbol{p}_{sx})}{p^2_{sx} + (\kappa^a_{sx})^2} \tag{2.65}$$

has a pole at $p^2_{sx} + (\kappa^a_{sx})^2 = 0$. However, if both particles s and x are charged, the potential V_{sx} includes both nuclear and Coulomb parts. The latter modifies the behavior of the form factor at $p^2_{sx} + (\kappa^a_{sx})^2 = 0$:

$$W_a(p_{sx}) \xrightarrow{p^2_{sx}+(\kappa^a_{sx})^2\to 0} [p^2_{sx} + (\kappa^a_{sx})^2]^{\eta_{sx}}\,\widetilde{W}_a(p_{sx}), \tag{2.66}$$

where $\widetilde{W}_a(p_{sx})$ is regular at the singular point, $\eta_{sx} = Z_s Z_x e^2 \mu_{sx}/\kappa^a_{sx}$ is the Coulomb parameter of the bound state (sx), $Z_i e$ is the charge of particle i. We remind that we use the system of units in which $\hbar = c = 1$. Hence, the Fourier component of the bound-state wave function and, correspondingly, the amplitude of the diagram in figure 2 have the branching point singularity rather than the pole one:

$$\varphi_a(\boldsymbol{p}_{sx}) \xrightarrow{p^2_{sx}+(\kappa^a_{sx})^2\to 0} -2\,\mu_{sx}\frac{\widetilde{W}_a(\boldsymbol{p}_{sx})}{[p^2_{sx} + (\kappa^a_{sx})^2]^{1-\eta_{sx}}}. \tag{2.67}$$

Hence the amplitude of the diagram 2.2 is not a pole one in the presence of the Coulomb interaction in the vertex $a \to s + x$. Only if one of the particles s or x is a neutron, that is $\eta_{sx} = 0$, the singularity at $p^2_{sx} + (\kappa^a_{sx})^2 = 0$ turns into a pole, and in this case the diagram 2.2 can be called a pole diagram.

Although the singularity at $p^2_{sx} + (\kappa^a_{sx})^2 = 0$ is located in the unphysical region, owing to its presence for the orbital angular momentum of the bound state $l_{sx} = 0$ (this is the most common condition in the application of THM, compare table 6) the amplitude $M(\boldsymbol{k}_{bB}, \boldsymbol{p}_{xA}; \boldsymbol{p}_{sx})$ has a maximum at $p_{sx} = 0$, although the Coulomb $s - x$ interaction decreases the QF peak making it even disappear at $\eta_{sx} > 1$. Thus the QF kinematics provides the best condition for the dominance of the diagram in figure 2.

The second condition is that the relative momentum k_{aA} of nuclei a and A in the entry channel of the THM reaction should be large enough (typically $k_{aA} > \kappa^a_{sx}$), so that A will probe distances smaller than the distances between s and x available in the QF kinematics. However, astrophysical energies E_{xA} still can be reached and even the negative (sub-threshold) energy region can be investigated using the THM that follows from equation (2.60). We can see that the binding energy ε^a_{sx} of the Trojan Horse particle $a = (sx)$ plays an important role compensating the first term $p^{(0)2}_{xA}/2\mu_{xA}$ and bringing down E_{xA} so that we can reach the astrophysical region.

2.2.2. *Theory of the THM for direct binary sub-reactions.*

Starting with the PWA in the prior form, let us consider the TH reactions proceeding through direct binary sub-reactions. First we neglect the spins of the particles, which will be taken into account later. We start from the prior form of the PWA:

$$M^{\mathrm{PWA(prior)}}(P, \boldsymbol{k}_{aA}) = \left\langle \chi^{(0)}_{sF}\Psi^{(-)}_{bB}|V_{xA}|\varphi_a\varphi_A\chi^{(0)}_{aA}\right\rangle, \tag{2.68}$$

where $\chi^{(0)}_{aA} = \mathrm{e}^{\mathrm{i}\,\boldsymbol{k}_{aA}\cdot\boldsymbol{r}_{aA}}$ and $\chi^{(0)}_{sF} = \mathrm{e}^{\mathrm{i}\,\boldsymbol{k}_{sF}\cdot\boldsymbol{r}_{sF}}$, $\Psi^{(-)}_{bB}$ is the scattering wave function of the fragments b and B in the exit channel, $F = b + B$. The prior form looks more preferable than the post-form because it does not contain the interaction potential of the exiting particle s, allowing us to treat it as a spectator. Expressing $\boldsymbol{r}_{aA}$ and $\boldsymbol{r}_{sF}$ in terms of $\boldsymbol{r}_{sx}$ and $\boldsymbol{r}_{xA}$

$$\boldsymbol{r}_{aA} = \boldsymbol{r}_{xA} + \frac{m_s}{m_a}\boldsymbol{r}_{sx}, \qquad \boldsymbol{r}_{sF} = \frac{m_A}{m_F}\boldsymbol{r}_{xA} + \boldsymbol{r}_{sx}, \tag{2.69}$$

we get

$$M^{\mathrm{PWA(prior)}}(P,\,\boldsymbol{k}_{aA}) = M^{\mathrm{HOES}}_{xA\to bB}(\boldsymbol{k}_{bB},\,\boldsymbol{p}_{xA})\varphi_a(\boldsymbol{p}_{sx}). \qquad (2.70)$$

Here

$$M^{\mathrm{HOES}}_{xA\to bB}(\boldsymbol{k}_{bB},\,\boldsymbol{p}_{xA}) = \left\langle \Psi^{(-)}_{bB} | V_{xA} | \varphi_A \mathrm{e}^{\mathrm{i}\,\boldsymbol{p}_{xA}\cdot \boldsymbol{r}_{xA}} \right\rangle \qquad (2.71)$$

is the HOES (half-off the energy shell) amplitude of the binary sub-reaction $x + A \to b + B$,

$$\boldsymbol{p}_{sx} = \boldsymbol{k}_{sF} - \frac{m_s}{m_a}\,\boldsymbol{k}_{aA}, \qquad \boldsymbol{p}_{xA} = \boldsymbol{k}_{aA} - \frac{m_A}{m_F}\,\boldsymbol{k}_{sF}. \qquad (2.72)$$

This HOES amplitude should be compared with the OES (on the energy shell) amplitude of the sub-reaction

$$M^{\mathrm{OES}}_{xA\to bB}(\boldsymbol{k}_{bB}, \boldsymbol{p}_{xA}) = \left\langle \Psi^{(-)}_{bB} | V_{xA} | \varphi_A \mathrm{e}^{\mathrm{i}\boldsymbol{k}_{xA}\cdot \boldsymbol{r}_{xA}} \right\rangle. \qquad (2.73)$$

Here we assume that the Coulomb $x - A$ interaction is screened so that we can avoid the distorted wave in the initial channel of the reaction. Equation (2.71) is exact if $\Psi^{(-)}_{bB}$ is the exact scattering wave function in the exit channel $b + B$ of the binary sub-reaction and antisymmetrization is neglected.

Compare now equations (2.71) and (2.73) near the QF kinematics. At $E_{xA} \gg \varepsilon^{a}_{sx}$ from equation (2.63) we get that $E_{xA} \approx p^2_{xA}/2\mu_{xA}$ and $p_{xA} \approx k_{xA} = \sqrt{2\mu_{xA}E_{xA}}$. Hence the HOES amplitude $M^{\mathrm{HOES}}_{xA\to bB}(\boldsymbol{k}_{bB},\,\boldsymbol{p}_{xA}) \approx M^{\mathrm{OES}}_{xA\to bB}(\boldsymbol{k}_{bB},\,\boldsymbol{k}_{xA})$. However, practical applications of the THM are most important at $E_{xA} \to 0$. At low energies the barrier penetrability factor becomes one of the most crucial factors determining the behavior of the OES reaction amplitude. Using the two-potential equation we can rewrite (2.73) as

$$M^{\mathrm{OES}}_{xA\to bB}(\boldsymbol{k}_{bB},\,\boldsymbol{k}_{xA}) = \left\langle \Psi^{(-)}_{bB} | V_{xA} - U_{xA} | \varphi_A\, \chi^{(+)}_{\boldsymbol{k}_{xA}} \right\rangle, \qquad (2.74)$$

where $\chi^{(+)}_{\boldsymbol{k}_{xA}}$ is $x - A$ distorted wave generated by the optical potential U_{xA}. Now after introducing the distorted wave in the initial channel we can use in equation (2.74) the unscreened Coulomb potential U^{C}_{xA}. Applying the partial wave expansion of $M^{\mathrm{OES}}_{xA\to bB}(\boldsymbol{k}_{bB},\,\boldsymbol{k}_{xA})$, we immediately see that each partial wave amplitude contains the penetrability factor in the initial $x - A$ channel generated by the distorted waves $\chi^{(+)}_{k_{xA},l}$. At low E_{xA} energies the penetrability factors suppress the contribution of higher partial waves singling out only one or a few lowest partial waves. However we cannot use the two-potential formula in (2.71) because $p_{xA} \neq k_{xA}$ and the penetrability factors do not appear in the HOES amplitude (2.71). Hence, the number of the partial waves contributing to the HOES amplitude may be much larger than the ones contributing to the OES. Only in special cases such as resonant binary reactions, when only one or a few partial waves do contribute, or for direct reactions when a large $Q = m_x + m_A - m_b - m_B$ singles out only the lowest allowed partial wave, can the HOES amplitude provide the same information as the OES one even at low energies. In many papers devoted to the analysis of the THM data, a simplified version of the theory is used (see Pizzone *et al* (2013) and Gulino *et al* (2013) and references therein). Assume that only one partial wave in the initial $x + A$ channel does contribute to the reaction (it is the case for the resonant $x + A \to b + B$ reaction). The HOES amplitude obtained from equation (2.69) by partial wave expansion of the initial plane wave $\mathrm{e}^{\mathrm{i}\boldsymbol{p}_{xA}\boldsymbol{r}_{xA}}$ contains the spherical Bessel function $j_l(p_{xA}r_{xA})$ at the resonant partial wave l. At small $E_{xA}(E_{xA} \ll \varepsilon^{d}_{pn})$, according to equations (2.63), $p_{xA} \gg k_{xA}$ and $j_l(p_{xA}r_{xA})$ changes little when $E_{xA} \to 0$ practically not affecting the energy dependence of the HOES matrix element. The OES matrix element contains the distorted wave $\chi^{(+)}_{k_{xA}l}(r_{xA})$ in the initial state, whose energy behavior at small E_{xA} is almost entirely determined by the penetrability factor $P_l(k_{xA}r_{xA})$. Removing this penetrability factor, which is needed to obtain the astrophysical factor, we obtain a weak energy dependence of the initial distorted wave, as in the case of the HOES matrix element. Because both the HOES and OES matrix elements contain the same final channel scattering wave function, one expects that the energy behavior at small E_{xA} of the HOES matrix element is similar to the OES one with the penetrability removed from the OES cross section. Furthermore the absolute values of the HOES and OES cross sections under this condition may be quite different but in the THM only the energy dependence of the binary sub-reaction cross section is measured and its absolute value is determined by normalization of the TH differential cross section to the available direct experimental data at higher energies. This discussion provides a qualitative justification for the simplified analysis of the TH data, in which the TH triple differential cross section of the TH reaction $x + A \to s + b + B$ is related to the differential cross section for the binary sub-reaction $x + A \to b + B$ as shown in section 4 below, see equation (4.1).

Now we outline a more accurate approach, which is based on the surface integral formalism and the PWA. At low E_{xA} we need to consider the TH amplitude in more detail to investigate whether we can single out the OES shell amplitude of the binary sub-reaction from the TH amplitude of the actual TH reaction and estimate how important the off-shell effects are. To this end the surface integral formalism (Kadyrov *et al* 2009, Mukhamedzhanov 2011) can be used, which allows us to express the TH amplitude in terms of the OES amplitude for the binary sub-reaction and the HOES term.

Following Mukhamedzhanov (2011) we can get for the prior HOES reaction amplitude in the PWA:

$$\begin{aligned} M^{\mathrm{PWA(prior)}}(P,\,\boldsymbol{k}_{aA}) \approx{}& -\mathrm{i}4\pi^2\sqrt{\frac{R_{xA}}{k_{bB}\mu_{bB}\mu_{xA}}}\,\varphi_a(\boldsymbol{p}_{sx}) \\ &\times \sum_{J_F M_F j' l l' m_{j'} m_l m_{l'} M_x} \mathrm{i}^{l+l'} \langle j m_j l m_l | J_F M_F \rangle \\ &\times \left\langle j' m_{j'} l' m_{l'} | J_F M_F \right\rangle \left\langle J_x M_x J_A M_A | j' m_{j'} \right\rangle \\ &\times \langle J_s M_s J_x M_x | J_a M_a \rangle\, Y_{l m_l}(-\hat{\boldsymbol{k}}_{bB}) Y^{*}_{l' m_{l'}}(\hat{\boldsymbol{p}}_{xA}) \qquad (2.75) \\ S^{J_F}_{bBjl;xAj'l'}\, P^{-1/2}_{l'}&(k_{xA},\,R_{xA})\mathrm{e}^{\mathrm{i}\delta^{hs}_{xAl'}} \Bigg\{ j_{l'}(p_{xA}R_{xA}) \\ &\times \Big[[B_{xAl'}(k_{xA},\,R_{xA}) - 1] - D_{xAl'}(p_{xA},\,R_{xA}) \Big] \\ &+ 2Z_x Z_A e^2 \mu_{xA} \int_{R_{xA}}^{\infty} \mathrm{d}r_{xA}\, \frac{O_{l'}(k_{xA},\,r_{xA})}{O_{l'}(k_{xA},\,R_{xA})}\, j_{l'}(p_{xA}r_{xA}) \Bigg\}. \end{aligned}$$

Here, $S^{J_F}_{bBjl;xAj'l'}$ is the OES S-matrix elements for the binary sub-reaction $x + A \to b + B$, R_{xA} is the channel radius in the channel $x + A$ and

$$B_{xAl'} = R_{xA}\frac{\frac{\partial O_{l'}(k_{xA},r_{xA})}{\partial r_{xA}}\big|_{r_{xA}=R_{xA}}}{O_{l'}(k_{xA},\,R_{xA})} \tag{2.76}$$

is the logarithmic derivative like in the R-matrix method. Recall that we use the system with $\hbar = c = 1$.

We also used the equation for the outgoing spherical wave

$$O_{l'}(k_{xA},\,R_{xA}) = \sqrt{F_{l'}^2(k_{xA},\,R_{xA}) + G_{l'}^2(k_{xA},\,R_{xA})}$$
$$\times \mathrm{e}^{\mathrm{i}\tan^{-1}\left[\frac{F_{l'}(k_{xA},R_{xA})}{G_{l'}(k_{xA},R_{xA})}\right]}\mathrm{e}^{-\mathrm{i}\omega_{xAl'}} = \sqrt{\frac{k_{xA}R_{xA}}{P_{l'}(k_{xA},\,R_{xA})}}\mathrm{e}^{\mathrm{i}\delta_{xAl'}^{hs}}. \tag{2.77}$$

The logarithmic derivative is

$$D_{xAl'}(p_{xA},\,R_{xA}) = R_{xA}\frac{\frac{\partial j_{l'}(p_{xA},r_{xA})}{\partial r_{xA}}\big|_{r_{xA}=R_{xA}}}{j_{l'}(p_{xA},\,R_{xA})},$$

where $F_l(k_{xA},\,R_{xA})$ and $G_l(k_{xA},\,R_{xA})$ are the Coulomb regular and singular solutions, correspondingly, $j_l(p,\,r)$ is the spherical Bessel function,

$$P_l(k_{xA},\,R_{xA}) = \frac{k_{xA}R_{xA}}{F_{l'}^2(k_{xA},\,R_{xA}) + G_{l'}^2(k_{xA},\,R_{xA})} \tag{2.78}$$

is the barrier penetrability factor. Also the factor $\omega_{xAl} = \sum_{n=1}^{l}\eta_{xA}/\eta_{xA}$, and the term

$$\delta_{xAl}^{hs} = \tan^{-1}\left[\frac{F_l(k_{xA},\,R_{xA})}{G_l(k_{xA},\,R_{xA})}\right] - \omega_{xAl}$$

is the solid sphere scattering phase shift, η_{xA} is the Coulomb parameter in the $x + A$ channel. Note that this definition differs from the one used in Lane and Thomas (1958).

Thus using the surface integral formalism we succeeded to transform the TH reaction amplitude in the PWA into the sum of two amplitudes, the surface term and the external term containing the integral over r_{xA} in the external region. Both terms are expressed in terms of the OES S-matrix elements for the binary sub-reaction. The surface term contains the logarithmic derivative of the outgoing spherical wave resembling the R-matrix method. A small internal term was neglected. Equation (2.75) can be used to analyze the TH reaction proceeding through direct binary sub-reaction.

There is one important point to discuss. As one can see from (2.75), the presence of the factor $P_{l'}^{-1/2}(k_{xA},\,R_{xA})$ eliminates the penetrability factor in the channel $x + A$ of the S-matrix element $S_{bBjl;xAj'l'}^{J_F}$, which is the entry channel of the binary sub-reaction. The absence of the penetrability factor in this entry channel is the main advantage of the TH method, which allows one to measure the astrophysical factor of the binary reaction down to zero E_{xA} energy.

However, the absence of the penetrability factor has a negative side. The penetrability factor in the entry channel of the binary reaction singles out only one or a few of the smallest partial waves l'. Its absence leads to the contribution of many partial waves. Hence, the astrophysical factor determined from the TH reaction for direct binary sub-reactions may deviate from the OES astrophysical factor extracted from direct measurements. Hence, only if there are special kinematical conditions, which single out only the lowest partial waves l' in the binary sub-reaction of the TH reaction, the TH method can provide the same astrophysical factor as direct measurements.

2.2.3. Theory of the THM for resonant binary sub-reactions.

In this section we consider reactions proceeding through resonant binary sub-reactions. A general formalism for (d, p) reactions populating resonance states based on the CDCC/DWBA and the surface integral formalism is given by Mukhamedzhanov (2011). Here we present the TH reaction amplitude in the PWA using the surface integral formalism previously applied in Kadyrov *et al* (2009) and Mukhamedzhanov (2011). While only neutron transfer was considered by Mukhamedzhanov (2011), here we consider transfer of a charged particle.

As in the previous section, we consider only the s-wave bound state $a = (sx)$ and neglect the internal degrees of freedom of the transferred particle x. Because only the energy dependence of the TH cross sections has been measured, often a simple PWA is enough to analyze the TH reactions. Following Mukhamedzhanov (2011) we get for the prior PWA amplitude of the TH reaction proceeding through the resonance binary sub-reaction:

$$\begin{aligned}
M^{\mathrm{PWA(prior)}}(P,\,\boldsymbol{k}_{aA}) \;&=\; (2\pi)^2\sqrt{\frac{1}{\mu_{bB}k_{bB}}}\varphi_a(\boldsymbol{p}_{sx})\\
&\times \sum_{J_FM_Fj'll'm_{j'}m_lm_{l'}M_n} i^{l+l'}\left\langle jm_jlm_l|J_FM_F\right\rangle\left\langle j'm_{j'}l'm_{l'}|J_FM_F\right\rangle\\
&\times \left\langle J_xM_xJ_AM_A|j'm_{j'}\right\rangle\langle J_sM_sJ_xM_x|J_aM_a\rangle\,\mathrm{e}^{-\mathrm{i}\delta_{bBl}^{hs}}Y_{lm_l}(-\hat{\boldsymbol{k}}_{bB})\\
&\times \sum_{\nu,\tau=1}^{N}[\Gamma_{\nu bBjlJ_F}(E_{bB})]^{1/2}[\boldsymbol{A}^{-1}]_{\nu\tau}Y_{l'm_{l'}}^{*}(\hat{\boldsymbol{p}}_{xA})\\
&\times \sqrt{\frac{R_{xA}}{\mu_{xA}}}[\Gamma_{\nu xAl'j'J_F}(E_{xA})]^{1/2}P_{l'}^{-1/2}(k_{xA},\,R_{xA})(j_{l'}(p_{xA}R_{xA})\\
&\times[(B_{xAl'}(k_{xA},\,R_{xA}) - 1) - D_{xAl'}(p_{xA},\,R_{xA})]\\
&+ 2Z_xZ_Ae^2\mu_{xA}\int_{R_{xA}}^{\infty}\mathrm{d}r_{xA}\frac{O_{l'}(k_{xA},\,r_{xA})}{O_{l'}(k_{xA},\,R_{xA})}j_{l'}(p_{xA}r_{xA})).
\end{aligned} \tag{2.79}$$

Here, N is the number of the levels included, $\Gamma_{\nu bBjlJ_F}(E_{bB})$ is the partial resonance width of the νth level in the channel $(b + B)_{ljJ_F}$. The internal part contribution is neglected in equation (2.79). This equation allows one to treat both multi-level (interfering) and single-level two-channel cases (non-interfering resonances). It expresses the TH resonance reaction amplitude in terms of partial resonance widths (reduced widths amplitudes), boundary conditions and matrix elements $[\boldsymbol{A}^{-1}]_{\nu\tau}$ of the inverse level matrix $\boldsymbol{A}^{-1}$ used in the R-matrix approach (Lane and Thomas 1958). The generalization of the R-matrix approach is evident because we consider 2 → 3 particles TH resonant reactions, which are more complicated than resonant binary reactions, for which a conventional R-matrix approach has been developed. In the TH reaction the complication is caused by the presence of the TH-nucleus

a in the initial states, which carries the transferred particle x, and the spectator s in the final state. The $a - A$ interaction in the initial state and the $s - F$ interaction in the final state can be conventionally treated within the distorted wave (DWBA) or more advanced CDCC formalism, but here, aiming for the application for the THM, we presented the TH resonance reaction amplitude in the PWA, where the initial and final state distorted waves are replaced by the corresponding plane waves. This implies the need to normalize the THM-extracted cross section to the direct one to get the absolute indirect cross section.

2.3. Coulomb excitation and dissociation

The theory of Coulomb excitation at low energies ($E_{\mathrm{lab}} < 20\,\mathrm{MeV/nucleon}$) is very well understood (Alder and Winther 1975), and has been used for a long time to analyze experiments on multiple excitations and reorientation effects (Cline 1988). For Coulomb excitation of relativistic heavy ions another accurate semiclassical theory exists (Winther and Alder 1979). In this case, the kinematics is characterized by straight-line trajectories and retardation effects due to special relativity are fully taken into account. A quantum mechanical theory for relativistic Coulomb excitation has also been developed (Bertulani and Baur 1985, Bertulani and Nathan 1993), which includes diffraction and absorptive effects. For collisions at intermediate energies ($20 < E_{\mathrm{lab}} < 200\,\mathrm{MeV/nucleon}$) a combination of retardation effects and relativistic corrections of the Rutherford trajectories are necessary for a proper description of the Coulomb excitation mechanism (Aleixo and Bertulani 1989).

In Coulomb excitation experiments at energies above the Coulomb barrier, one indirectly selects impact parameters b that exceed the sum of the radii of the two colliding nuclei, often via restrictions to observe scattering at small angles. This allows the selection of collisions at 'safe' distances, minimizing possible contributions to the excitation from nuclear interactions. Most Coulomb excitation experiments performed at rare isotope beam facilities to date have been done at intermediate bombarding energies, around 50–100 MeV/nucleon. Then both relativistic and quantum scattering effects are of relevance. At these facilities, Coulomb excitation has been proven to be a very important tool to extract information on electromagnetic properties of nuclear transitions with relevance for nuclear structure as well as for nuclear astrophysics (Aumann 2006).

2.3.1. First-order perturbation theory. Because nuclei are nearly spherical, the theory of Coulomb excitation is best described by performing a multipole expansion of the electromagnetic field of a projectile nucleus with charge Z_P as it evolves along a classical Rutherford trajectory. In most situations of interest, the Coulomb excitation process can be treated in perturbation theory. Using first-order time-dependent perturbation theory one gets

$$\frac{\mathrm{d}\sigma_{i\to f}}{\mathrm{d}\Omega} = \left(\frac{\mathrm{d}\sigma_{\mathrm{elastic}}}{\mathrm{d}\Omega}\right)\frac{16\pi^2 Z_P^2 e^2}{\hbar^2} \times \sum_{\Pi LM}\frac{B\left(\Pi L;\, I_i \to I_f\right)}{(2L+1)^3}\left|S\left(\Pi LM\right)\right|^2 \tag{2.80}$$

where $B\left(\Pi L, I_i \to I_f\right)$ is the reduced transition probability for the target nucleus, $\Pi L = E1, E2, M1, \ldots$ is the multipolarity of the excitation, and $M = -L, -L+1, \ldots, L$ is the total magnetic quantum number.

The reduced transition probabilities are given by

$$B\left(\Pi L;\, I_i \to I_f\right) = \frac{1}{2I_i+1}\sum_{M_i M_f}\left|\left\langle I_f M_f\left|m(\Pi LM)\right| I_i M_i\right\rangle\right|^2 \tag{2.81}$$

where $M = M_i - M_f$.

The nuclear matrix elements, with nuclear structure information for the transition from the initial to the final state is

$$\mathrm{M}\left(ELM\right) = \frac{(2L+1)!!}{\kappa^{L+1}c\,(L+1)} \times \int \boldsymbol{j}(\boldsymbol{r})\cdot\nabla\times\boldsymbol{L}\left[j_L(\kappa r)Y_{LM}(\hat{\boldsymbol{r}})\right]\mathrm{d}^3r \tag{2.82}$$

for electric (E) transitions, and

$$\mathrm{M}\left(MLM\right) = -\mathrm{i}\frac{(2L+1)!!}{\kappa^{L}c\,(L+1)} \times \int \boldsymbol{j}(\boldsymbol{r})\cdot\boldsymbol{L}\left[j_L(\kappa r)Y_{LM}(\hat{\boldsymbol{r}})\right]\mathrm{d}^3r \tag{2.83}$$

for magnetic (M) transitions.

Here $\kappa = \omega/c$ is the photon wavenumber, $\boldsymbol{j}(\boldsymbol{r})$ is the electric current density in the excited nucleus, j_L are spherical Bessel functions and Y_{LM} are spherical harmonics.

The orbital integrals $S(\Pi LM)$ contain the information on the dynamics of the reaction (Alder and Winther 1975, Bertulani and Baur 1985). Later, it was shown that including retardation and Coulomb recoil, they become (Aleixo and Bertulani 1989)

$$\begin{aligned} S(\mathrm{E}LM) = {} & -\frac{\mathrm{i}\kappa^{L+1}}{L\,(2L-1)!!} \times \int \frac{\partial}{\partial r'}\left\{r'(t)h_L^{(1)}[\kappa r'(t)]\right\}Y_{LM}\left[\theta'(t),\phi'(t)\right]\mathrm{e}^{\mathrm{i}\omega t}\,\mathrm{d}t \\ & -\frac{\kappa^{L+2}}{cL\,(2L-1)!!}\int \boldsymbol{v}'(t)\cdot\boldsymbol{r}'(t)h_L^{(1)}[\kappa r'(t)] \\ & \times Y_{LM}\left[\theta'(t),\phi'(t)\right]\mathrm{e}^{\mathrm{i}\omega t}\,\mathrm{d}t, \end{aligned} \tag{2.84}$$

and

$$S(\mathrm{E}LM) = -\frac{\mathrm{i}}{\gamma\mu c}\frac{\kappa^{L+1}}{L\,(2L-1)!!} \cdot\boldsymbol{L}_0\int\nabla'\left\{h_L^{(1)}[\kappa r'(t)]Y_{LM}\left[\theta'(t),\phi'(t)\right]\right\}\mathrm{e}^{\mathrm{i}\omega t}\,\mathrm{d}t, \tag{2.85}$$

where v is the relative velocity, $r'(t)$ is the classical relative motion trajectory as a function of time,

$$L_0 = \gamma a\mu v\cot\left(\vartheta/2\right) \tag{2.86}$$

is the (constant) relative angular momentum, ϑ is the center-of-mass scattering angle, $\gamma = \left(1 - v^2/c^2\right)^{-1/2}$ is the Lorentz factor, μ is the reduced mass, and $a = Z_P Z_T e^2/\left(\gamma \mu v^2\right)$ is the distance of closest approach in a head-on collision.

Inclusion of absorption effects in S(ΠLM) due to the imaginary part of an optical nucleus–nucleus potential were worked out by Bertulani and Nathan (1993). This allows the description of diffraction patterns in the differential cross sections. The orbital integrals depend on the multipolarity ΠLM and on the adiabaticity parameter $\xi(b) = \omega b/\gamma v$, where $\omega = E_x/\hbar$ and E_x is the excitation energy, and b is the impact parameter. It is worthwhile to mention that in rare isotope facilities one is interested in the excitation of the projectile, which is often a radioactive nucleus. In this case, the variables associated to the projectile and the target are exchanged in the above equations—the target is the source of the time-dependent electromagnetic interaction.

Because the Coulomb excitation process is an external process, i.e., it occurs when the nuclei are outside the range of the nuclear forces between them, the matrix elements probed in Coulomb excitation are the same as those probed with real photons (except for the $E0$ multipolarity, which contributes very little). Therefore, Coulomb excitation cross sections are directly related to the photonuclear cross sections by means of the equation (Bertulani and Baur 1985),

$$\frac{\mathrm{d}\sigma}{\mathrm{dE}_x} = \frac{1}{E_x}\sum_L \Big[n_{\gamma EL}(E_x)\,\sigma_{\gamma EL}(E_x) + n_{\gamma ML}(E_x)\sigma_{\gamma ML}(E_x)\Big], \qquad (2.87)$$

where $\sigma_{\gamma EL}(E_x)$ and $\sigma_{\gamma ML}(E_x)$ are the photonuclear cross sections for EL and ML excitations with photon energy E_x, respectively. The functions $n_{\gamma \Pi L}(E_x)$ are known as virtual photon numbers for the ΠL multipolarity. While for a real photon all multipolarities are mixed with the same weight, in Coulomb excitation they are weighted with the virtual photon numbers.

The photonuclear cross sections are related to the reduced matrix elements, and the excitation energy E_x, through the relation (Bertulani and Baur 1985)

$$\sigma_{\gamma \Pi L}(E_x, \theta) = \frac{(2\pi)^3 (L+1)}{\mathrm{L}\left[(2L+1)!!\right]^2}\left(\frac{E_x}{\hbar c}\right)^{2L-1} \frac{\mathrm{d}B(\Pi L, E_x)}{\mathrm{d}E_x}, \qquad (2.88)$$

where $\mathrm{d}B/\mathrm{d}E_x$ are the electromagnetic response functions dependent for each excitation energy E_x and related to the transition reduced matrix elements by

$$B\left(\Pi LM; I_i \to I_f\right) = \int \mathrm{d}E_x \frac{\mathrm{d}B(\Pi L, E_x)}{\mathrm{d}E_x}. \qquad (2.89)$$

A similar expression is valid for the angle differential cross sections

$$\frac{\mathrm{d}\sigma(E_x)}{\mathrm{d}\Omega} = \frac{1}{E_x}\sum_L \left[\frac{\mathrm{d}n_{\gamma EL}(E_x,\theta)}{\mathrm{d}\Omega}\sigma_{\gamma EL}(E_x) + \frac{\mathrm{d}n_{\gamma ML}(E_x,\theta)}{\mathrm{d}\Omega}\sigma_{\gamma ML}(E_x)\right], \qquad (2.90)$$

where Ω denotes the solid scattering angle.

Due to the common use of high-energy (above the Coulomb barrier) projectiles in rare isotope facilities, it is important to account for strong absorption properly. The proper formalism for Coulomb excitation in high-energy collisions was developed by Bertulani and Nathan (1993). They have shown that the virtual photon numbers in equation (2.90) are given by

$$\frac{\mathrm{d}n_{\gamma \Pi L}(E_x,\theta)}{\mathrm{d}\Omega} = Z_P^2 \alpha \left(\frac{\omega k}{\gamma v}\right)^2 \frac{\mathrm{L}\left[(2L+1)!!\right]^2}{(2\pi)^3 (L+1)} \times \sum_M \left|G_{\Pi LM}(c/v)\right|^2 \left|\Omega_M(q)\right|^2, \qquad (2.91)$$

where $\alpha = e^2/\hbar c$ and

$$\Omega_M(q) = \int_0^\infty \mathrm{d}b\, b\, J_M(qb)\, K_M\left(\frac{\omega b}{\gamma v}\right) \mathrm{e}^{\mathrm{i}\chi(b)}. \qquad (2.92)$$

In these equations, k is the projectile momentum, $q = 2k\sin(\vartheta/2)$ is the momentum transfer (assumed to be much smaller than k), ϑ is the scattering angle, $G_{\Pi LM}(v/c)$ are functions defined by Winther and Alder (1979), J_M is the Bessel function of order M and K_M is the modified Bessel function of order M. The eikonal phase is given by

$$\chi(b) = -\frac{1}{\hbar v}\int \mathrm{d}z U_{\mathrm{nuc}}(r) + \frac{2 Z_P Z_T e^2}{\hbar v}\ln(kb), \qquad (2.93)$$

where $r = (b, z)$ and U_{nuc} is the nuclear optical potential. The integral in equation (2.92) runs over the impact parameter b. The total number of virtual photons is obtained by an integral of equation (2.91) over scattering angles.

For the $E1$, $E2$ and $M1$ multipolarities, the functions $G_{\Pi LM}(v/c)$ are given by (Winther and Alder 1979)

$$\begin{aligned}
G_{E11}(x) &= -G_{E1-1}(x) = x\frac{\sqrt{8\pi}}{3},\\
G_{E10}(x) &= -4\mathrm{i}\frac{\sqrt{\pi\left(x^2-1\right)}}{3}\\
G_{M11}(x) &= G_{M1-1}(x) = -\mathrm{i}\frac{\sqrt{8\pi}}{3},\\
G_{M10}(x) &= 0\\
G_{E22}(x) &= G_{E2-2}(x) = -2x\frac{\sqrt{\pi\left(x^2-1\right)/6}}{5},\\
G_{E20}(x) &= 2x\frac{\sqrt{\pi\left(x^2-1\right)}}{5}\\
G_{E21}(x) &= -G_{E2-1}(x) = 2\mathrm{i}\sqrt{\frac{\pi}{6}}\frac{\left(2x^2-1\right)}{5}.
\end{aligned} \qquad (2.94)$$

In figure 3 we plot the virtual photon numbers for energy $E_\gamma \equiv E_x$ and $E1$ multipolarity, 'as seen' by a projectile passing by a lead target at impact parameters larger than $b = 12.3$ fm, corresponding to a 'safe' impact parameter above which the nuclear interaction becomes irrelevant. The figure displays the results for three typical bombarding energies. As the projectile energy increases, more virtual photons of large energy E_x are available for the reaction. This increases the number of states accessed in the excitation process.

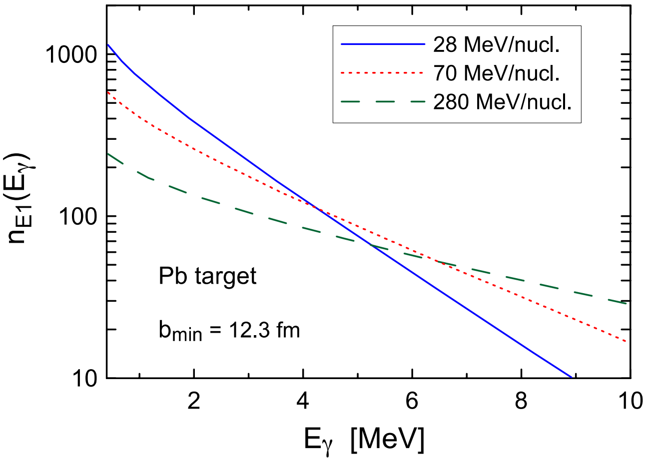

Figure 3. Total number of virtual photons for the E1 multipolarity, 'as seen' by a projectile passing by a lead target at impact parameters $b_{\min} = 12.3$ fm and larger, for three typical bombarding energies.

2.3.2. Coulomb dissociation. The CD method is based on the breakup of a projectile in the Coulomb field of a large Z target A. The (differential, or angle-integrated) Coulomb breakup cross section for $a + A \to b + c + A$ follows from equation (2.90). It can be rewritten as

$$\frac{d\sigma_{a+A\to b+c+A}}{d\Omega} = \frac{1}{E_x}\sum_{\Pi L}\frac{dn_{\gamma\Pi L}(E_x,\theta)}{d\Omega}\sigma^{\gamma\Pi L}_{\gamma+a\to b+c}(E_x), \tag{2.95}$$

where E_x is the energy transferred from the relative motion to the breakup, and $\sigma^{\gamma\Pi L}_{\gamma+a\to b+c}(E_x)$ is the photo-dissociation cross section for the multipolarity ΠL and photon energy E_x.

Time reversal, expressed in the form of the the detailed balance theorem, allows one to deduce the radiative capture cross section $b + c \to a + \gamma$ from the disintegration cross section, $\sigma^{\gamma\Pi L}_{\gamma+a\to b+c}(E_x)$,

$$\sigma^{\gamma\Pi L}_{b+c\to a+\gamma}(E_x) = \frac{2(2j_a+1)}{(2j_b+1)(2j_c+1)}\frac{q_x^2}{q^2}\sigma^{\gamma\Pi L}_{\gamma+a\to b+c}(E_x), \tag{2.96}$$

where $q^2 = 2m(E_x - S)/\hbar^2$, with S equal to the separation energy, and $q_x = E_x/\hbar c$.

The CD method was proposed by Baur *et al* (1986), and has been tested successfully in a number of reactions of interest to astrophysics. The most celebrated case is the reaction ^{7}Be(p, γ)^{8}B, first studied by Motobayashi *et al* (1994), followed by numerous experiments in the last two decades (see figure 4). Due to its importance for the solar neutrino problem (see Adelberger *et al* 2011) this reaction has been measured experimentally down to about 110 keV, with the Gamow peak being located around 20 keV. Extrapolations based on the experimental data to the Gamow window have been difficult and CD has been used as a complementary tool to help extrapolations to the low energies. It is worthwhile mentioning that, as already mentioned in section 2.3.3, and emphasized by Esbensen and Bertsch (1996), Bertulani (1996), Typel and Baur (2001), Esbensen *et al* (2005), Capel and Baye (2005), Bertulani (2005) and Goldstein *et al* (2007), higher order and relativistic effects and the contribution of higher multipoles have a significant influence on the reaction process, which makes it difficult to directly use equation (2.95). A more detailed analysis of the reaction process is necessary.

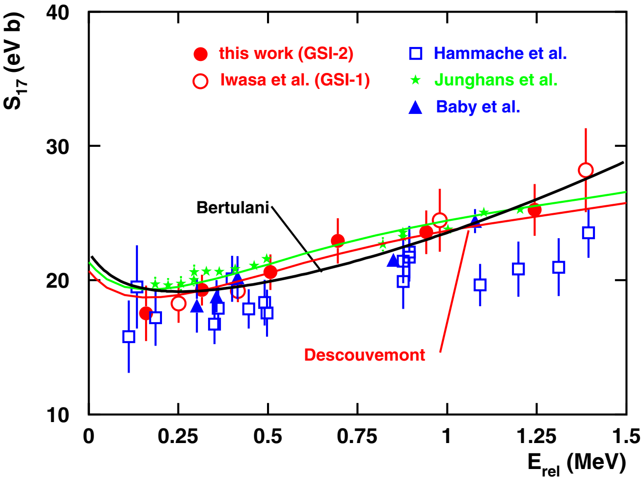

Figure 4. Selected data on ^{7}Be(p,γ)^{8}B compared to theoretical calculations. The filled circles show results obtained with the CD method (GSI-1&2). Data are from Hammache *et al* (1999), Junghans *et al* (2002), Baby *et al* (2003), Iwasa *et al* (1999), and this work;—Schümann *et al* (2003).

2.3.3. Final state interactions. Equation (2.95) is based on first-order perturbation theory. It also assumes that the nuclear contribution to the breakup is small, or that it can be separated under certain experimental conditions. The contribution of the nuclear breakup has been examined by several authors (see, e.g., Bertulani and Gai 1998). ^{8}B has a small proton separation energy ($S = 140$ keV). For such loosely bound systems it was shown by Bertulani and Canto (1992) that multiple step, or higher order effects are important. These effects occur due to multiple continuum–continuum transitions (see figure 5). Detailed studies of dynamic contributions to the breakup have been explored (Bertulani and Canto 1992, Baur *et al* 1992, Bertsch and Bertulani 1993, Bertulani 1994, 1995, 1996, Bertulani and Bertsch 1994, Esbensen *et al* 1995, Gai and Bertulani 1995, Bertulani and Gai 1998) and in several other later works. Three-body Coulomb interaction effects in the final state have been investigated by Alt *et al* (2005). The role of higher multipolarities, e.g., $E2$ contributions in the reaction ^{7}Be(p,γ)^{8}B and the coupling to high-lying states have also to be investigated carefully (Bertulani 1994, Gai and Bertulani 1995, Esbensen and Bertsch 1995, 1996, Bertulani and Gai 1998). It has been shown that the influence of giant resonance states on the dissociation channel is small (Bertulani 2002).

Bertulani and Canto (1992) were the first to notice that the CD of a weakly bound neutron-rich nucleus can lead to incursions in the continuum with continuum–continuum couplings becoming of large relevance. They developed a semiclassical continuum discretized coupled-channels (S-CDCC) method for the Coulomb breakup, with the assumption that the projectile wavefunction can be expanded on a discrete basis as $\Psi(\boldsymbol{r}, t) = \sum_k a_k(t)\Phi_k(\boldsymbol{r})$, where $a_k(t)$ are time-dependent expansion parameters, Φ_k are the basis

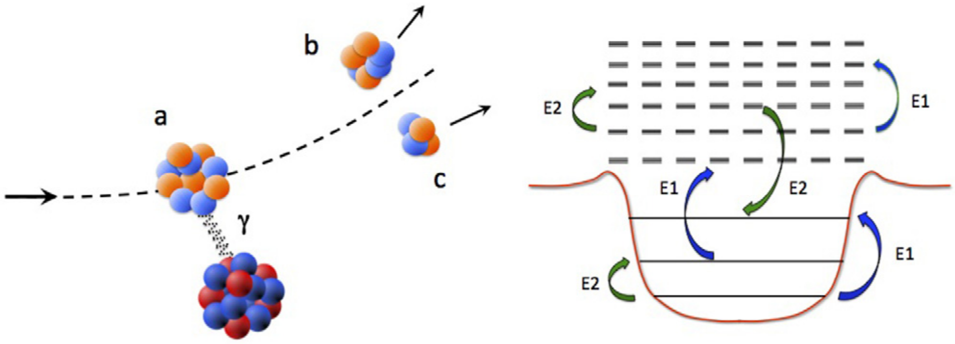

Figure 5. Schematic representation of (left) CD of projectile a into fragments b and c and (right) a multistep process involving $E1$ and $E2$ excitations, including continuum–continuum transitions.

functions and $\boldsymbol{r}$ is the relative coordinates of the fragments after the breakup. Besides the bound-state wavefunctions $\Phi_k^{(b)}$, the basis also includes continuum–discretized functions $\Phi_k^{(c)}$. The discretization is done by bunching the continuum solutions for the relative motion of the fragments around a continuum energy E_j so that

$$\Phi_k^{(c)} = \int_{E_j}^{E_j+\Delta} \Gamma_j(E)\,\psi_k^{(c)}(E)\,\mathrm{d}E, \tag{2.97}$$

where $\psi_k^{(c)}$ is the continuum solution for the relative motion of the fragments under the influence of a potential $U(\boldsymbol{r})$ and Δ is an energy window around the discretized energy E_j.

The orthogonal functions $\Gamma_j(E)$ are centered around E_j and are chosen conveniently to allow for a quick convergence of the matrix elements of continuum–continuum couplings (Bertulani and Canto 1992). For each impact parameter one then solves the coupled-channels equations

$$\frac{\mathrm{d}a_k}{\mathrm{d}t} = \frac{1}{\mathrm{i}\hbar}\sum_{j\Pi\mathrm{LM}} a_j(t)\left\langle\Phi_k|V_{\Pi LM}(t)|\Phi_j\right\rangle \exp\left[\frac{\mathrm{i}}{\hbar}\left(E_k - E_j\right)t\right], \tag{2.98}$$

where $V_{\Pi LM}$ is the time-dependent electromagnetic field generated by the target for multipolarity ΠLM. The observables such as momentum, energy and angular distributions of the fragments are obtained from the time-evolved wavefunction $\Psi(\boldsymbol{r}, t)$.

An analysis of the Coulomb breakup of ^{8}B to extract the astrophysical S-factor for the reaction ^{7}Be(p,γ)^{8}B was done by Bertulani (1996). The continuum–continuum couplings were indeed proven relevant for an accurate description of the breakup cross section.

The eikonal CDCC method (E-CDCC) developed by Ogata *et al* (2003, 2006) is an extension of the semiclassical CDCC that enables one to efficiently treat the nuclear and Coulomb breakup reactions at $E_{\mathrm{lab}} > 30$ MeV/nucleon. It is easy to see how the E-CDCC equations arise from equation (2.98) by the replacement $t \to z/v$, where z is the projectile coordinate (v is its velocity) along the beam axis and the replacement of the exponential by $S(b)\exp\left[\mathrm{i}\left(p_k - p_j\right)z/\hbar\right]$, where p_i is the projectile momentum in energy bin i and $S(b)$ is the eikonal scattering matrix. A proper relativistic treatment of the continuum–continuum couplings is necessary, as shown by Bertulani (2005) where the role of scalar and vector nuclear potentials has also been explored. This work has been further extended by Ogata and Bertulani (2009, 2010) and the effect of Lorentz transformations on the nuclear potentials was further accessed. The left panel of figure 6 shows the double differential breakup cross section of ^{8}B by ^{208}Pb at 250 MeV/nucleon. Here θ is the scattering angle of the center mass of the ^{7}Be and p, and ε is the breakup energy between the two fragments. In the right panel, the relative difference between the relativistic and non-relativistic results is shown. One sees significant increase of the cross section by several tens of percent. It should be noted that these dynamical relativistic effects are important not in the tail of the cross section but near the peak. Thus, the relativistic treatment of Coulomb interaction in continuum–continuum couplings is necessary to analyze Coulomb breakup processes in rare isotope beam facilities.

A proper relativistic treatment of nuclear potentials in breakup reactions at intermediate energies ($E_{\mathrm{lab}} > 30$ MeV/nucleon) requires the use of an effective meson-exchange theory combined with proper Lorentz transformations, as shown by Long and Bertulani (2011). This theory leads to appreciable deviations from the standard optical model method widely used in low-energy reactions. The Osaka group (Ogata *et al* 2011) has summarized the major theoretical results in CDCC calculations applied to nuclear astrophysics and to reaction with rare isotopes.

Another method to study higher order processes in CD was introduced by Bertsch and Bertulani (1993) and Bertulani and Bertsch (1994). In this method time and space are discretized and the Schrödinger initial wavefunction is propagated in time by the evolution equation

$$\Psi(\boldsymbol{r}, t) = \exp\left[-\mathrm{i}H(t - t_0)/\hbar\right]\Psi(\boldsymbol{r}, t_0), \tag{2.99}$$

where H is the total Hamiltonian for the system. This method is equivalent to CDCC. The method of choice to tackle the higher order effects depends on the convenience and accuracy of computational algorithms at hand. The simplest starting point to solve the Schrodinger equation using the time-evolution operator $\exp\left[-\mathrm{i}H(t - t_0)/\hbar\right]$ is to assume that the wavefunction can be expanded in a spherical basis: $\Psi(\boldsymbol{r}, t) =$

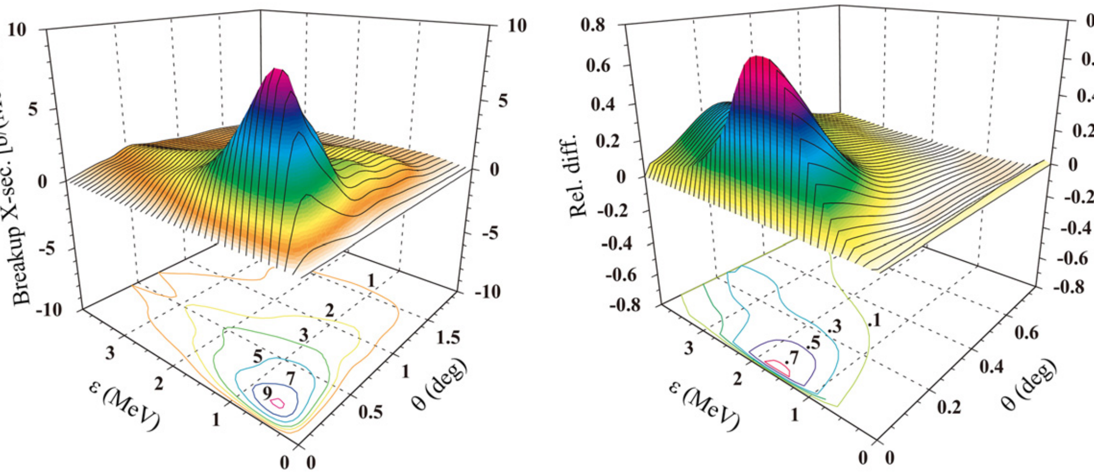

Figure 6. Double differential breakup cross section for ^{8}B+^{208}Pb at 250 MeV/nucleon including dynamical relativistic corrections (left panel) and its relative difference from the calculation without relativistic corrections (right panel).

$(1/r)\sum_{lm} u_{lm} Y_{lm}(\hat{r})$. Then the discretization is only needed for the radial coordinate with the equation to be solved for the radial wavefunction being of the form

$$\left[\frac{d^2}{dr^2} - \frac{l(l+1)}{r^2} - \frac{2\mu}{\hbar^2}U(r)\right] u_{lm}(r,t) + \sum_{\Pi LM l'm'} S_{\Pi LM}^{(lml'm')}(t)\, u_{l'm'}(r,t) = \frac{2i\mu}{\hbar}\frac{\partial u_{lm}}{\partial t}, \qquad (2.100)$$

where $U(r)$ is the interaction between the fragments and $S_{\Pi LM}^{(lml'm')}$ is a function of angular momentum algebraic coefficients and the Coulomb multipole potentials $V_{\Pi LM}(t)$ due to the interaction of the fragments with the target. The easiest way to solve this equation on the radial lattice is to use a three point derivative for the operator d^2/dr^2. The time evolution can be obtained by simple inversions of tri-diagonal matrices on the lattice at each time step (Bertsch and Bertulani 1993). The computation is limited by the number of points in the lattice and by the number of angular momenta lm needed for convergence.

With the appearance of faster computers, the lattice calculations have been extended to reach higher accuracy and more complex situations. A true discretization in three dimensions can also be done without need of expansion of the wavefunction in spherical coordinates. For more details on the different algorithms used in lattice calculations of the CD problem see Esbensen *et al* (1995), Kido *et al* (1996), Melezhik (1997), Capel *et al* (2003), Baye *et al* (2005) and Esbensen (2009). The Tsukuba group (Nakatsukasa *et al* 2008) has developed the most advanced lattice calculations for CD including absorbing boundary conditions (to simulate wave propagation outside the lattice) in order to study several reaction cases, extending the method to tackle problems in atomic and nuclear physics, including an extension to time-dependent density functional theory.

Coulomb excitation and CD experiments are now routinely a tool of choice to assess several nuclear properties and information of astrophysical interest in radioactive beam facilities. It is routinely used in laboratories worldwide and planned for future facilities, too (see, e.g., Reifarth 2013).

3. ANCs—experimental considerations

While the connection between the tail of the overlap function and low-energy direct capture had been recognized for some time, the use of a peripheral transfer reaction to measure an ANC was first suggested in 1994 by Xu *et al* (1994) as a way to determine the astrophysical S-factor, S_{17} from the ANC for $^8\mathrm{B} \rightarrow {}^7\mathrm{Be} + \mathrm{p}$, which is equivalent to the ^{7}Be(p,γ)^{8}B reaction rate at stellar energies since the cross section is completely dominated by direct capture at very low energy. When this was proposed, the uncertainty in S_{17} was one of the largest in the standard solar model prediction for the flux of multi-MeV neutrinos from the Sun. As preparations were being made to measure the ANC to determine S_{17}, a Workshop on Solar Fusion Reactions was held at the Institute for Nuclear Theory at the University of Washington. Reaction measurements with both direct and indirect techniques were discussed at length during the workshop. In a follow-up publication (Adelberger *et al* 1998), a test case was proposed in order to verify that an ANC obtained by a peripheral transfer would correctly predict a direct capture reaction rate. The case that was chosen was a determination of the S-factor for direct capture to the ground and first excited state of ^{17}F, which could be compared to direct data from the ^{16}O(p,γ)^{17}F reaction. Extensions of the ANC technique now include measurements of neutron ANCs to obtain proton ANCs for the mirror reaction and the extraction of ANCs from nuclear breakup reactions. Below we will discuss each of these topics starting with the test case.

3.1. ^{16}O(p,γ)^{17}F as a test case

In order to extract the ANCs for $^{17}\mathrm{F} \rightarrow {}^{16}\mathrm{O}+\mathrm{p}$, a measurement of the transfer reaction ^{16}O(^{3}He,d)^{17}F was carried out at a ^{3}He beam energy of 29.75 MeV where the reaction would be highly peripheral. Combining this with a previous measurement that had been carried out at a beam energy of 25 MeV (Vernotte *et al* 1994), allowed for a more reliable extraction of the ANCs. Data at laboratory scattering angles between 6.5° and 25° were obtained using Si solid-state detector telescopes and a ^{3}He beam from the U-120M isochronous cyclotron of the Nuclear Physics Institute (NPI) of the Czech Academy of Sciences, while data at laboratory angles between 1° and 11° were obtained using the MDM magnetic spectrometer and a molecular ^{3}He-d beam from the Texas A&M University K500 superconducting cyclotron. Both experiments used conventional nuclear physics techniques for measuring transfer reaction angular distributions. More details of the experiments can be found in Gagliardi *et al* (1999).

The ANCs were extracted from the angular distributions by comparison to DWBA calculations according to equation (2.55). The calculations were carried out with the finite-range code PTOLEMY (Rho des-Brown *et al* 1980) using the full transition operator. The single-particle orbitals were calculated in Woods–Saxon potentials with a radius parameter, r_0, in the range 1.15–1.35 fm and a diffusivity parameter, a_0, in the range 0.55–0.75 fm. The results indicated that the DWBA cross section divided by the square of the single-particle ANCs is insensitive to parameters of the Woods–Saxon potential. Indeed, this is a key signature of a peripheral transfer reaction. A range of optical model parameter sets were studied for both the entrance and exit channels, as detailed in Gagliardi *et al* (1999), and the resulting fits to the ground and excited state angular distributions are shown in figure 7. Normalizing the DWBA calculations to the data and dividing by the squares of the ANCs for the single-particle orbitals yields the product of the ANC's for the $^{17}\mathrm{F} \rightarrow {}^{16}\mathrm{O}+\mathrm{p}$ and $^3\mathrm{He} \rightarrow \mathrm{d}+\mathrm{p}$. Dividing this product by the known ANC for $^3\mathrm{He} \rightarrow \mathrm{d}+\mathrm{p}$ (Kamimura and Kameyama 1990, Mukhamedzhanov *et al* 1995) yields C^2 for $^{17}\mathrm{F} \rightarrow {}^{16}\mathrm{O}+\mathrm{p}$. The final adopted squares of the ANCs are $1.08 \pm 0.01\,\mathrm{fm}^{-1}$ for the ground state and $6490 \pm 680\,\mathrm{fm}^{-1}$ for the first excited state. The uncertainty for the ground state ANC includes ±4.8% from the absolute normalization and angle accuracies, plus the statistics of the fits, and ±7.6% associated with the choice of optical model parameters and single-particle orbital. The corresponding contributions to its uncertainty are ±5.4% and ±9.0%.

The relation of the ANCs to the direct capture rate at low energies was discussed in section 2.1.1. Since there is no resonant capture contribution at low energy for this system, the S-factors describing the capture to both the ground and first excited states are straightforward to calculate and require no additional normalization constants. The results are shown in figure 8 compared to the two previous measurements of $^{16}\mathrm{O}(\mathrm{p},\gamma)^{17}\mathrm{F}$ (Morlock *et al* 1997, Chow *et al* 1975). Both $E1$ and $E2$ contributions have been included in the calculations, but the $E1$ components dominate the results. The theoretical uncertainty in the S-factors is less than 2% for energies below 1 MeV. The agreement between the measured S-factors and those calculated from our measured ANCs is quite good, especially for energies below 1 MeV where the approximation of ignoring contributions from the nuclear interior should be very reliable. Due to a very small yield at low energies, the measured S-factor for the ground state may have background contamination that causes it to deviate from the predicted shape below about 0.5 MeV as discussed in Gagliardi *et al* (1999).

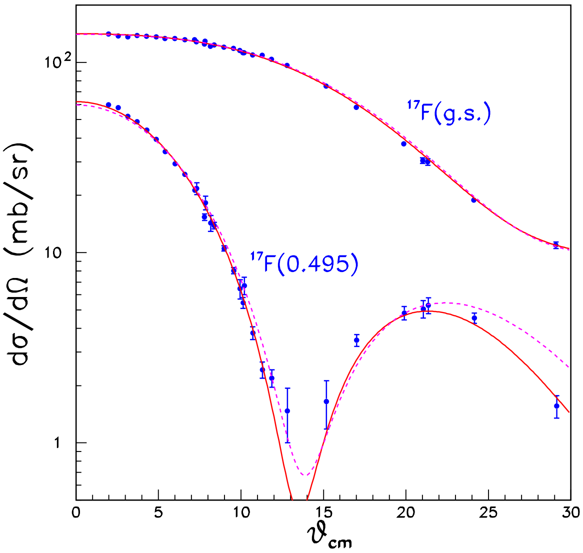

Figure 7. Angular distributions from the $^{16}\mathrm{O}(^3\mathrm{He,d})^{17}\mathrm{F}$ reaction with DWBA fits. The extracted ANCs were used to calculate the direct capture astrophysical S-factor.

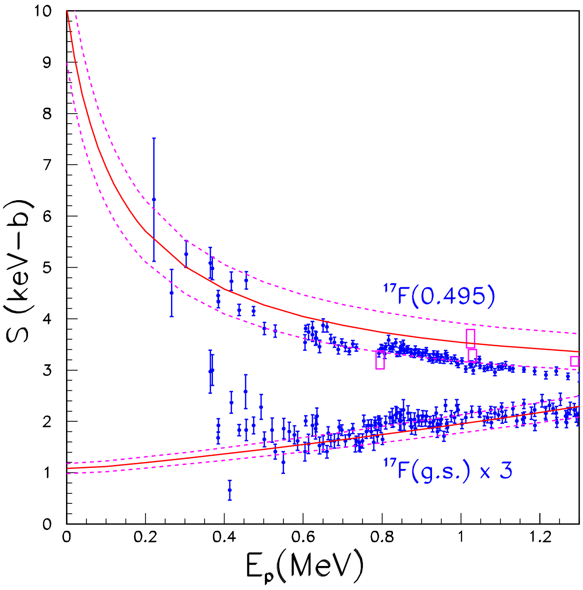

Figure 8. The direct capture astrophysical S-factor for $^{16}\mathrm{O}(\mathrm{p},\gamma)^{17}\mathrm{F}$ calculated from the ANCs and compared to experimental data. The dashed lines are based on the 1σ uncertainties of the ANCs. See text for data sources.

3.2. ANCs from peripheral transfer reactions—additional tests

In order to verify the ANC technique, two issues needed to be addressed: (1) the extraction of the ANC for a system should be independent of the transfer reaction used to measure it; (2) ANCs correctly predict direct capture cross sections. The second issue was verified for the test case as discussed above. In order to understand the first issue, proton ANCs for $^{14}\mathrm{N} \rightarrow {}^{13}\mathrm{C}+\mathrm{p}$ and neutron ANCs for $^{13}\mathrm{C} \rightarrow {}^{12}\mathrm{C}+\mathrm{n}$ were extracted from different reactions.

With a ^{3}He beam of about 8 MeV/nucleon from the U120 cyclotron at the NPI, angular distributions, normalized to absolute cross sections, were measured for the $^{13}\mathrm{C}(^3\mathrm{He,d})^{14}\mathrm{N}$

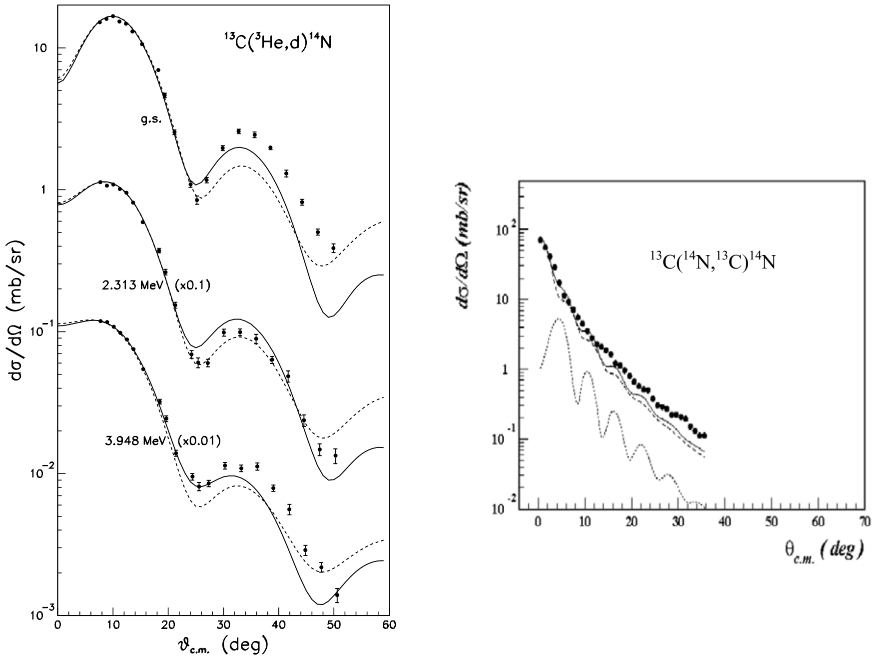

Figure 9. The left panel gives angular distributions and DWBA fits for the ^{13}C(^{3}He,d)^{14}N reaction. The right panel shows the proton-exchange reaction, ^{13}C(^{14}N,^{13}C)^{14}N angular distribution to the ground state of ^{13}C. The ANCs determined from these different reactions are compared in table 1.

reaction (Bem *et al* 2000). The reaction products were observed in silicon solid-state particle detectors using a setup that was optimized for determining absolute reaction cross sections. Transitions to the ground and excited states were measured. The ANCs for the stronger transitions were extracted by comparison to DWBA calculations, carried out with the code DWUCK5 (Kunz unpublished), properly normalized with single-particle ANCs. Elastic scattering data also was obtained to constrain optical model parameters. Results for the transition to the ground and excited states of ^{14}N are shown in the left panel of figure 9 along with the DWBA predictions. In these comparisons, the important region is at very forward angles where the extraction of the ANC is most reliable.

The same ANCs were measured using a heavy-ion beam through the ^{13}C(^{14}N,^{13}C)^{14}N (Trache *et al* 1998) one-proton-exchange reactions using an ^{14}N beam at about 10 MeV/nucleon from the TAMU K500 superconducting cyclotron. For the heavy-ion induced reaction, the outgoing reaction products were observed at the focal plane of the MDM magnetic spectrometer with the Oxford detector (Pringle *et al* 1986). The detector provided four consecutive position determinations along the dispersive direction for particles as they traversed the ion chamber, which contained pure isobutane gas. The position determinations were done by measuring the charge on each end of resistive wires that were separated consecutively through the counter depth by about 16 cm. A plastic scintillator at the end of the gas volume was used to measure a residual energy. Particles were then identified from the signals corresponding to ΔE_{gas} and E_{plastic}. By combining the four position readouts, the particle trajectory was reconstructed and then ray tracing was used to determine the scattering angle on a particle by particle basis. An advantage of the proton-exchange reaction for determining ANCs is that the ground state to ground state transition has the same ANC in the entrance and exit channels. Thus the cross section for the transition is proportional to C^4. Furthermore, the optical model parameters used in the DWBA calculation are identical for the entrance and exit channels. The optical model analysis for these reactions was carried out using the code PTOLEMY (Rho des-Brown *et al* 1980). The results for the angular distributions for the ground state to ground state transition for ^{13}C(^{14}N,^{13}C)^{14}N is compared to the DWBA fit in the right panel of figure 9. The results for the ANCs obtained in the different reactions are given in table 1. Note that the agreement between them is excellent.

The neutron ANC for ^{13}C → ^{12}C + n has been determined from light-ion stripping reactions and from a heavy-ion transfer reaction. The results for the ANC from stripping reactions were summarized by Mukhamedzhanov and Timofeyuk (1990) and the value for the ANC is given in table 1. The ANC was also determined from the transfer reaction ^{13}C(^{12}C,^{13}C)^{12}C using a ^{12}C beam from the TAMU K500 cyclotron at around 10 MeV/nucleon. The technique used to measure the transfer reaction was very similar to that used for the proton ANCs. The results from the measurement are given in table 1. The agreement between the light- and heavy-ion reactions is once again quite good.

3.3. Proton ANCs from transfer reactions with stable beams and targets

Following techniques similar to those described in sections 3.1 and 3.2, additional proton ANCs have been measured for p and s–d shell nuclei using (^{3}He,d) and heavy-ion reactions on stable targets at beam energies around 8 MeV/nucleon. The additional reactions that have been studied at the NPI in Rez include ^{14}N(^{3}He,d)^{15}O (Mukhamedzhanov *et*

Table 1. Results from two different reactions measuring the same ANCs for ground state to ground state transitions. Note that the quantum numbers and other labels have been dropped here for simplicity.

Reaction (ANC)	C^2 (fm^{-1})	Reference
^{13}C(^{3}He,d)^{14}N; (^{14}N → ^{13}C + p)	18.7 ± 1.3	Bem *et al* (2000)
^{13}C(^{14}N,^{13}C)^{14}N; (^{14}N → ^{13}C + p)	19.5 ± 1.2	Trache *et al* (1998)
Average for ^{13}C → ^{12}C + n from light-ion reactions	2.40 ± 0.12	Gubler *et al* (1977); Mukhamedzhanov and Timofeyuk (1990)
^{13}C(^{12}C,^{13}C)^{12}C; (^{13}C → ^{12}C + n)	2.24 ± 0.11	Al-Abdullah *et al* (2010)

Table 2. Other proton ANC measurements of ground states with stable beams and targets. Note that the quantum numbers and other labels have been dropped here for simplicity.

Reaction (ANC)	C^2 (fm^{-1})	Reference
^{9}Be(^{10}B,^{9}Be)^{10}B; (^{9}Be + p → ^{10}B)	5.06 ± 0.46	Mukhamedzhanov *et al* (1997)
^{14}N(^{3}He,d)^{15}O; (^{14}N + p → ^{15}O)	54.0 ± 5.4	Mukhamedzhanov *et al* (2003a)
^{15}N(^{3}He,d)^{16}O; (^{15}N + p → ^{16}O)	192.0 ± 26.0	Mukhamedzhanov *et al* (2008a, 2008b)
^{20}Ne(^{3}He,d)^{21}Na; (^{20}Ne + p → ^{21}Na)	0.21 ± 0.04	Mukhamedzhanov *et al* (2006)

al 2003a), ^{15}N(^{3}He,d)^{16}O (Mukhamedzhanov *et al* 2008a, 2008b), ^{17}O(^{3}He,d)^{18}F (Burjan 2013), ^{18}O(^{3}He,d)^{19}F (Burjan 2013), and ^{20}Ne(^{3}He,d)^{21}Na (Mukhamedzhanov *et al* 2006). The ANCs have been used to fix the (p,γ) direct capture rate for ground and excited state transitions and to determine the proton capture rate through sub-threshold states in ^{15}O and ^{21}Na. The measurements at the NPI have been carried out with ^{3}He beams of about 8 MeV/nucleon. A special gas cell was built to carry out the experiments with ^{15}N, $^{17-18}$O and ^{20}Ne. The gas cell temperature and pressure were monitored continuously throughout the experiments in order to be able to obtain absolute cross sections for the reactions. The results of the measurements that have been published are summarized in table 2. Below we provide the astrophysical motivation for two of these measurements.

The ANCs for ^{14}N + p → ^{15}O were measured to better determine the low-energy S-factor for the ^{14}N(p,γ)^{15}O reaction. This is the slowest reaction in the CNO cycle (Rolfs and Rodney 1988) and thus it determines the amount of energy produced in the cycle as well as the rate of hydrogen burning by CNO material. Prior to this work, one direct measurement of the reaction rate had been carried out to energies slightly below the lowest resonance (Schroeder *et al* 1987). The primary contribution to the S-factor at stellar energies comes from the sub-threshold state in ^{15}O at 6.79 MeV. The direct data from Schroeder *et al* (1987) had to be extrapolated to small energies and thus was very sensitive to the parameters that were used for this state. Around the same time that the measurement of the ^{14}N(^{3}He,d)^{15}O reaction occurred, an attempt was made to determine the gamma width of this state. The results (Bertone *et al* 2001) showed that the gamma width was much smaller than the value that had been found in the previous fit to the direct data in Schroeder *et al* (1987). The ANC for the sub-threshold state determined the overall normalization of the direct capture through the state and its proton width. With this information, an R-matrix fit was carried out to determine the S-factor. The result was nearly a factor of 2 smaller than the value obtained from extrapolating the direct data to low energy. The discrepancy in rates led to new direct measurements. Definitive results were obtained by the LUNA collaboration (see Marta *et al* (2008) for the most recent results) using the underground facility at the Gran Sasso laboratory, where background in the gamma-detector array is much reduced over that in terrestrial laboratories. The new data, which extended to much lower proton energy than the previous direct measurements, agreed very well with the ANC result. As an indication of the importance of this new value, it increased the age estimate for globular clusters by 10^9 years.

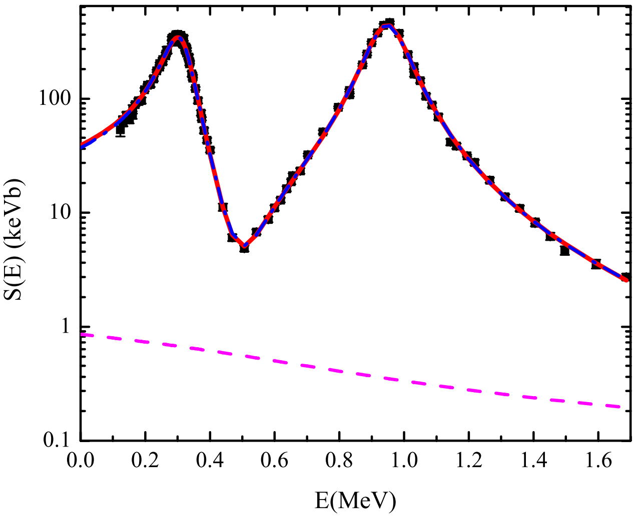

Figure 10. The astrophysical S-factor for the ^{15}N(p,γ)^{16}O reaction. The black squares are experimental data from Le Blanc *et al* (2010). The solid red line is an unconstrained R-matrix fit that includes interfering amplitudes from resonances, a non-resonant term and a background term. See Mukhamedzhanov *et al* (2011) for details.

The ANCs for ^{16}O → ^{15}N + p constrain the direct capture contribution to the ^{15}N(p,γ)^{16}O reaction, which provides a path for producing ^{16}O in the stellar hydrogen burning CN cycle. The ANCs were measured in an experiment with the ^{15}N(^{3}He,d)^{16}O reaction (Mukhamedzhanov *et al* 2008a, 2008b) and the results are given in table 2. A recent R-matrix calculation for the ^{15}N(p,γ)^{16}O reaction was carried out and is detailed in Mukhamedzhanov *et al* (2011). The S-factor obtained from the calculation is plotted in figure 10. The result fits the recent data obtained from the LUNA

Table 3. Proton ANCs from RIB measurements. Note that the quantum numbers and other labels have been dropped here for simplicity.

Reaction and ANC system	C^2 (fm^{-1})	Reference
d(^{7}Be,^{8}B)n; ^{8}B → ^{7}Be + p	0.60 ± 0.17	Liu *et al* (1996); Gagliardi *et al* (1998)
^{10}B(^{7}Be,^{8}B)^{9}Be; ^{8}B → ^{7}Be + p	0.460 ± 0.046	Azhari *et al* (2001)
^{14}N(^{7}Be,^{8}B)^{13}C; ^{8}B → ^{7}Be + p	0.466 ± 0.049	Tabacaru *et al* (2006)
^{14}N(^{11}C,^{12}N)^{13}C; ^{12}N → ^{11}C + p	1.73 ± 0.25	Tang *et al* (2003)
^{14}N(^{12}N,^{13}O)^{13}C; ^{13}O → ^{12}N + p	2.53 ± 0.30	Banu *et al* (2009)
^{14}N(^{13}N,^{14}O)^{13}C; ^{14}O → ^{13}N + p	29.0 ± 4.3	Tang *et al* (2004)

collaboration using the ANC found in Mukhamedzhanov *et al* (2008a, 2008b).

The ^{21}Na → ^{20}Ne + p ANCs provide the direct capture contribution to the ^{20}Ne(p,γ)^{21}Na reaction and in particular they help determine the contribution from the sub-threshold state that dominates the rate at stellar energies. This reaction is the first one in the Ne–Na cycle, which leads to the production of ^{21}Na, ^{21}Ne, ^{22}Na, ^{22}Ne and ^{23}Na. One of the important products out of this cycle is ^{21}Ne, which can then generate neutrons via the ^{21}Ne(α,n)^{24}Mg reaction. The ANC results were used to calculate the S-factor for the reaction. Capture through the sub-threshold state depends on both the ANC and the gamma width of the state. Using data from direct measurements and the ANC provide the information needed to predict the gamma width. The result found from this approach was in good agreement with the direct measurement of the width as described in Mukhamedzhanov *et al* (2006).

3.4. Proton ANCs from transfer reactions with radioactive beams

A major advantage of the ANC technique, and one of the primary motivations for developing it, is that it can be used effectively to obtain information about proton direct capture on radioactive nuclei. The measurements that have been done to date with radioactive beams are summarized in table 3.

The first ANC measurements for radioactive systems were for ^{8}B → ^{7}Be + p. The ANC for this reaction fixes the direct capture rate at low energy for the ^{7}Be(p,γ)^{8}B reaction. The decay of ^{8}B is the primary source for high-energy solar neutrinos so determining the rate of the reaction is important for pinning down the solar neutrino flux observed in large underground detectors such as Super-Kamiokande and the Sudbury Neutrino Observatory (SNO). The first of these measurements was reported by the group at the China Institute for Atomic Energy in Beijing who carried out a d(^{7}Be,n)^{8}B reaction with a secondary beam of ^{7}Be at 26 MeV that was produced by the ^{7}Li(p,n)^{7}Be reaction using their Tandem Van de Graff accelerator (Liu *et al* 1996) to produce a 34 MeV ^{7}Li beam. The secondary beam was separated from the primary beam by its difference in magnetic rigidity. The reaction was studied by measuring the reaction products produced in a deuterated polyethylene target. One problem that quickly surfaced with the analysis of this data was the lack of neutron optical model parameters at energies appropriate for the outgoing channel. This led to large uncertainties in the extracted ANC (Gagliardi *et al* 1998). Soon after this measurement was published, the first results for this ANC from a heavy-ion transfer reaction were published based upon the ^{10}B(^{7}Be,^{8}B)^{9}Be reaction (Azhari *et al* 1999a). The 10 MeV/nucleon ^{7}Be beam for this experiment was produced again by the ^{7}Li(p,n)^{7}Be reaction using a gas cell at 2 atm of H_2 gas that was cooled to LN_2 temperature and a primary beam from the TAMU K500 cyclotron. The reaction products were separated by the MARS recoil spectrometer (Tribble *et al* 1991) at TAMU and resulted in a ^{7}Be beam that was >99% pure. A silicon detector telescope was used to measure the outgoing ^{8}B particles. Several improvements were made to the detection system and the primary beam intensity for a second measurement of this ANC via the ^{14}N(^{7}Be,^{8}B)^{13}C reaction (Azhari *et al* 1999b) where a melamine target was used for ^{14}N. The flux of ^{7}Be that provided the normalization for the two reactions was obtained by measuring the production rate at low beam intensity and then assuming a linear extrapolation to higher intensity. The primary beam current was then measured to obtain the rate. In later experiments with a different detector geometry, we found that this extrapolation procedure was not valid for the higher intensity primary beam that was used for the ^{14}N(^{7}Be,^{8}B)^{13}C reaction. A follow-up measurement was carried out with a new detector geometry that provided a direct measurement of the secondary beam particles. The results from that measurement represent the final ANCs that were obtained from proton transfer for this reaction and yield an astrophysical S-factor of $S(0) = 18.6 \pm 1.8$ eV-b for ^{7}Be(p,γ)^{8}B (Tabacaru *et al* 2006), which is a bit lower than the recommended value of 20.8 ± 0.7 (expt) ± 1.4 (theor) eV-b from the second solar fusion workshop (Adelberger *et al* 2011). The angular distribution for the transfer reaction from Azhari *et al* (1999b) is shown in figure 11 along with the DWBA calculation that was used to extract the ANC.

Transfer reactions with ^{11}C (Tang *et al* 2003), and $^{12-13}$N radioactive beams (Banu *et al* 2009, Tang *et al* 2004) have been used to study other (p,γ) reactions on radioactive nuclei that have a significant direct capture contribution. A melamine target was used in these studies as well since the ^{14}N → ^{13}C+p ANC is well known. The general techniques that were used for the studies are similar those for the ^{7}Be reaction studies. Angular distributions for the transfer reactions (^{11}C,^{12}N) and (^{13}N,^{14}O) along with DWBA predictions, and resulting S-factors for the reactions are shown in figures 12 and 13. The results for the ANCs between the ground states of the initial and final nuclei are given in table 3.

The ANC for ^{12}N → ^{11}C + p fixes the rate for the ^{11}C(p,γ)^{12}N reaction. This is one of the reactions in the rapid alpha-proton chain that can bypass the 3α reaction to

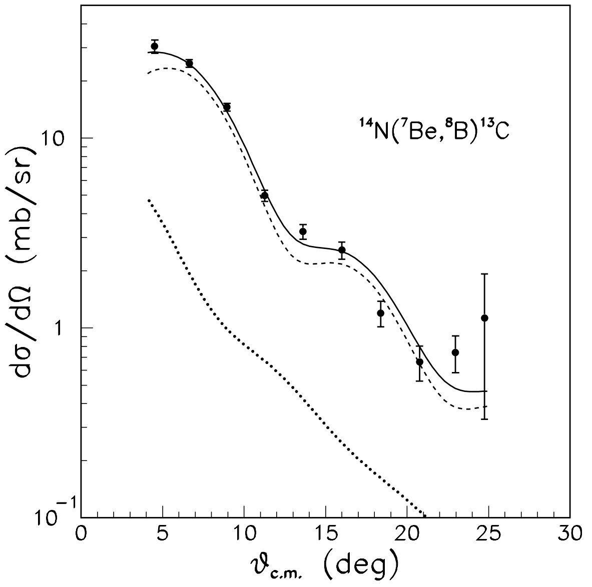

Figure 11. The angular distribution from the ^{14}N(^{7}Be,^{8}B)^{13}C reaction and the DWBA prediction. The ANC from the measurement was used to determine the astrophysical S-factor, $S_{17}(0)$.

produce ^{12}C in a star (Wiescher *et al* 1989). The carbon is needed to provide fuel for the CNO cycle, which generates significantly more heat than the p–p reaction chain and can help stabilize very metal poor giant stars from rapid collapse. The S-factor at energies important for this process is primarily due to direct capture. The ANC for $^{13}\mathrm{N} + \mathrm{p} \rightarrow {}^{14}\mathrm{O}$ gives the direct capture contribution to the ^{13}N(p,γ)^{14}O reaction, which signals the onset of the (β-limited) hot-CNO reaction cycle. Direct capture interferes with resonant capture in this reaction and substantially modifies the low-energy S-factor for the reaction. The difference between destructive and constructive interference is a factor of 4 based on the ANC found in Tang *et al* (2004). The increase for constructive interference, which is expected, relative to the resonant contribution is more than a factor of 2 at stellar energies as is shown in figure 13 (Tang *et al* 2004). The $^{13}\mathrm{O} \rightarrow {}^{12}\mathrm{N} + \mathrm{p}$ ANC fixes the direct capture rate for the ^{12}N(p,γ)^{13}O reaction, which is a termination reaction in the rapid alpha-proton chain.

3.5. Proton ANCs determined from neutron ANCs in mirror symmetric reactions

Heavy-ion reactions involving neutron transfer at energies around 10 MeV/nucleon are highly peripheral and they provide an optimum way for determining neutron ANCs. Neutron ANCs are useful for understanding the direct capture part of (n,γ) reactions if an angular momentum barrier exists. They are not useful for s-wave capture. However, neutron ANCs can be used to infer proton ANCs through charge symmetry (see Mukhamedzhanov *et al* (2012), and references therein). Up to charge symmetry breaking effects, the connection between mirror symmetric proton and neutron ANCs is made through the relationship between the ANC and the SF. By mirror symmetry, the SFs for the proton and neutron systems are the same. Then to relate the mirror nucleon ANCs we can use equation (2.48).

The charge symmetry relationship has been used to determine proton ANCs for several important reactions. The first measurement that was carried out was the ^{13}C(^{7}Li,^{8}Li)^{12}C reaction with a ^{7}Li beam at 9 MeV/nucleon (Trache *et al* 2003). The angular distribution obtained for this reaction is shown in figure 14. The ^{13}C target was chosen for this reaction since the $^{13}\mathrm{C} \rightarrow {}^{12}\mathrm{C} + \mathrm{n}$ ANC is well known as shown in table 1. Invoking mirror symmetry, the proton ANCs that were determined were for $^8\mathrm{B} \rightarrow {}^7\mathrm{Be} + \mathrm{p}$. Since the beam and target are both stable isotopes, the measurement was carried out in the MDM magnetic spectrometer at TAMU. This has several advantages over the radioactive beam experiments. The stable beam intensity is much higher than that for the radioactive beam so measurements can be made over a much larger angular range. Also by using the MDM spectrometer, measurements at very small center-of-mass angles can be made. This is particularly important for separating the different angular momentum components that contribute to the cross section. As can be seen in figure 14, the contribution from the $\mathrm{p}_{1/2}$ and $\mathrm{p}_{3/2}$ orbitals can be separated in the reaction with the very forward angle data. The proton ANCs that were obtained from the neutron transfer reaction are given in table 4. The agreement is very good with the ANCs that were obtained using the ^{7}Be beam on the melamine target.

Other proton ANCs that have been determined by this technique include $^{18}\mathrm{Ne} \rightarrow {}^{17}\mathrm{F} + \mathrm{p}$ from $^{18}\mathrm{O} \rightarrow {}^{17}\mathrm{O} + \mathrm{n}$ ANCs (Al-Abdullah *et al* 2014), $^{23}\mathrm{Al} \rightarrow {}^{22}\mathrm{Mg} + \mathrm{p}$ from $^{23}\mathrm{Ne} \rightarrow {}^{22}\mathrm{Ne} + \mathrm{n}$ (Al-Abdullah *et al* 2010), and $^{27}\mathrm{P} \rightarrow {}^{26}\mathrm{Si} + \mathrm{p}$ from $^{27}\mathrm{Mg} \rightarrow {}^{26}\mathrm{Mg{+}n}$ (McCleskey 2013). The measurements were carried out with stable beams of ^{17}O, ^{22}Ne and ^{26}Mg at about 10 MeV/nucleon from the K500 superconducting cyclotron on ^{13}C targets using the MDM spectrometer to measure elastic scattering and transfer reaction products. The results for ground state to ground state transitions from the reactions that have been published are summarized in table 4. Note that the large number for the proton ANC in $^{23}\mathrm{Al} \rightarrow {}^{22}\mathrm{Mg} + \mathrm{p}$ is due to the very low binding energy of the proton in ^{22}Mg.

3.6. ANCs from single nucleon removal reactions

A process that is similar to CD involves the removal of a loosely bound single nucleon from a heavy-ion projectile at energies of about a hundred MeV/nucleon or more that interacts with a low-Z target. Since the core nucleus must survive following the nucleon removal, this process is highly peripheral and consequently its cross section depends on the ANC for the system. The first application of this approach involved determining the ANC for $^9\mathrm{C} \rightarrow {}^8\mathrm{B} + \mathrm{p}$ from data for ^{9}C breakup in Trache *et al* (2002). The underlying analysis process is similar to what is done to extract ANCs from transfer reactions. The cross section for the one-nucleon removal depends on the reaction dynamics and the ANC. In the case of nucleon removal, the dynamics has been calculated using an extended Glauber model approach as discussed in Trache *et al* (2002).

The details of the calculations for ^{9}C breakup on four targets, carbon, aluminum, tin and lead, can be found in Trache

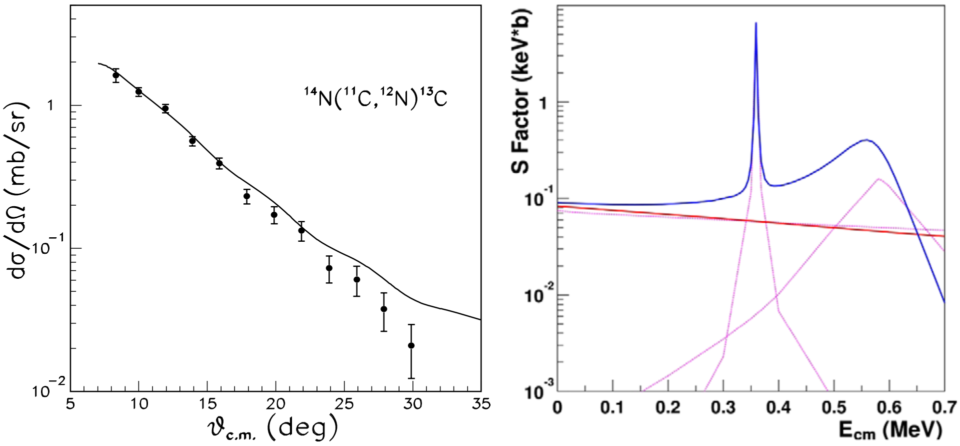

Figure 12. The left panel gives the angular distribution for the ^{14}N(^{11}C,^{12}N)^{13}C reaction along with the DWBA prediction and the right panel shows the resulting S-factor calculation. The direct capture contribution is shown as the solid red line, which dominates at low energy. The magenta solid lines are the contributions of the first and second resonances. The blue solid line is the total S-factor contributed by the interfering resonant and direct capture terms.

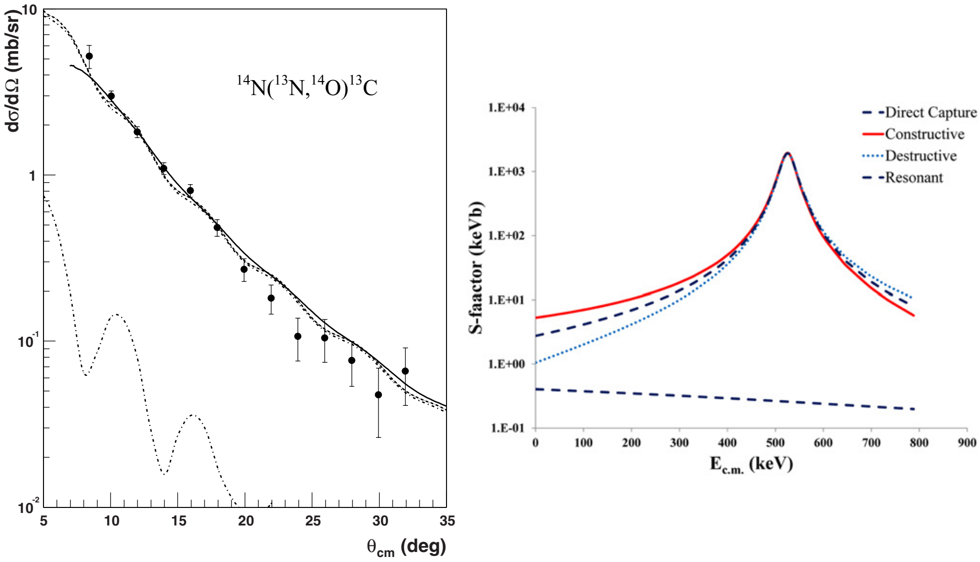

Figure 13. The angular distribution for the ^{14}N(^{13}N,^{14}O)^{13}C reaction and the DWBA fit. The right panel gives the S-factor for ^{13}N(p,γ)^{14}O. The contributions from resonant and direct capture are shown as dashed blue lines. The S-factor assuming destructive interference is shown as the dotted blue line and the solid red line shows the result for constructive interference, which is preferred by theory.

et al (2002). The ANC for the ^{9}C → ^{8}B + p system was determined by comparing the calculations for each target to the measured cross section. For the case of ^{9}C, two different configurations contribute to the breakup, $p_{3/2}$ and $p_{1/2}$. The authors of Trache *et al* (2002) noted that since the removal cross section is dominated by peripheral interactions, the dynamical cross section for the two configurations and the asymptotic form of the single-particle ANCs would be the same. Then the sum of the squares of the ANCs for the two configurations could be obtained from the data by the relation $\sigma_{-1p} = ((C^{^9\mathrm{C}}_{p^8B\,1\,3/2\,3/2})^2 + (C^{^9\mathrm{C}}_{p^8B\,1\,1/2\,3/2})^2)\sigma_{\mathrm{sp}}/b^2_{1\,1\,3/2\,3/2}$, where σ_{-1p} is the measured cross section, σ_{sp} is the calculated single-particle removal cross section for particle p_j and $b_{1\,1\,3/2\,3/2}$ is the ANC for the particle removed from the core. The same form for the combined ANCs appears in the astrophysical S-factor for ^{8}B(p,γ)^{9}C.

Following the initial work on ^{9}C breakup, the ANCs for ^{8}B → ^{7}Be + p (Trache *et al* 2004) and ^{24}Si → ^{23}Al + p (Banu *et al* 2012) have been determined from the breakup of ^{8}B and ^{24}Si, respectively. With the availability of exotic beams from rare isotope facilities, more ANC measurements will be done by this approach. Because of this, more effort is now being put into the theoretical approach for calculating the single-particle removal cross sections.

3.7. ANCs and radiative widths in an R-matrix analysis for radiative capture

The R-matrix formalism provides a consistent way to analyze radiative capture reactions, such as $x + A \rightarrow F + \gamma$. The R-matrix radiative capture cross section to a state of nucleus

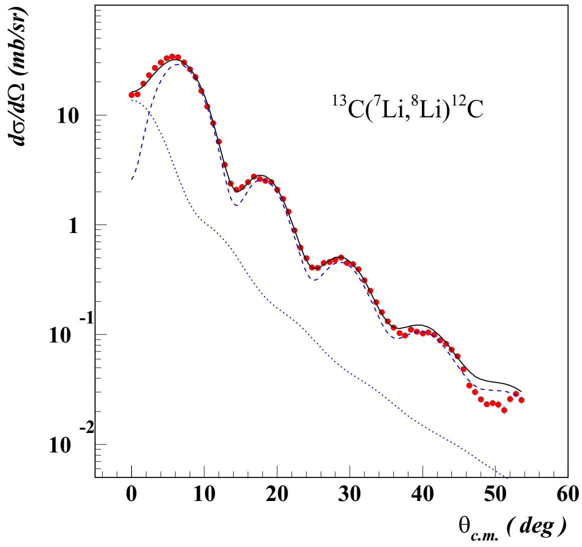

Figure 14. Angular distribution for the ^{13}C(^{7}Li,^{8}Li)^{12}C reaction along with the DWBA prediction. The dotted line corresponds to the $p_{1/2} \to p_{1/2}$ contribution and the dashed line is the $p_{1/2} \to p_{3/2}$ contribution. The extracted neutron ANC is given in table 4 along with the proton ANC that was determined using charge symmetry.

F with a given spin J_f is given by Barker and Kajino (1991) as

$$\sigma_{J_f}(E_{xA}) = \frac{\pi}{k_{xA}^2} \sum_{J_i l_i I} \frac{\hat{J}_i}{\hat{J}_x \hat{J}_A} |U_{l_f l_i I J_f J_i}(E_{xA})|^2. \tag{3.1}$$

Here, $\hat{J} = 2J + 1$, J_i is the total angular momentum of the colliding nuclei x and A in the initial state J_x and J_A are their spins, I and l_i are their channel spin and orbital angular momentum, and k_{xA} is the relative $x - A$ momentum related to their relative kinetic energy E_{xA} as $k_{xA} = \sqrt{2\mu_{xA} E_{xA}}$, with μ_{xA} the reduced mass of x and A. Note that in this section we use the LS-coupling scheme rather than jj-coupling used in the previous sections. Here we once again use the system of units in which $\hbar = c = 1$. In (3.1) $U_{l_f l_i I J_f J_i}(E_{xA})$ is the transition amplitude from the initial continuum state (l_i, I, J_i) to the final bound state (l_f, I, J_f). It is given by the sum of the resonant $U^{\rm R}_{I l_f l_i J_f J_i}(E_{xA})$ and non-resonant $U^{\rm NR}_{I l_f l_i J_f J_i}(E_{xA})$ transition amplitudes:

$$U_{I l_f l_i J_f J_i}(E_{xA}) = U^{\rm R}_{I l_f l_i J_f J_i}(E_{xA}) + U^{\rm NR}_{I l_f l_i J_f J_i}(E_{xA}). \tag{3.2}$$

The resonant amplitude itself can have contributions from a few resonances. The resonant and non-resonant amplitudes with the same quantum numbers do interfere. In the one-level, one channel R-matrix approach, the resonant amplitude $U^{\rm R}_{l_f l_i I J_f J_i}(E_{xA})$ for the capture into the resonance with energy E_R and spin J_i, and subsequent decay into the bound state with spin J_f, is given by

$$U^{\rm R}_{l_f l_i I J_f J_i}(E_{xA}) = -{\rm i}e^{{\rm i}(\omega_{l_i} - \phi_{l_i})} \frac{[\Gamma_{xAl_i I J_i}(E_{xA})]^{1/2} [\Gamma^{J_i}_{\gamma J_f}(E_{xA})]^{1/2}}{E_{xA} - E_R + {\rm i}\frac{\Gamma_{J_i}(E_{xA})}{2}}. \tag{3.3}$$

The phase factor ϕ_{l_i} is the solid sphere scattering phase shift in the l_ith partial wave and ω_{l_i} is given by

$$\omega_{l_i} = \sum_{n=1}^{l_i} \tan^{-1}\left(\frac{\eta_i}{n}\right), \tag{3.4}$$

where $\eta_i = Z_x Z_A \mu_{xA}/k_{xA}$ is the Coulomb parameter in the initial state, Z_j is the charge of the particle j. $[\Gamma_{xAl_i I J_i}(E_{xA})]^{1/2}$ is real and its square, $\Gamma_{xAl_i I J_i}(E_{xA})$, is the observable partial width of the resonance in the channel $x + A$ with the given set of quantum numbers, and $\Gamma_{J_i}(E_{xA})$ is the total resonance width which we approximate as $\Gamma_{J_i}(E_{xA}) \approx \sum_I \Gamma_{xAl_i I J_i}(E_{xA})$; $[\Gamma^{J_i}_{\gamma J_f}(E_{xA})]^{1/2}$ is complex and its modulus square is the observable radiative width:

$$\Gamma^{J_i}_{\gamma J_f}(E_{xA}) = |[\Gamma^{J_i}_{\gamma J_f}(E_{xA})]^{1/2}|^2. \tag{3.5}$$

The energy dependence of the partial and radiative widths are given by

$$\Gamma_{xAl_i I J_i}(E_{xA}) = \frac{P_{l_i}(E)}{P_{l_i}(E_R)} \Gamma_{xAl_i I J_i}(E_R) \tag{3.6}$$

and

$$\Gamma^{J_i}_{\gamma J_f}(E_{xA}) = \left(\frac{E_{xA} + \varepsilon^F_{xA}}{E_R + \varepsilon^F_{xA}}\right)^{2L+1} \Gamma^{J_i}_{\gamma J_f}(E_R) \tag{3.7}$$

respectively. Here, $\Gamma_{xAl_i I J_i}(E_R)$ and $\Gamma^{J_i}_{\gamma J_f}(E_R)$ are the experimental partial and radiative resonance widths, ε^F_{xA} is the binding energy of the bound state $F = (xA)$ for the virtual decay $F \to x + A$, and L is the multipolarity of the gamma-quanta emitted during the transition.

In a strict R-matrix approach the radiative width $\Gamma^{J_i}_{\gamma J_f}(E_{xA})$ can be expressed in terms of the real internal and complex external channel radiative widths amplitudes (Barker and Kajino 1991) as

$$\begin{aligned}\Gamma^{J_i}_{\gamma J_f}(E_{xA}) &= |-[\Gamma^{J_i}_{\gamma({\rm int})J_f}(E_{xA})]^{1/2} + [\Gamma^{J_i}_{\gamma({\rm ch})J_f}(E_{xA})]^{1/2}|^2 \\ &= ({\rm Re}[\Gamma^{J_i}_{\gamma({\rm ch})J_f}(E_{xA})]^{1/2} - [\Gamma^{J_i}_{\gamma({\rm int})J_f}(E_{xA})]^{1/2})^2 \\ &\quad + ({\rm Im}[\Gamma^{J_i}_{\gamma({\rm ch})J_f}(E_{xA})]^{1/2})^2.\end{aligned} \tag{3.8}$$

The channel radiative width amplitude is given by (Barker and Kajino 1991)

$$\begin{aligned}[\Gamma^{J_i}_{\gamma({\rm ch})J_f}(E_{xA})]^{1/2} &= \sqrt{2}{\rm i}^{l_i+L-l_f+1} \frac{1}{k} \mu_{xA}^{L+1/2} \\ &\quad \times \left(\frac{Z_x e}{m_x^L} + (-1)^L \frac{Z_A e}{m_A^L}\right) \sqrt{\frac{(L+1)\hat{L}}{L}} \frac{1}{\hat{L}!!} (k_\gamma R_{xA})^{L+1/2} \\ &\quad \times C^F_{xA\,l_f I J_f} \sqrt{\Gamma^{J_i}_{xAIl_i}(E_R)} \sqrt{P_{l_i}(E_{xA})} ([F_{l_i}(k, R_{xA})]^2 \\ &\quad + [G_{l_i}(k, R_{xA})]^2) \\ W_{-\eta^{\rm bs}_{xA}, l_f+1/2}&(2\kappa^F_{xA} R_{xA}) \\ &\quad \times (l_i 0 L 0 | l_f 0) U(L l_f J_i I; l_i J_f) J_L(l_f, l_i),\end{aligned} \tag{3.9}$$

with

$$\begin{aligned}J_L(l_f, l_i) &= J''_L(l_f, l_i) \\ &\quad + {\rm i}\frac{F_{l_i}(k, R_{xA}) G_{l_i}(k, R_{xA})}{F^2_{l_i}(k, R_{xA}) + G^2_{l_i}(k, R_{xA})} J'_L(l_f, l_i),\end{aligned} \tag{3.10}$$

Table 4. Summary of neutron transfer studies with ground state to ground state ANCs. Note that the quantum numbers and other labels have been dropped here for simplicity.

Reaction and n ANC	$C^2(\mathrm{fm}^{-1})$	p ANC	C^2 (fm^{-1})	Reference
^{13}C(^{7}Li,^{8}Li)^{12}C; $^{8}\mathrm{Li} \to {}^{7}\mathrm{Li} + \mathrm{n}$	0.432 ± 0.039	$^{8}\mathrm{B} \to {}^{7}\mathrm{Be} + \mathrm{p}$	0.455 ± 0.047	Trache *et al* (2003)
^{13}C(^{17}O,^{18}O)^{12}C; $^{18}\mathrm{O} \to {}^{17}\mathrm{O} + \mathrm{n}$	8.18 ± 0.76	$^{18}\mathrm{Ne} \to {}^{17}\mathrm{F} + \mathrm{p}$	12.15 ± 1.19	Al-Abdullah *et al* (2014)
^{13}C(^{22}Ne,^{23}Ne)^{12}C; $^{23}\mathrm{Ne} \to {}^{22}\mathrm{Ne} + \mathrm{n}$	$0.86 \pm 0.08 \pm 0.12$	$^{23}\mathrm{Al} \to {}^{22}\mathrm{Mg} + \mathrm{p}$	$4.63 \pm 0.77 \times 10^{3}$	Al-Abdullah *et al* (2010)

$$J''_L(l_f, l_i) = \frac{1}{R_{xA}^{L+1}} \int\limits_{R_{xA}}^{\infty} \mathrm{d}r r^L \frac{W_{-\eta_{xA}^{\mathrm{bs}}, l_f+1/2}(2\kappa_{xA}^F r)}{W_{-\eta_{xA}^{\mathrm{bs}}, l_f+1/2}(2\kappa_{xA}^F R_{xA})} \times \frac{F_{l_i}(k, r) F_{l_i}(k, R_{xA}) + G_{l_i}(k, r) G_{l_i}(k, R_{xA})}{F_{l_i}^2(k, R_{xA}) + G_{l_i}^2(k, R_{xA})}, \quad (3.11)$$

$$J'_L(l_f, l_i) = \frac{1}{R_{xA}^{L+1}} \int\limits_{R_{xA}}^{\infty} \mathrm{d}r r^L \frac{W_{-\eta_{xA}^{\mathrm{bs}}, l_f+1/2}(2\kappa_{xA}^F r)}{W_{-\eta_{xA}^{\mathrm{bs}}, l_f+1/2}(2\kappa_{xA}^F R_{xA})} \times \left[\frac{F_{l_i}(k, r)}{F_{l_i}(k, R_{xA})} - \frac{G_{l_i}(k, r)}{G_{l_i}(k, R_{xA})} \right]. \quad (3.12)$$

In (3.9),$C_{xA\, l_f I J_f}^F$ is ANC for the virtual decay $F \to x + A$,R_{xA} is the channel radius, which determines the border dividing the internal and external regions, and $U(Ll_f J_i I; l_i J_f)$ is a $6j$-symbol. Also $F_{l_i}(k, r)$ and $G_{l_i}(k, r)$ are the regular and singular (at the origin) solutions of the radial Schrödinger equation with the pure Coulomb potentials. The penetrability $P_{l_i}(E_{xA})$ is given by equation (2.78) and the momentum of the emitted photon is

$$k_\gamma = E_{xA} + \varepsilon_{xA}^F. \quad (3.13)$$

It is clear from equation (3.9) that to calculate the channel radiative width amplitude $[\Gamma_{\gamma(\mathrm{ch})J_f}^{J_i}(E_{xA})]^{1/2}$ we need to know only two experimentally measurable quantities, the ANC, $C_{xA\, l_f I J_f}^F$, and the partial resonance width $\Gamma_{xAl_i I J_i}(E_{xA})$. The relative phase of Re $[\Gamma_{\gamma(\mathrm{ch})J_f}^{J_i}(E_{xA})]^{1/2}$ and $[\Gamma_{\gamma(\mathrm{int})J_f}^{J_i}(E_{xA})]^{1/2}$ is, *a priori*, unknown, so these real parts may interfere either constructively or destructively. Hence, (Im $[\Gamma_{\gamma(\mathrm{ch})J_f}^{J_i}(E_{xA})]^{1/2})^2$ always provides a lower limit for the radiative width, and additional stronger limits may be obtained if assumptions are made about the interference between the two real contributions. For constructive interference of the real parts the channel contribution gives a stronger low limit as

$$\Gamma_{\gamma J_f}^{J_i}(E_{xA}) \geqslant (\mathrm{Re}[\Gamma_{\gamma(\mathrm{ch})J_f}^{J_i}(E_{xA})]^{1/2})^2 + (\mathrm{Im}[\Gamma_{\gamma(\mathrm{ch})J_f}^{J_i}(E_{xA})]^{1/2})^2 = \left| [\Gamma_{\gamma(\mathrm{ch})J_f}^{J_i}(E_{xA})]^{1/2} \right|^2. \quad (3.14)$$

In the case of the destructive interference of the real parts, if $|\mathrm{Re}\, [\Gamma_{\gamma(\mathrm{ch})J_f}^{J_i}(E_{xA})]^{1/2}| > |[\Gamma_{\gamma(\mathrm{int})J_f}^{J_i}(E_{xA})]^{1/2}|$, the channel contribution gives an upper limit for the radiative width. These limits depend only on one model parameter, the channel radius as

$$\Gamma_{\gamma J_f}^{J_i}(E_{xA}) \leqslant (\mathrm{Re}\, [\Gamma_{\gamma(\mathrm{ch})J_f}^{J_i}(E_{xA})]^{1/2})^2 + (\mathrm{Im}\, [\Gamma_{\gamma(\mathrm{ch})J_f}^{J_i}(E_{xA})]^{1/2})^2 = \left| [\Gamma_{\gamma(\mathrm{ch})J_f}^{J_i}(E_{xA})]^{1/2} \right|^2. \quad (3.15)$$

Thus the ANC plays an important role in determination of the radiative width because the normalization of the channel contribution is determined by the ANC.

Assuming that the experimental radiative width $\Gamma_{\gamma J_f}^{J_i}(E_R)$, the ANC of the bound state, and the resonance width $\Gamma_{xAl_i I J_i}(E_R)$ are known, we can determine the internal radiative width

$$\Gamma_{\gamma(\mathrm{int})J_f}^{J_i}(E_{xA}) = [\mathrm{Re}[\Gamma_{\gamma(\mathrm{ch})J_f}^{J_i}(E_{xA})]^{1/2} \pm \sqrt{\Gamma_{\gamma J_f}^{J_i}(E_{xA}) - (\mathrm{Im}[\Gamma_{\gamma(ch)J_f}^{J_i}(E_{xA})]^{1/2})^2}]^2 \quad (3.16)$$

with two possible solutions.

In the R-matrix method the internal non-resonant amplitude is absorbed into the internal resonance term, so that the non-resonant capture amplitude is entirely determined by the channel (external) term (Barker and Kajino 1991, Sobotka *et al* 2013):

$$U_{Il_f l_i J_f J_i}^{\mathrm{NR}}(E_{xA}) = -\mathrm{i}(2)^{3/2} \mathrm{i}^{l_i+L-l_f+1} \mathrm{e}^{\mathrm{i}(\omega_{l_i} - \phi_{l_i})} \frac{1}{k} \mu_{xA}^{L+1/2} \times \left(\frac{Z_x e}{m_x^L} + (-1)^L \frac{Z_A e}{m_A^L} \right) \sqrt{\frac{(L+1)\hat{L}}{L}} \frac{1}{\hat{L}!!} (k_\gamma R_{xA})^{L+1/2} \times C_{xA\, l_f I J_f}^F F_{l_i}(k, R_{xA}) G_{l_i}(k, R_{xA}) W_{-\eta_{xA}^{\mathrm{bs}}, l_f+1/2}(2\kappa_{xA}^F R_{xA}) \times \sqrt{P_{l_i}(E_{xA})} (l_i 0 L 0 | l_f 0) U(L l_f J_i I; l_i J_f) J'_L(l_i l_f), \quad (3.17)$$

which contains the same ANC as the channel radiative width amplitude $[\Gamma_{\gamma(\mathrm{ch})J_f}^{J_i}(E)]^{1/2}$. Such a normalization of the channel radiative width and non-resonant amplitudes is physically transparent. Both quantities describe peripheral processes and, hence, contain the tail of the overlap function, whose normalization is given by the corresponding ANC.

The sum of the interfering resonant and non-resonant amplitudes is given by (Barker and Kajino 1991)

$$U_{l_f l_i I J_f J_i}^{\mathrm{R}}(E_{xA}) = U_{l_f l_i I J_f J_i}^{\mathrm{R(int)}}(E_{xA}) + U_{l_f l_i I J_f J_i}^{\mathrm{R(ch)}}(E_{xA}) + U_{l_f l_i I J_f J_i}^{\mathrm{NR}}(E_{xA}). \quad (3.18)$$

The internal and external resonant radiative capture amplitudes, describing the capture of the incident particle x by A into the resonant state with subsequent decay to the bound state at distances $r \leqslant R_{xA}$ and $r > R_{xA}$, correspondingly, are given by

$$U_{l_f l_i I J_f J_i}^{\mathrm{R(int)}}(E_{xA}) = \mathrm{i}\mathrm{e}^{\mathrm{i}(\omega_{l_i} - \phi_{l_i})} \times \frac{[\Gamma_{xAl_i I J_i}(E_{xA})]^{1/2} [\Gamma_{\gamma(\mathrm{int})J_f}^{J_i}(E_{xA})]^{1/2}}{E_R - E_{xA} - \mathrm{i}\frac{\Gamma^{J_i}(E_{xA})}{2}} \quad (3.19)$$

and

$$U^{\mathrm{R(ch)}}_{l_f l_i I\, J_f J_i}(E_{xA}) = -\mathrm{i}\mathrm{e}^{\mathrm{i}(\omega_{l_i}-\phi_{l_i})} \frac{[\Gamma_{xAl_i I\, J_i}(E_{xA})]^{1/2}[\Gamma^{J_i}_{\gamma(\mathrm{ch})J_f}(E_{xA})]^{1/2}}{E_R - E_{xA} - \mathrm{i}\frac{\Gamma_{J_i}(E_{xA})}{2}}. \tag{3.20}$$

The relative sign of the $U^{\mathrm{R(ch)}}_{l_f l_i I\, J_f J_i}(E_{xA})$ and $U^{\mathrm{NR}}_{l_f l_i I\, J_f J_i}(E_{xA})$, which determines the pattern of their interference, is well known because both contain the same factor $[\Gamma_{xAl_i I J_i}(E_{xA})]^{1/2}$ $\times[\Gamma^{J_i}_{\gamma(\mathrm{ch})J_f}(E_{xA})]^{1/2}$. The sign of the internal part, which dictates the interference pattern with the channel and non-resonant amplitudes, is not known and can be determined only from the microscopic calculations. If the channel resonance amplitude $|U^{\mathrm{R(ch)}}_{l_f l_i I\, J_f J_i}(E_{xA})|$ dominates over the internal part, the interference character of the resonant and non-resonant amplitudes can be easily determined. This constitutes another important role of the ANC in the analysis of the radiative capture reactions when the interference of the resonant and non-resonant mechanisms occur.

In Sobotka *et al* (2013) the radiative capture in ^{11}C(p, γ)^{12}N, in which interference of direct and resonance mechanisms occur, was analyzed. The channel radiative width amplitude of the second resonance of ^{12}N decaying to the ground state was estimated to be $[\Gamma^{J_i}_{\gamma(\mathrm{ch})J_f}(E_{xA})]^{1/2} = 0.000\,154 + \mathrm{i}0.000\,0273\,\mathrm{MeV}^{1/2}$. This value was obtained using the ANC measured in Tang *et al* (2003) and the resonance width determined in Sobotka *et al* (2013).. A simple single-particle estimate gives $[\Gamma^{J_i}_{\gamma(\mathrm{int})J_f}(E_{xA})]^{1/2} = 0.000\,043\,\mathrm{MeV}^{1/2}$, which is significantly smaller than the real part of the channel radiative width amplitude and from the single-particle estimates we find that the channel $U^{\mathrm{R(ch)}}_{l_f l_i I\, J_f J_i}(E_{xA})$and the internal resonant amplitude $U^{\mathrm{R(int)}}_{l_f l_i I\, J_f J_i}(E_{xA})$ have constructive interference. Hence $|[\Gamma^{J_i}_{\gamma(\mathrm{ch})J_f}(E_{xA})]^{1/2}|^2 = 24.5\,\mathrm{meV} < \Gamma^{J_i}_{\gamma J_f}(E_{xA})$ gives the lower limit of the radiative width.

In Banu *et al* (2009) the astrophysical factor for the ^{12}N(p, γ)^{13}O reaction was calculated using the measured ANC. This S factor has contributions from the interfering resonant and non-resonant amplitudes. The radiative width of the resonance energy, $E_R = 2.75\,\mathrm{MeV}$, decaying to the ground state via an $E1$ transition is dominated by the channel radiative width amplitude, which is about of a factor of 3 larger than the internal width calculated in the single-particle model. The calculated radiative width of this resonance based on the measured ANC is 0.95 eV (for a channel radius 4.25 fm) is significantly larger than the value of 24 meV used in Wiescher *et al* (1989). From equation (3.8) we conclude that $\Gamma^{J_i}_{\gamma J_f}(E_R) > (\mathrm{Im}[\Gamma^{J_i}_{\gamma(\mathrm{ch})J_f}(E_R)]^{1/2})^2 = 40\,\mathrm{meV}$, which indicates that the radiative width of 24 meV was undervalued.

4. Applications of the THM

The THM has been successfully applied to several reactions that are important in astrophysics, nuclear, and atomic physics. The reactions studied by means of the THM are summarized in table 5. Some of the results were included in the recent compilation of astrophysical factors of interest for nucleosynthesis and energy production in the Sun (Adelberger *et al* 2011).

These reactions can be divided into two broad categories, as discussed in the theoretical section, namely resonant and non-resonant processes. A large number of indirect investigations with the THM have been focused on the study of (p,α) reactions at stellar energies since they play a key role in many stellar nucleosynthesis scenarios. Most of these measurements were performed in inverse kinematics with a deuterated polyethylene target to supply virtual protons from the deuteron. An alternative source of virtual protons (and deuterons) is represented by ^{3}He, as shown by several indirect measurements (Tumino *et al* 2006, 2011 and Pizzone *et al* 2011). All the TH-nuclei used so far in experiments are characterized by an orbital angular momentum $l = 0$ for the x–s intercluster motion, though other systems with $l = 1$ orbital angular momentum are available, like $^7\mathrm{Li} = t + \alpha$.

Below we will review the basic requirements to be fulfilled to effectively apply the THM.

4.1. THM: from theory to experiments

In section 2.2 devoted to the illustration of the theoretical framework of the THM, it has been shown that under QF kinematical conditions non-THM reaction mechanisms are suppressed, as the $M^{\mathrm{PWA(post)}}_{\mathrm{int}}(P, \boldsymbol{k}_{aA})$ term, containing the interaction potential V_{sx} involving the spectator, may be small and so only the terms in the total amplitude proportional to the OES S-matrix elements $S^{J_F}_{bBjl;xAj'l'}$ can be retained. The second important feature pointed out by equation (2.75), in the case of direct reactions, and by equation (2.79) in the case of resonant reactions, is that the total prior PWA amplitude is proportional to the wave function of the TH-nucleus a in momentum space, $\varphi_a(\boldsymbol{p}_{sx})$. Therefore, the advanced THM formalism based on the surface integral approach (Kadyrov *et al* 2009, Mukhamedzhanov 2011) can be regarded as an extension and generalization of the simplified THM formulas based on the impulse approximation (Chew and Wick 1952), which have been used in the original works focused on the investigation of QF reactions (see Spitaleri (1991) and references therein). This is a consequence of the historical development of the method, as an extension of the measurements of the excitation function of 2 → 3 reaction cross sections for QF reactions at low energies (Lattuada *et al* 1985, Zadro *et al* 1989, Calvi *et al* 1990). In these works, a simple PWA expression for the TH cross section was adopted:

$$\frac{\mathrm{d}^3\sigma}{\mathrm{d}\Omega_b\,\mathrm{d}\Omega_B\,\mathrm{d}E_b} \propto KF\;|\varphi_a(\boldsymbol{p}_{sx})|^2\,\frac{\mathrm{d}\sigma_{xA\to bB}}{\mathrm{d}\Omega}\bigg|_{\mathrm{HOES}}, \tag{4.1}$$

showing a straightforward connection between the 2 → 3 cross section and the one of the binary reaction. In this formula, KF is a kinematical factor containing the final state phase space factor and it is a function of the masses m_i, momenta k_i and angles θ_i of the outgoing particles (see Spitaleri *et al* (2004) for its explicit expression). $|\varphi_a(\boldsymbol{p}_{sx})|^2$, which is the squared Fourier transform of the radial wave function of the $a = (sx)$ system, represents the momentum distribution of the s–x intercluster motion, usually described in terms of Hänkel, Eckart or

Table 5. Two-body reactions studied via the THM (first column). In the next columns, the THM reaction, the beam energy and the Q−value of the three-body reactions (Q_3) are shown, respectively. In the fifth column the THM nucleus and the transferred cluster are reported. Finally, in the last column the reference for each reaction is given.

Reaction	THM reaction	E_{beam} (MeV)	Q_3 (MeV)	THM nucleus (x-cluster)	Reference
^{7}Li(p,α)^{4}He	^{2}H(^{7}Li,$\alpha\alpha$)n	19–22, 28–48	15.122	^{2}H (p)	Zadro *et al* (1989) Spitaleri *et al* (1999) Lattuada *et al* (2001) Aliotta *et al* (2000)
^{7}Li(p,α)^{4}He	^{7}Li(^{3}He,$\alpha\alpha$)^{2}H	33	11.853	^{3}He (p)	Tumino *et al* (2006)
^{6}Li(p,α)^{3}He	^{2}H(^{6}Li,α^3He)n	14.25, 21.6–33.6 25	1.795	^{2}H (p)	Tumino *et al* (2003) Tumino *et al* (2004) Calvi *et al* (1990) Lamia *et al* (2013)
^{6}Li(d,α)^{4}He	^{6}Li(^{3}He,$\alpha\alpha$)^{1}H	17.5	16.879	^{3}He (p)	Pizzone *et al* (2011)
^{6}Li(d,α)^{4}He	^{6}Li(^{6}Li,$\alpha\alpha$)^{4}He	5	22.372	^{6}Li (d)	Cherubini *et al* (1996) Spitaleri *et al* (2001)
^{9}Be(p,α)^{6}Li	^{2}H(^{9}Be,α^6Li)n	22.35	−0.099	^{2}H (p)	Romano *et al* (2006) Wen *et al* (2008)
^{10}B(p,α)^{7}Be	^{2}H(^{10}B,α^7Be)n	27	−1.079	^{2}H (p)	Lamia *et al* (2009, 2010)
^{11}B(p,α)^{8}Be	^{2}H(^{11}B,α^8Be)n	27	6.366	^{2}H (p)	Spitaleri *et al* (2004) Lamia *et al* (2012a)
^{15}N(p,α)^{12}C	^{2}H(^{15}N,α^{12}C)n	60	2.741	^{2}H (p)	La Cognata *et al* (2006, 2007, 2009)
^{18}O(p,α)^{15}N	^{2}H(^{18}O,α^{15}N)n	54	1.755	^{2}H (p)	La Cognata *et al* (2008a, 2008b, 2010a, 2010b) Palmerini *et al* (2013)
^{19}F(p,α)^{16}O	^{2}H(^{19}F,α^{16}O)n	50	5.889	^{2}H (p)	La Cognata *et al* (2011)
^{17}O(p,α)^{14}N	^{2}H(^{17}O,α^{14}N)n	45	−1.033	^{2}H (p)	Sergi *et al* (2010) Palmerini *et al* (2013)
^{3}He(d,p)^{4}He	^{6}Li(^{3}He,pα)^{4}He	5.6	16.879	^{6}Li (d)	La Cognata *et al* (2005)
^{2}H(d,p)^{3}H	^{2}H(^{6}Li,p^{3}H)^{4}He	14	2.559	^{6}Li (d)	Rinollo *et al* (2005) Pizzone *et al* (2013)
^{2}H(d,p)^{3}H	^{2}H(^{3}He,p^{3}H)^{1}H	18	−1.461	^{3}He (d)	Tumino *et al* (2011)
^{2}H(d,n)^{3}He	^{2}H(^{3}He,n^{3}He)^{1}H	18	−2.225	^{3}He (d)	Tumino *et al* (2011)
^{12}C(α,α)^{12}C	^{6}Li(^{12}C,α^{12}C)^{2}H	16, 20	−1.474	^{6}Li (α)	Spitaleri *et al* (2000)
^{6}Li(n, α)^{3}H	^{2}H(^{6}Li,α^3H)^{1}H	14	2.559	^{2}H (n)	Tumino *et al* (2005) Gulino *et al* (2010)
^{17}O(n,α)^{14}C	^{2}H(^{17}O,α^{14}C)^{1}H	41, 43.5	−0.407	^{2}H (n)	Gulino *et al* (2013)
^{1}H(p,p)^{1}H	^{2}H(p,pp)n	5.6	2.224	^{2}H (p)	Tumino *et al* (2007, 2008)
^{12}C(^{12}C,α)^{20}Ne	^{12}C(^{16}O,α^{20}Ne)^{4}He	25	−2.545	^{16}O (^{12}C)	—
^{19}F(α,p)^{22}Ne	^{19}F(^{6}Li,p^{22}Ne)^{2}H	6	0.199	^{6}Li (α)	—
^{13}C(α,n)^{16}O	^{13}C(^{6}Li,n^{16}O)^{2}H	7.82	0.742	^{6}Li (α)	La Cognata *et al* (2012, 2013)

Hulthén functions depending on the s–x system properties. Finally, $\frac{\mathrm{d}\sigma_{xA\to bB}}{\mathrm{d}\Omega}|_{\mathrm{HOES}}$, which is essentially the modulus square of equation (2.71), is the HOES cross section. As it has been pointed out in section 2.2.2, where a short derivation of equation (4.1) is given (compare equations (2.70) and (2.71)), the HOES cross section approaches the OES one only when $E_{xA} \gg \varepsilon^a_{sx}$ as $p_{xA} \approx k_{xA}$. In the case $E_{xA} \to 0$, which is the most interesting for astrophysics, the HOES amplitude does not contain penetrability factors making it possible to extend the measurement of the binary reaction cross section down to astrophysical energies. However, HOES effects are sizeable under this hypothesis, making it necessary to introduce correction factors to retrieve the energy dependence of the binary sub-reaction cross section. Moreover, a number of validity tests were necessary to verify the applicability of equation (4.1).

In the early applications, the HOES cross section was linked to the OES one by introducing the correct penetration factor that, in the case of charged particle induced reactions, is given by equation (2.78). In the case of neutron-induced reactions ($x = n$), where the Coulomb barrier is obviously absent in the entrance channel, if the $n + A \to b + B$ reaction occurs with $l > 0$, the cross section can be suppressed due to the centrifugal barrier. Thus appropriate penetration factors had to be introduced to deduce the OES cross section from the experimental HOES one. For the charged particles x and A, the penetrability factor is given by equation (2.78). For $x = n$

$$P_l(E_{xA}) = \frac{1}{k_{xA}R_{xA}\left(j_l^2(k_{xA}R_{xA}) + n_l^2(k_{xA}R_{xA})\right)}, \tag{4.2}$$

with j_l and n_l the spherical Bessel function and the Neumann function, respectively. Then, the OES cross section was obtained taking the product:

$$\left.\frac{\mathrm{d}\sigma_{xA\to bB}}{\mathrm{d}\Omega}\right|_{\mathrm{OES}} = P_l(E_{xA})\left.\frac{\mathrm{d}\sigma_{xA\to bB}}{\mathrm{d}\Omega}\right|_{\mathrm{HOES}}, \tag{4.3}$$

which is expressed, however, in arbitrary units owing to the PWA that allows one to deduce the energy dependence of the cross section but not its absolute value.

More recently, the modified R-matrix method has led to a more sophisticated treatment of the triple differential cross section, in the case of both direct and resonant reactions. The total prior PWA amplitude in the case of direct reactions was given in equation (2.75) and in the case of resonant reactions in equation (2.79). The amplitudes of the $2 \to 3$ reactions are proportional to the OES S-matrix elements and to the OES $[\boldsymbol{A}^{-1}]_{\nu\tau}$ inverse level matrix elements, respectively. However, both total prior PWA amplitudes contain the $P_l^{-\frac{1}{2}}(k_{xA}R_{xA})$ factor, namely, the inverse square root of the penetration factor for the xA entrance channel compensating for the Coulomb barrier suppression effect on the cross section and making it possible to extend the measurement of the binary cross section down to astrophysical energies with no suppression. In the modified R-matrix approach the link between the triple differential cross section $\frac{\mathrm{d}^3\sigma}{\mathrm{d}\Omega_b\,\mathrm{d}\Omega_B\,\mathrm{d}E_b}$ and the OES one is ensured by the presence in the total PWA amplitudes of the same matrix elements (S-matrix or level matrix, for direct and resonant reaction, respectively) as in the OES binary reaction cross section. These parameters can be deduced by fitting the measured $\frac{\mathrm{d}^3\sigma}{\mathrm{d}\Omega_b\,\mathrm{d}\Omega_B\,\mathrm{d}E_b}$ cross section using the TH cross section calculated from the PWA amplitudes mentioned above. The obtained matrix elements (that is, in the case of resonant reactions, the reduced widths γ) are then used to calculate the OES cross section to be compared with the results of direct measurements. This approach has the advantage of permitting to account for HOES effects, due to the virtual nature of the transferred particle x, which can be treated only heuristically when equation (4.1) is used in the data analysis. Moreover, when sub-threshold resonances contribute to the astrophysical reactions, as the 6.356 MeV state in ^{17}O determining an enhancement of the astrophysical factor right at astrophysical energies, the modified R-matrix approach allows us to determine the ANC of such states (La Cognata *et al* 2012, 2013).

4.2. THM experiment preparation

A necessary condition for the application of THM equations is that the QF mechanism yields a dominant contribution to the $2 \to 3$ cross section. This means that only the diagram in figure 2 can be used to depict the TH data and higher order diagrams are negligible (pole approximation). The intercluster momentum range where the pole diagram is expected to be dominant in the reaction mechanism was suggested to be $p_{sx} < \kappa_{sx}^{a}$ (Shapiro 1967a, 1967b, La Cognata *et al* 2007, Spitaleri *et al* 2011). However, competing reaction mechanisms such as direct breakup and sequential processes might contribute as well or even be dominant inside this relative momentum region (La Cognata *et al* 2005). For this reason, careful experiment planning and off-line validity tests are necessary to identify and single out the kinematic region where the pole diagram is mostly contributing and where the theoretical formalism discussed in the previous sections can be applied to deduce the OES cross section.

Table 6. Structure (x–s cluster structure), orbital angular momentum for the x–s relative motion and binding energy of some TH-nuclei.

TH nucleus	x–s cluster structure	Orbital angular momentum	Binding energy (MeV)
^{2}H	p–n	0	2.225
^{3}H	d–n	0	6.257
^{3}He	d–p	0	5.493
^{6}Li	d–α	0	1.474
^{9}Be	^{5}He–α	0	2.464
^{16}O	^{12}C–α	0	7.162
^{20}Ne	^{16}O–α	0	4.730

A first task in planning a THM measurement is the selection of an appropriate $a + A \to b + B + s$ reaction and therefore of a suitable TH-nucleus that has a large amplitude for the $a = (xs)$ cluster configuration. In table 6 a list of possible TH-nuclei, many of them already used in THM experiments, is shown with the corresponding cluster x (participant). In some cases, different choices of TH-nuclei are available to get the same virtual particle x. We note from table 6 that a participant proton, for example, can be transferred either off a deuteron $^2\mathrm{H} = (\mathrm{pn})$, in which case neutron acts as a spectator (binding energy $\varepsilon_{pn}^{d} = 2.225$ MeV) or off $^3\mathrm{He} = (\mathrm{pd})$ with deuteron as spectator ($\varepsilon_{pd}^{3\mathrm{He}} = 5.493$ MeV). A virtual participant α-particle can be transferred off different nuclei, such as ^{6}Li, ^{9}Be or ^{16}O.

The choice of an appropriate TH-nucleus among those made up of the same participant cluster x but different spectator s is mainly linked to (Chew and Wick 1952, Barbarino *et al* 1980, Spitaleri *et al* 2011):

- the minimum value of binding energy for the $a = (xs)$ system;
- the population of kinematic regions where sequential processes, namely multistep reactions proceeding through decay of intermediate compound systems instead of direct transfer are minimized;
- the Q-value of the $a+A \to b+B+s$ reaction and, therefore, the value of the transferred momentum;
- the knowledge of the x–s momentum distribution.

In particular, the choice of deuteron as a TH-nucleus to obtain a virtual proton beam is suggested by a number of reasons:

- it has a simple structure (proton plus neutron) and its wave function is well known;
- binding energy is low (see table 6);
- the spectator cluster is a neutral particle (neutron), reducing the probability of rescattering in the exit channel;
- the momentum distribution of the p–n intercluster motion has a maximum at $p_{sx} = 0$ MeV/c, the intercluster motion taking place in s-wave.

In addition, the deuteron can be used as a source of both virtual protons and neutrons (Tumino *et al* 2005, Gulino *et al* 2010, 2013), thus allowing for investigations of neutron-induced reactions avoiding the experimental problems connected to the use of neutron beams, at the same time as p-induced reactions are measured (as in the case of the ^{6}Li + d interaction).

Beam energies are chosen with the aim to maximize the QF contribution in comparison with other reaction mechanisms, such as sequential processes, and to overcome the Coulomb barrier in the $A + a$ channel, V_{aA}^{C}. In this way, the cluster x is brought inside the $x + A$ nuclear interaction region to induce the $x(A, b)B$ reaction without being affected by Coulomb suppression of the cross section due to the Coulomb penetration factor. Also the incident energy in the center-of-mass system E_{aA} as well as the detection angles have to be chosen so that the relative energy E_{xA} can span the astrophysical region of interest below the Coulomb barrier, $E_{xA} < V^C_{xA}$. This is possible because the initial projectile energy is compensated for by the binding energy ε^a_{xs} of particle x inside a as shown by equation (2.63). Moreover, if the QF condition is slightly relaxed, the intercluster motion can be used to cover a limited E_{xA} region (La Cognata *et al* 2007), thus allowing one to explore the Gamow window even using comparatively large beam energies. This property might be very useful in the investigations of reactions induced by unstable nuclei, since in these cases the energy presently available at most facilities can be too large for the THM application (see, for instance, Cherubini *et al* (2012)).

It is worth noting that, thanks to the energy associated to the x–s intercluster motion, by using a single beam energy E_{beam} the whole excitation function of the $x + A \rightarrow b + B$ reaction can be measured, spanning the entire interval of astrophysical importance.

Energy resolution in the x–A channel is a crucial issue especially in the resonant reaction case as resolution has to be good enough to separate the contribution of each level to the THM cross section. The kinematical variable mostly influencing energy resolution is the relative angle of emission of the two detected particles. Indeed, in a typical experiment two out of the three emitted particles in a reaction event are detected in coincidence in two or more pairs of coincidence telescopes arranged on opposite sides of the beam direction, often located at quite forward QF angles as the experiments are usually performed in inverse kinematics. QF angles are defined as those at which the QF condition is best fulfilled, e.g. those at which $p_{sx} = 0$ in the case of a dominant s-wave in the x–s relative motion. The uncertainty affecting the measured angles can be kept below 0.2° by using a well collimated beam coupled to position sensitive detectors (PSDs), leading to an energy resolution as good as 17 keV (La Cognata *et al* 2010a), which is usually adequate to isolate resonances in the $A = 20$ mass region. However, for some applications better resolution is necessary, for instance in the case of neutron-induced reactions at very low energies (Gulino *et al* 2010).

The ‘magnifying glass’ effect (Baur *et al* 1986) can be used to improve the relative energy resolution in reactions having three particles in the exit channel and so, as a particular case, it can be useful in the extraction of x–A relative energy spectra in THM reactions. Under peculiar kinematic conditions, E_{xA} shows weak dependence on the energies of the detected particles, thus their uncertainties give a small contribution to the E_{xA} total error budget, as can be demonstrated by applying standard error propagation formulas.

4.3. From the $a + A \rightarrow b + B + s$ cross section to the $x + A \rightarrow b + B$ one

Several different reactions can be induced on the same target owing to the presence of contaminants or several open channels. These parasitic reactions might introduce background that has to be identified and removed. The 2 → 3 reactions allow for a number of kinematic tests suited to disentangle the $a + A \rightarrow b + B + s$ channel from others, which complement the standard particle identification approaches, such as the $\Delta E - E$ technique. Since both the angle of emission and the kinetic energy of two of the three outgoing particles are detected and these lay on the same plane as the impinging nucleus, the Q−value spectrum for the coincidence events can be deduced and compared with the theoretical value, calculated taking the mass of the undetected particle from the energy–momentum plot, as discussed in Costanzo *et al* (1990).

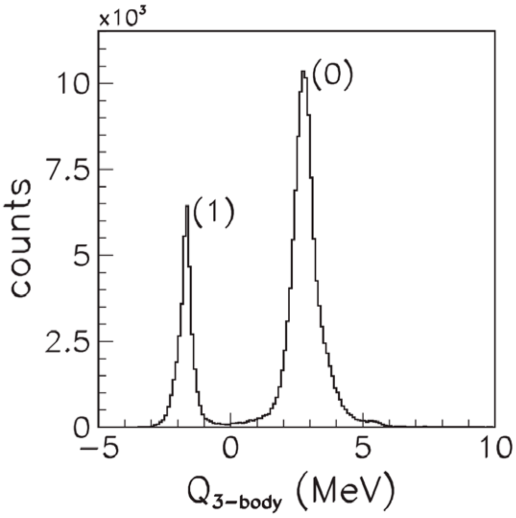

Figure 15. Q-value spectrum obtained in La Cognata *et al* (2007). It shows two peaks, corresponding to two reaction channels, namely (0) the ^{2}H(^{15}N,α_0^{12}C)n reaction, in which ^{12}C is emitted in its ground state, and (1) the ^{2}H(^{15}N,α_1^{12}C)n reaction, where the first excited state of ^{12}C is populated in the reaction.

Figure 15 shows a typical Q-value spectrum for a 2 → 3 reaction, in this case for the ^{2}H(^{15}N,α^{12}C)n reaction (La Cognata *et al* 2007). In the spectrum two peaks are apparent, corresponding to two reaction channels, in which ^{12}C is emitted with different excitation energies. In this case, particle identification cannot be used to single out the channel of interest while they appear well separated in the Q-value spectrum. The Q-value spectrum is also a good test to check the accuracy of detector calibration, as peak position is very sensitive to changes on the position and energy calibration parameters.

The same $a + A \rightarrow b + B + s$ channel can be fed through different reaction mechanisms. Apart from the diagram in figure 2, other processes might be needed to describe the reaction and kinematics cannot be used to disentangle them. However, the analysis of reaction dynamics can be used to shed light on the dominant reaction mechanism. Some of them are shown in figure 16 for the case of the ^{2}H(^{18}O,α^{15}N)n reaction (La Cognata *et al* 2007). Panel (*a*) describes a QF process, as the one given in figure 2, that is, the reaction mechanism of interest for the THM application. Panels (*b*)–(*d*) show, instead, two-step sequential decays where the neutron cannot be regarded as a spectator in the ^{18}O(p,α)^{15}N sub-reaction, the one of astrophysical interest. The processes marked with (*c*)

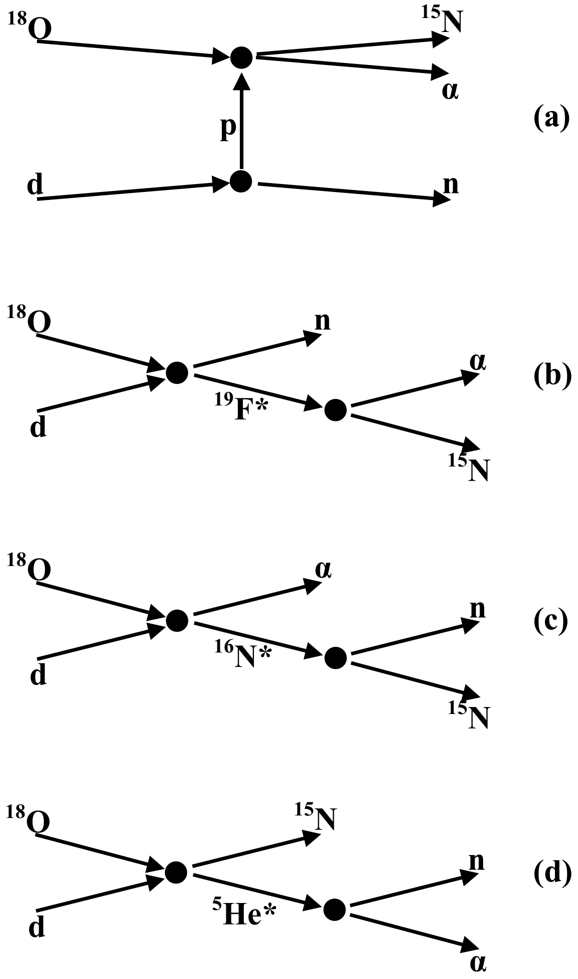

Figure 16. Diagrams representing different reaction mechanisms leading to the population of the same $\alpha + ^{15}$N + n channel in the ^{2}H(^{18}O,α^{15}N)n reaction (La Cognata *et al* 2007). (*a*) depicts a QF process, the other panels display sequential processes proceeding through the population of intermediate compound nuclei, ^{19}F (*b*), ^{16}N (*c*) and ^{5}He (*d*).

and (*d*) in figure 16 can be singled out by analyzing the relative energy spectra of any two out of the three emitted particles. If compound nuclei form, different from $F = bB$ (^{19}F in the case of the ^{2}H(^{18}O,α^{15}N)n reaction), later decaying to the observed final state, peaks should appear that correspond to levels populated following the $a + A$ interaction. For example, in the case of figure 16(*c*), a spectrum of the n–^{15}N relative energy should show evidence of a resonance if ^{16}N excited states are populated. Figure 17 is an example of this reaction mechanism investigation applied to the ^{2}H(^{18}O,α^{15}N)n process (La Cognata *et al* 2010a). In this case, two-dimensional energy correlation spectra display only loci corresponding to ^{19}F states, ruling out sequential decays of ^{5}He or ^{16}N. However, this approach cannot establish whether resonances in the $F = bB$ system are populated through a QF process or a sequential decay.

An observable very sensitive to the reaction mechanism is the shape of the experimental momentum distribution of the cluster s in the TH-nucleus a. Indeed, if the $a + A \to b + B + s$ reaction is direct and can be described by the diagram in figure 2, s should keep the same momentum as inside A, thus the comparison of the experimental and theoretical momentum distributions can be used to disentangle the QF reaction mechanism from others (as, for instance, in La Cognata *et al* (2005)). Moreover, the investigation of the x–s relative motion momentum distribution constitutes an important validity test of the theoretical formalism adopted in the data analysis (La Cognata *et al* 2010c).

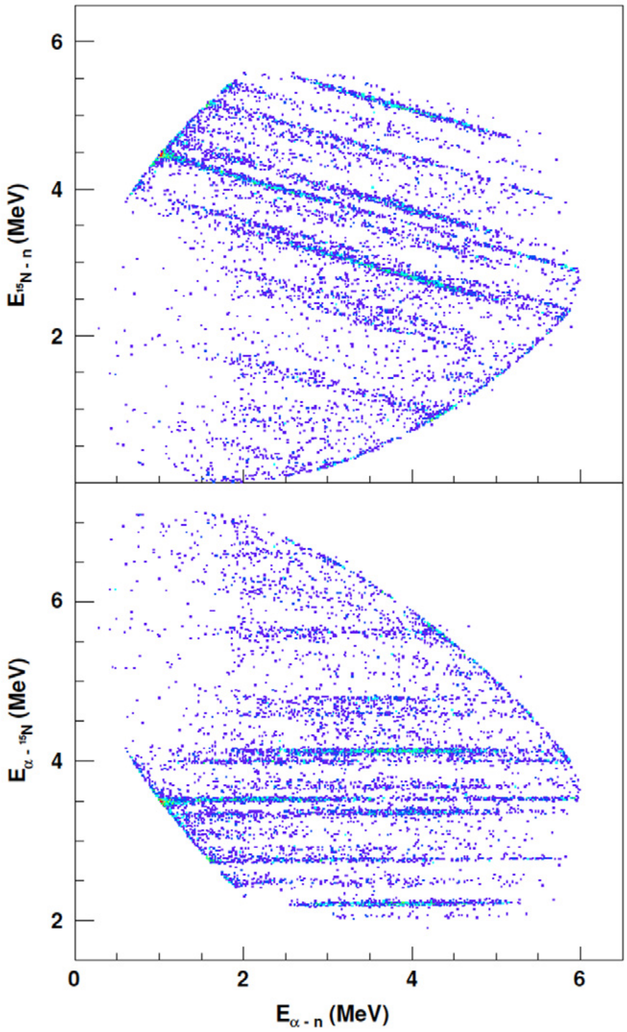

Figure 17. Energy correlation spectra for the ^{2}H(^{18}O,α^{15}N)n reaction (La Cognata *et al* 2010a). Horizontal loci in the lower panel correspond to ^{19}F excited states. No additional loci appear, thus no sequential decay proceeding through the population of ^{5}He or ^{16}N excited states are present.

The recoil momentum of cluster s can be determined from kinematics of the $2 \to 3$ reaction, even though this particle is not detected, as in the case s is a neutron (Ohlsen 1965). The experimental momentum distribution can be deduced using different approaches, the angular correlation and the energy sharing techniques, for instance (Kasagi *et al* 1975). Here we will discuss about the latter, which has been adopted in most of the recent THM works. Equations (2.75) and (2.79), describing the $2 \to 3$ process under QF kinematic conditions, show that in a restricted range of E_{xA} and of $\theta_{\rm cm} = \cos^{-1} \hat{k}_{xA} \cdot \hat{k}_{bB}$, the total PWA amplitudes for direct and resonant reactions are proportional to the x–s wave function in momentum space

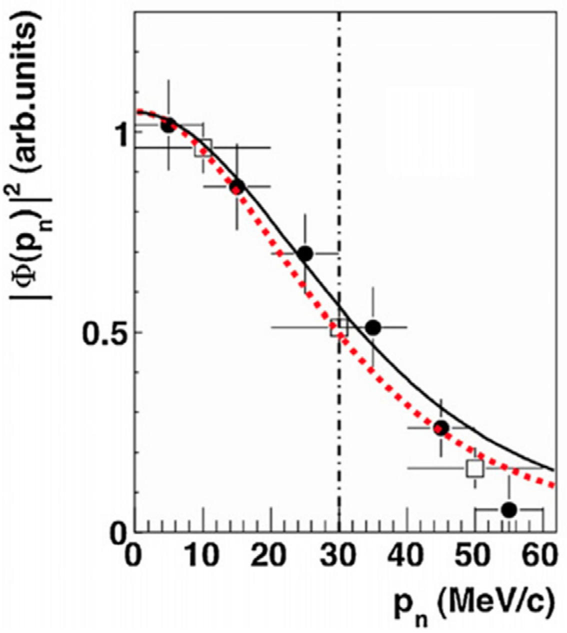

Figure 18. Experimental momentum distribution (full circles and open squares) of n inside d from the ^{2}H(^{11}B, α_0^8Be)n reaction (Lamia *et al* 2012a). The red dotted line is the theoretical momentum distribution in PWA, the squared Hulthén function in momentum space. The black solid line is a fit of the momentum distribution leaving as free parameters coefficients $a$and b appearing in the analytical expression equation (4.4).

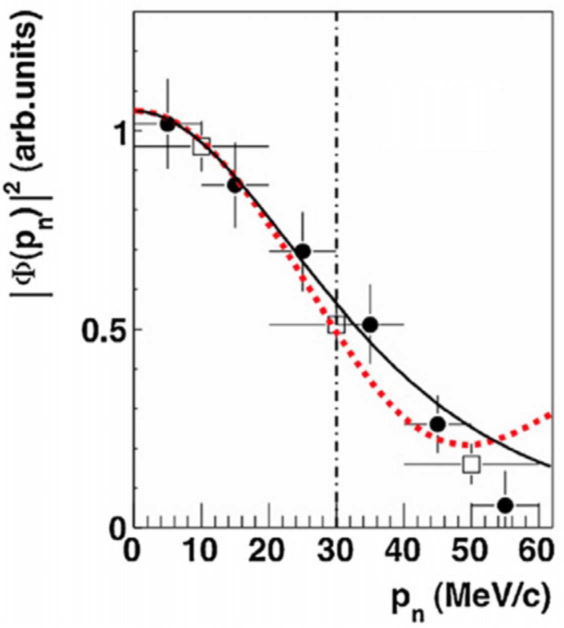

Figure 19. Same as figure 18, where the red dotted line highlights the momentum distribution obtained in the DWBA framework, using the computer code FRESCO (see Lamia *et al* (2012a) for details).

through a constant factor, describing the binary sub-reaction. Therefore, the analysis of the 2 → 3 reaction yield leads to the determination of the experimental momentum distribution if the appropriate kinematical cuts are imposed onto the data and if the kinematic factor KF, describing the population of the phase space in the 2 → 3 process, is divided out.

In figure 18 the experimental spectrum of neutron momenta, divided by the kinematic factor KF, is displayed, as obtained from the ^{2}H(^{11}B, α_0^8Be)n reaction introducing a narrow gate on the p–^{11}B relative energy and on the $\theta_{\rm cm}$ parameter (Lamia *et al* 2012a). The subscript 0 is used to mark the events where the emitted alpha particle leaves ^{8}Be in its ground state. Experimental data are reported as full circles and open squares. The experimental momentum distribution is compared with the expected theoretical shape, given by the square of Fourier transform of the radial bound-state wave function for the x–s system in the PWA approach. In the case of the deuteron, the theoretical distribution is given in terms of the squared Hulthén wave function in momentum space:

$$\varphi_a\left(\boldsymbol{p}_{sx}\right)=\frac{1}{\pi}\sqrt{\frac{ab(a+b)}{(a-b)^2}}\left[\frac{1}{a^2+\boldsymbol{p}_{sx}^2}-\frac{1}{b^2+\boldsymbol{p}_{sx}^2}\right], \qquad (4.4)$$

with parameters $a = 0.2317\,\text{fm}^{-1}$ and $b = 1.202\,\text{fm}^{-1}$ for the deuteron. The squared Hulthén function in momentum space is superimposed onto the data (red dotted line). The two parameters characterizing the Hulthén momentum distribution are determined by the deuteron mass, binding energy and triplet effective range parameter. If a and b are left free to vary, to get a best-fit curve, the black line in figure 18 is obtained that is in very good agreement with the theoretical expression within the experimental uncertainties. In particular, the experimental full-width at half-maximum (FWHM) is $65 \pm 10\,\text{MeV}/c$, in good agreement with the theoretical value of $58\,\text{MeV}/c$. In figure 19 the PWA momentum distribution is replaced by the one evaluated using a DWBA calculation performed by means of the FRESCO code (Thompson 1988), taking the optical model potential parameters from Perey and Perey (1976). The single free parameter, i.e. the normalization factor, is obtained by scaling the calculated distribution to the experimental one. The agreement between PWA and DWBA is very good for the neutron momenta $|\boldsymbol{p}_{sx}| < 30\,\text{MeV}/c$, that is, within the validity interval of the pole approximation, while for larger momenta the PWA function departs from the DWBA curve. This is a well-known result, as a number of works has proved that the shape of the momentum distribution close to the $|\boldsymbol{p}_{sx}| = 0\,\text{MeV}/c$ condition is quite insensitive to the theoretical framework used for its derivation. Also the influence of the d-state component of the deuteron wave function is absolutely negligible in such a momentum window (Lamia *et al* 2012b). Figures 18 and 19 clearly show this effect for $|\boldsymbol{p}_{sx}| < 30\,\text{MeV}/c$ (vertical dotted–dashed line) as the different curves (fit, Hulthén and DWBA) depart from one another by few percent.

Equations (2.75) and (2.79), used in the derivation of the physical parameters, allow us to fully account for the HOES character of the binary sub-process. Such effects are treated only in approximate way when equation (4.1) is used in the derivation of the $A + x \rightarrow b + B$cross section. In detail, since equation (4.1) derives from the application of the impulse approximation, good agreement is found if the momentum transfer, defined by the Galilean

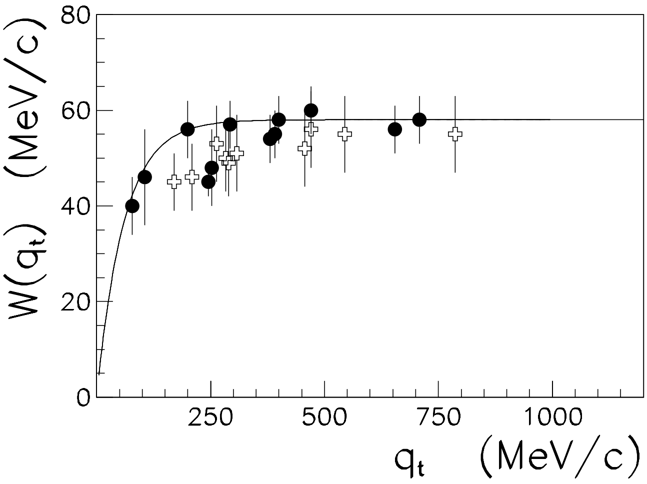

Figure 20. Behavior of FWHM for the p–n momentum distribution as a function of the transferred momentum q_t. The FWHM is deduced from the experimental p–n momentum distribution, while the q_t value is calculated from the reaction kinematics. Open symbols are used for the experimental data in Margaziotis *et al* (1970), Valkovic *et al* (1971), Pan *et al* (1970), Lambert *et al* (1982). Black circles marks the FWHM determined from p–n momentum distributions measured with THM under different kinematical conditions, as listed in table II of Pizzone *et al* (2009). The line represents an empirical fit described in Pizzone *et al* (2009).

invariant equation (Pizzone *et al* 2009)

$$q_t = \left(\frac{m_F}{m_A}\right)^{1/2} p_A - \left(\frac{m_A}{m_F}\right)^{1/2} p_F, \qquad (4.5)$$

is large enough to make distortions negligible (Pizzone *et al* 2005, 2009). However, even in those cases when the momentum transfer is small, so that the impulse approximation requirements are not wholly fulfilled, equation (4.1) still holds but the momentum distribution $|\varphi_a(p_{sx})|^2$ does not match the theoretical one, given by the squared Fourier transform of the x–s relative motion wave function inside a (Pizzone *et al* 2005, 2009). For instance, in the case of the ^{11}B + d → $\alpha +^8$Be + n reaction, the incident ^{11}B energy is 27 MeV and the transferred momentum corresponding to the QF condition is 370 MeV/c, leading to an experimental FWHM that matches the value characterizing the Hulthén function, which can be regarded as the asymptotic value achieved only for large transferred momenta. This is clearly presented in figure 20, where the trend of the experimentally measured FWHM of the deuteron momentum distribution as a function of the transferred momentum is displayed.

In general, the experimental momentum distribution FWHM departs from the theoretical value because of deviations from the simple PWA; anyway, these effects can be accounted for by using the experimental momentum distribution to extract the HOES cross section of the $x + A \to b + B$ sub reaction, with the correct width for the transfer momentum characterizing the TH reaction under investigation. However, within the $p_{sx} < \kappa^a_{sx}$ interval the change of FWHM has a small influence on the THM astrophysical factor. For instance, in the case of the ^{6}Li(^{6}Li,$\alpha\alpha$)^{4}He reaction used to determine the ^{6}Li(d,α)^{4}He cross section (Pizzone *et al* 2005), the $S(E)$ factor undergoes a variation of about 6% by changing the width with respect to the theoretical value, which for ^{6}Li $= \alpha$d equals 73 MeV/c, well below other sources of error such as the statistical uncertainty. Therefore, there is no need to use sophisticated momentum distributions, computed using advanced s–x wave functions, to deduce the astrophysical factor using the THM, as the effect is usually of the order of few percent. In this respect, the dependence on the choice of the momentum distribution has been analyzed in depth in the deuteron case, as the deuteron has been adopted very often as TH-nucleus. In detail, the Hulthén wave function is usually used to describe deuteron s-state wave function, while the d-state component is usually neglected for THM application as it amounts to about 4% of the total deuteron ground-state wave function. However, if is used to extract the THM astrophysical factor, its effect is absolutely negligible. For instance, in the case of the ^{11}B(p,α)^{8}Be reaction measured using the ^{2}H(^{11}B, α_0^8Be)n process, the change in the S-factor is smaller than 1% even taking $p_{sx} < 50$ MeV/c in the data reduction. This is because the maximum of the d-wave contribution lies at $r \sim 2$ fm, thus having its maximum corresponding to $p_{xs} \sim 100$ MeV/c. Such a value is large if compared with the usual THM momentum window (see Lamia *et al* (2012b) for a detailed discussion).

Indirect methods aim at deducing the cross section of a reaction by investigating another process, whose cross section can be linked to the one of interest. Validity tests are necessary to check experimentally whether the hypotheses underlying the equations reviewed in the previous sections can be applied. To this purpose, the indirect angular distributions are compared with the ones for direct reactions, where available, as well as the excitation functions above the Coulomb barrier, where HOES effects are smaller. Figures 21 and 22 show the THM angular distributions for the ^{11}B(p, α_0)^{8}Be (Spitaleri *et al* 2004) and the ^{15}N(p,α)^{12}C reactions (La Cognata *et al* 2007), respectively. They are examples of non-resonant and resonant reactions, respectively. Since the HOES nature of the measured cross section has no influence on the angular distributions as they are extracted for fixed energies and in arbitrary units, the THM data are compared with the direct angular distributions in figures 21 and 22. In both cases, the good agreement provides confidence that background mechanisms, such as sequential decay or direct breakup, do not contribute or have been appropriately separated from the QF reaction yield.

Figure 23 shows the HOES cross section for pp scattering (black symbols) superimposed onto the direct cross section, marked by a black line (Tumino *et al* 2007, 2008). The red line stands for the theoretical pp scattering cross section evaluated under HOES conditions. Clearly, good agreement is found between the HOES cross section and the direct (OES) one at energies above the Coulomb barrier, about 0.5 MeV, thus we can conclude that HOES effects are negligible in this region. Below about 500 keV HOES effects cannot be neglected and the THM cross section departs from the direct one, being devoid of the deep minimum it shows owing to the interference between the Coulomb and nuclear scattering amplitudes (Jackson and Blatt 1950, Dombrowski *et al* 1997). Under such simple conditions, pp scattering, it is apparent that

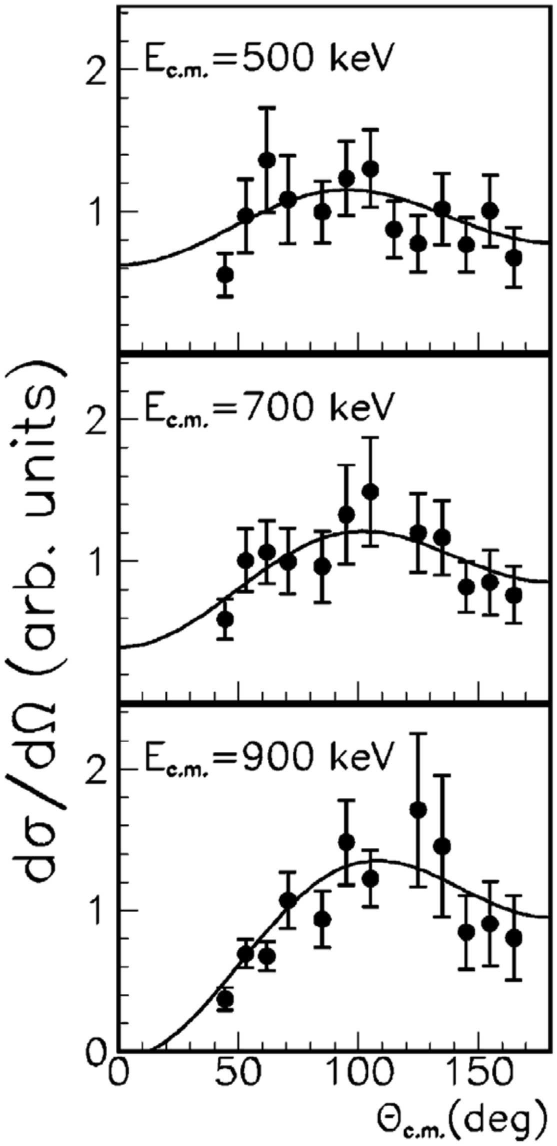

Figure 21. Angular distributions of the ^{11}B(p, α_0)^{8}Be reaction extracted for fixed energies indicated in the figure using the THM (Spitaleri *et al* 2004). For each energy, the black line shows the behavior of the experimental angular distributions from direct measurement, as parametrized by the authors using Legendre polynomials (Becker *et al* 1987).

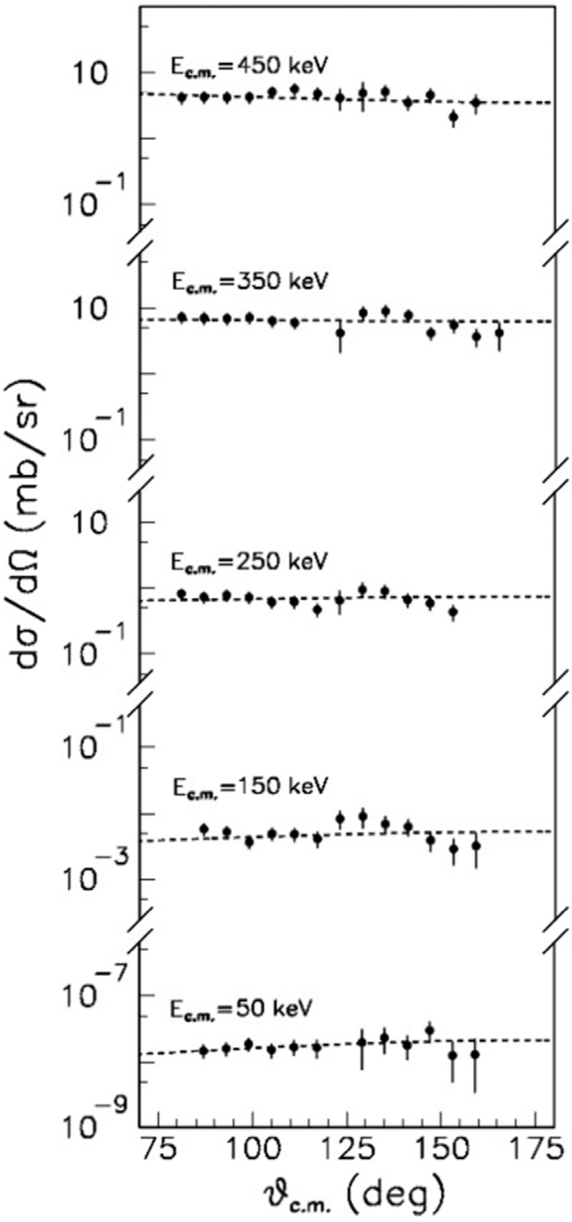

Figure 22. Angular distributions of the ^{15}N(p,α)^{12}C reaction extracted using the THM for indicated energies (La Cognata *et al* 2007). For each energy, a dashed line is used to indicate the corresponding angular distributions from Redder *et al* (1982).

THM essentially probes the nuclear cross section. This can be understood using equations (2.75) and (2.79), which shows that the Coulomb barrier penetration factor is compensated for by the $P_l^{-1/2}(k_{xA}, R_{xA})$ factor present in both equations. These considerations led to the use of equation (2.78) to account for HOES effects.

In the PWA framework only the energy behavior of cross sections can be well reproduced, though absolute values significantly depart from the experimental ones (see Spitaleri *et al* (2011) and references therein). DWBA has proved more realistic, though many more parameters are necessary in calculations (for instance, La Cognata *et al* (2010a, 2010b, 2010c)). As far as direct data are available for normalization, smaller model dependence characterizes THM cross sections adopting PWA in data reduction.

When the PWA equation (4.1) was used to deduce the cross section of the astrophysical reaction of interest, normalization to direct data to get the absolute value of the two-body cross section and thus of the astrophysical S-factor was performed by scaling the THM cross section to direct data above the Coulomb barrier, where HOES effects and the electron screening enhancement are negligible (as shown in figure 23). To minimize the normalization error, the trends of THM and direct data were compared over an energy range as broad as possible, where several direct data sets are available to reduce the effect of systematic uncertainties affecting a single data set. When more partial waves contribute to the total cross section, normalization constants are necessary for each partial wave contribution (see, for instance, the procedure described in Tumino *et al* (2003, 2011), Lamia *et al* (2012a)), as it

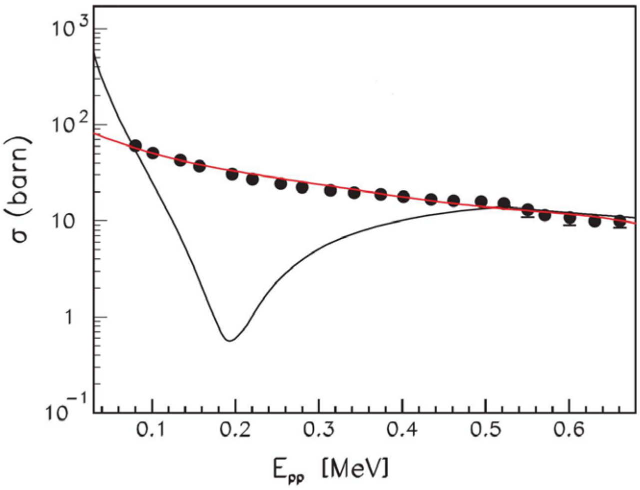

Figure 23. pp scattering cross section above and below the Coulomb barrier (500 keV). Black circles are used for the THM experimental data (Tumino *et al* 2007, 2008). The black line is the free p–p cross section, calculated using the formalism reported in Jackson and Blatt (1950) with scattering length $a_p = -7.806$ fm and effective radius $r_0 = 2.794$ fm. Finally, the theoretical HOES cross section is shown as a red line (Tumino *et al* 2007, 2008). The clear disagreement between the THM data and the free p–p cross section is explained by the suppression of the Coulomb barrier in THM data, which is accounted for in the theoretical HOES cross section.

descends from the considerations in the theoretical section. This procedure is effective when a few partial waves contribute and it is not viable when, for instance, several resonances show up, each populated in a different l-wave, since in this case a normalization performed at high energies could not be attributed to low-energy resonances.

In the case of multi-resonant reactions, a different approach has been developed in the last years to account for HOES effects and get absolute values. Two cases have to be singled out, namely, the narrow and the broad resonance cases. In the narrow resonance case, when the width of the resonance is much smaller than the resonance energy or of the same order, the nuclear parameters of astrophysical interest are resonance strengths and energies, as they only appear in the reaction rate formula. The resonance strength of the ith resonance is defined as (Rolfs and Rodney 1988, Iliadis 2007)

$$(\omega\gamma)_i = \frac{2J_i + 1}{(2J_x + 1)\,(2J_A + 1)}\,\frac{\Gamma^i_{xA}\Gamma^i_{bB}}{\Gamma^i_{\text{tot}}}, \tag{4.6}$$

where J_i, $J_x$andJ_A are the spins of the ith resonance, of nucleus x and A, respectively, and Γ^i_{xA}, Γ^i_{bB} and Γ^i_{tot} the partial widths for the entrance and exit channels and the total width of the ith resonance. The OES and the HOES strength are connected through the following expression (La Cognata *et al* 2008a, 2010a):

$$(\omega\gamma)_i^{\text{THM}} \propto (\omega\gamma)_i^{\text{HOES}}\,\frac{\Gamma^{i\ \text{sp}}_{xA}}{\left(\frac{\text{d}\sigma_{a+A\to F_i+s}}{\text{d}\Omega}\right)_{\text{sp}}}, \tag{4.7}$$

where the denominator, the cross section for the $a+A \to F_i+s$ transfer reaction populating the ith level of the F compound nucleus is necessary to account for the l dependence of the normalization constant, in order to have a single normalization parameter for any number of resonances and l's contributing to the total cross section. The index sp is used to underscore that both $\Gamma^{i\ \text{sp}}_{xA}$ and $(\frac{\text{d}\sigma_{a+A\to F_i+s}}{\text{d}\Omega})_{\text{sp}}$ have to be calculated in the single-particle approach, namely, using shell model wave functions without introducing SFs. Normalization is then achieved choosing a suitable resonance (marked by the index 0), well known from previous studies and measured also in the THM experiment, and scaling the THM resonance strength from equation (4.7) to $(\omega\gamma)_0$:

$$(\omega\gamma)_i^{\text{THM}} = \frac{\Gamma^{i\ \text{sp}}_{xA}}{\left(\frac{\text{d}\sigma_{a+A\to F_i+s}}{\text{d}\Omega}\right)_{\text{sp}}}\,\frac{\left(\frac{\text{d}\sigma_{a+A\to F_0+s}}{\text{d}\Omega}\right)_{\text{sp}}}{\Gamma^{0\ \text{sp}}_{xA}}\,\frac{(\omega\gamma)_i^{\text{HOES}}}{(\omega\gamma)_0^{\text{HOES}}}\,(\omega\gamma)_0\,. \tag{4.8}$$

The double ratio appearing in the previous equation allows for a substantial reduction of the model dependence of the THM resonance strength, leading to very accurate determination of low-energy resonance strengths (La Cognata *et al* 2008a, 2010a and Sergi *et al* 2010).

In the case of broad resonances, the energy dependence of the partial widths cannot be ignored and a more complex approach is necessary. Equation (2.79) is used to fit the 2 → 3 QF cross section, leaving as free parameters the reduced widths of the low-energy resonances, entering the level matrix, whose investigation is the goal of the THM experiment (check La Cognata *et al* (2007, 2009, 2010b, 2011, 2012) about the application of THM to broad resonance reactions). The reduced widths of the known resonances are taken from a standard R-matrix fit of direct data. This is possible as the same reduced widths appear in the R-matrix formula for OES and HOES cross sections (La Cognata *et al* 2011). The reduced widths deduced from the modified R-matrix fit of the 2 → 3 QF cross section using equation (2.79) are then introduced in a standard R-matrix function to infer the energy trend of the astrophysical factor in absolute units inside the Gamow window. Therefore, normalization is relative to observed resonances. This has two important advantages, as normalization is performed by comparison with more than one level and the use of R-matrix allows us to take into consideration not only the $x + A \to b + B$ channel, but all the channels leading to the population of the F compound nucleus resonances covered both in the THM experiment and by direct data. Thanks to this procedure, both the model dependence and the impact of systematic errors affecting direct data are significantly reduced, as the use of a large pool of direct data for normalization minimizes the effect of a biased data set.

4.3.1. Considerations on uncertainties. Apart from statistical error, several sources of uncertainties have to be considered in the evaluation of the THM astrophysical factor, coming from the different stages bringing from the 2 → 3 cross section to the OES one, to be compared with direct data. Background is a primary source of uncertainty. Two different origins should be examined: noise, which can come from electronics, from spurious coincidence events or beam induced background, much the same as in direct measurements, and background from non-QF processes, that is, the occurrence of reaction mechanisms for which the theoretical apparatus we have developed is not a suitable description. This is an additional source of background peculiar of indirect methods and in particular of the THM. Concerning the former, as we have discussed, the use of reactions with three particles in the exit channel makes background subtraction easier than in direct measurements in most of the cases. If the presence of sequential decay processes is ascertained by inspecting, for instance, the experimental momentum distribution, subtraction of the sequential decay mechanism is necessary as this process might be dominant in the phase space under examination. In the case of the ^{3}He(d,p)^{4}He reaction measured by applying the THM to the ^{6}Li(^{3}He,p^{4}He)^{4}He reaction (La Cognata *et al* 2005), the population of ^{8}Be states (in particular the 2$^+$ level at 3 MeV excitation energy) was much more likely than decay through the ^{5}Li level of astrophysical importance (at 16.87 MeV). The rejection of the dominant $^8\text{Be} \rightarrow 2\alpha$ sequential decay implied an additional uncertainty on the ^{3}He(d,p)^{4}He S-factor ranging from 10% to 20%, the largest value corresponding to the lowest energy region where the SD contribution dominates.

The theoretical framework adopted in the data analysis introduces additional uncertainties through the approximations exploited to express the cross section of the $2 \rightarrow 3$ reaction as a function of the cross section of the binary sub-reaction. For instance, equations (2.75) and (2.79) were derived assuming that the PWA holds, while a more realistic approach such as the DWBA would be advisable. This is possible if distorted waves are introduced in equations (2.74) and (2.75) in the place of the plane wave of the relative motion of particles i and j, $\chi_{ij}^{(0)}$. This has been performed in several cases to evaluate the contribution of systematic uncertainties. For instance, in the case of the ^{13}C(α,n)^{16}O reaction studied using the ^{13}C(^{6}Li,n^{16}O)d THM reaction (La Cognata *et al* 2012, 2013), the THM cross section is dominated above 500 keV by two resonances at 806 keV and 1019 keV. Their relative strength has been estimated in the PWA and DWBA models, taking optical model potential parameters from Johnson *et al* (2006). The DWBA and PWA calculations coincide within 9%, well within normalization and statistical errors (La Cognata *et al* 2012, 2013). Similarly, the change in the channel radius R_{xA}, a free parameter entering the modified R-matrix calculation (equations (2.97) and (2.108)), is responsible of a change of a few percent of the zero-energy astrophysical factor of the binary sub-reaction, provided that the channel radius is modified within reasonable values (for instance, ±1 fm) (La Cognata *et al* 2007). Note that to check the validity of the PWA the initial and final state interactions were also taken into account (La Cognata *et al* 2010a, 2010b, 2010c, 2011, Gulino 2013).

The largest source of uncertainty in THM experiments should be usually attributed to normalization to direct data, even though different normalization procedures have been devised in the attempt to reduce its contribution to the total uncertainty. As discussed above, usually THM data are scaled to direct data inside a broad energy range or to known resonances. In any case, we attempt to collect as many data sets as possible, or we try to cover an energy window where more than a single data set is available, since averaging out over a pool of direct data sets makes the influence of a single biased data set less relevant. However, normalization uncertainties ranging between 10% and 20% are usually found owing to a mismatch between different data sets or to their statistical uncertainties. By introducing a DWBA formulation of THM we aim to remove the need to scale THM data to direct data, which is especially important for the application of THM to reactions induced by unstable nuclei, as direct data are often missing or characterized by very large errors.

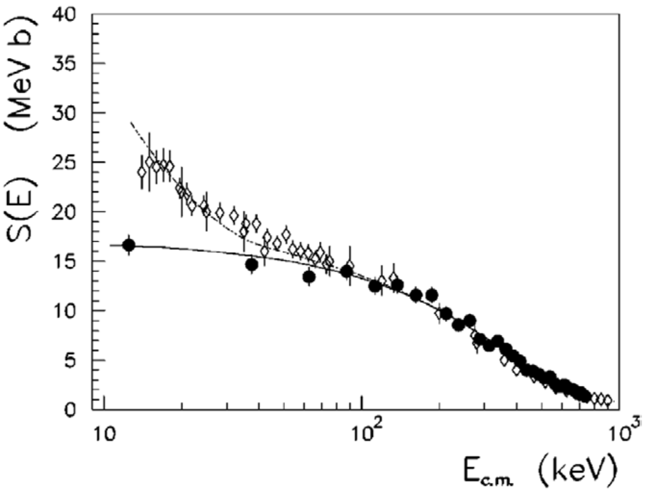

Figure 24. The $S(E)$ factor of the ^{6}Li(d,α)α reaction extracted with the THM (Spitaleri *et al* 2001) (full dots) is compared with direct data from Engstler *et al* (1992a) (open symbols); a fit to the indirect data with a second-order polynomial is shown as a solid line. The fit to determine U_e is also shown (dotted line).

4.4. Electron screening effects

Once the OES S-factor has been extracted, its comparison with direct data usually shows good agreement down to a center-of-mass energy where the presence of electrons cannot be neglected. Indeed, atomic electrons shield nuclear electric charges, causing an artificial increase of the measured astrophysical factor at low energies due to a reduced Coulomb repulsion (Assenbaum *et al* 1987, Rolfs and Rodney 1988, Balantekin *et al* 1997, Strieder *et al* 2001). This is clearly apparent in figure 24. Down to about 100 keV, the THM S-factor of the ^{6}Li(d,α)α reaction (filled circles) perfectly matches the direct one (empty symbols). The two data sets depart from one another below 100 keV, as the THM S-factor (Spitaleri *et al* 2001) is not affected by electron screening enhancement while direct data are (Engstler *et al* 1992a).

The ^{6}Li(d,α)α reaction has been extensively measured in the past, using both the THM and direct approaches, for several reasons, besides nuclear astrophysics (where it occurs in the pre-main sequence and in the inhomogeneous Big Bang nucleosynthesis (Pizzone *et al* (2011) and references therein)). In the THM framework, it has been measured for checking the TH particle invariance, the influence of a charged spectator on the extracted binary cross section and the projectile breakup–target breakup invariance. Moreover, it has been used to evaluate the isotopic independence of the electron screening potential, by comparing the deduced electron screening potential with those for the ^{7}Li(p,α)α and ^{6}Li(p,α)^{3}He processes. Very good agreement was found between the $S(0)$ value extrapolated from high-energy direct data, $S(0) = 17.4$ MeV b (Engstler *et al* 1992a), and the value obtained through the THM, free of electron screening and not extrapolated, $S(0) = 16.9 \pm 0.5$ MeV b (Spitaleri *et al* 2001).

The fact that THM can provide for electron-screening free astrophysical factor has two major consequences. One is that since electron screening acts differently in stars and in the laboratory, the S-factor from direct data has to be corrected two times as the laboratory screening has to be removed and the plasma screening factor has to be accounted for. THM instead supplies the bare-nucleus S-factor, thus only the plasma screening factor (Rolfs and Rodney 1988) has to be introduced for astrophysical applications making it possible to reduce systematic uncertainties related to electron screening corrections. This is even more important as we presently have an incomplete understanding of the electron screening effect; the enhancement, as predicted by models, usually underestimates the experimental value evaluated by comparing the experimental S-factor with the bare nucleus one (see La Cognata *et al* (2005) for the ^{3}He(d,p)^{4}He case and references therein).

The second important consequence is the possibility to deduce the electron screening potential U_e by using the THM S-factor as that appropriate for a bare nucleus. In the standard approach, the bare nucleus astrophysical factor $S_{\mathrm{bare}}(E_{\mathrm{cm}})$ is obtained by extrapolating the direct S-factor from high energies, where the enhancement is negligible, down to zero energy. Then the electron screening potential is deduced by fitting direct data through the formula (Rolfs and Rodney 1988):

$$S(E_{\mathrm{cm}}) = S_{\mathrm{bare}}(E_{\mathrm{cm}})\ \exp\left(\pi\eta\frac{U_e}{E_{\mathrm{cm}}}\right). \qquad (4.9)$$

As we have already discussed, extrapolation might introduce systematic errors due to, for instance, the presence of sub-threshold resonances determining an increase of the astrophysical factor at low energies, in the same way as electron screening (La Cognata *et al* 2012, 2013). The use of THM to provide for $S_{\mathrm{bare}}(E_{\mathrm{cm}})$ might help to reduce uncertainties on U_e and, therefore, to improve our current understanding of electron screening. This approach is exemplified in figure 24 where the THM data are parameterized using a second-order polynomial (full line), thus obtaining $S_{\mathrm{bare}}(E_{\mathrm{cm}})$, which is the input in equation (4.9) that is used to fit direct data (dotted line). In the case of the ^{6}Li(d,α)α reaction, $U_e = 340 \pm 51$ eV is obtained (Spitaleri *et al* 2001), in agreement with the results in the literature (Engstler *et al* 1992a) (350 eV) but much larger than 186 eV, that is, the upper limit for U_e predicted by the adiabatic approximation (Bracci *et al* 1990).

4.5. Experimental THM applications to non-resonant reactions

As an example of the THM used for direct reactions, consider the case of ^{7}Li abundance, which is a key isotope in astrophysics as its abundance is a signature of the nucleosynthesis process that took place during the Big Bang and still occurs in stars (Fields 2011). Indeed, the Big Bang essentially produced light nuclei up to ^{7}Li, because of the absence of stable $A = 8$ nuclei. Primordial ^{7}Li abundances can be retrieved by observing very old stars, formed from material closely resembling the ashes of primordial nucleosynthesis (Meléndez *et al* 2010). However, when comparing ^{7}Li abundance with model predictions, based on the WMAP measurement of the baryon-to-photon ratio η (Dunkley *et al* 2009), it turns out that theoretical evaluations overestimate ^{7}Li pristine abundance (Fields 2011). This mismatch might be linked to ^{7}Li stellar processing; due to mixing affecting star outer layers, ^{7}Li on a star surface might be brought to high-temperature regions where ^{7}Li is burnt through the ^{7}Li(p,α)^{4}He reaction. Therefore, if ^{7}Li primordial abundance was well known, the measured abundance could be used to constrain mixing model, working as a probe of star inner layers (Lamia *et al* (2012c) and references therein).

Table 7. Zero-energy astrophysical factor $S(0)$ of the ^{7}Li(p,α)^{4}He reaction obtained through extrapolation from high-energy direct data and by means of the THM.

$S(0)$ (keV b)	Ref.	Method
52 ± 8	Rolfs and Kavanagh (1986)	Extrapolation
59.3	Engstler *et al* (1992a)	Extrapolation
55 ± 3	Spitaleri *et al* (1999), Lattuada *et al* (2001)	THM
$55.6^{0.8}_{-1.7}$	Cruz *et al* (2008)	R-matrix
58	Barker (2000)	R-matrix
60–66.2	Barker (2002)	R-matrix
59.3	Angulo *et al* (1999)	Compilation
52 ± 11	Xu *et al* (2013)	Compilation

In this context, the ^{7}Li(p,α)^{4}He reaction plays a key role, especially at energies of <10 keV typical of the bottom of the convective region (Lamia *et al* 2012c). Table 7 displays the zero-energy astrophysical factor reported by different authors, showing a broad range of extrapolated values. In fact, direct measurements cannot access the energy region of astrophysical importance, thus extrapolations are necessary to spread over the Gamow window. These have been performed using both simple polynomial fitting of high-energy data (Engstler *et al* 1992a, Rolfs and Kavenagh 1986) and the more accurate R-matrix approach (Cruz *et al* 2008, Barker 2000, 2002), allowing one to account for all the levels contributing to the astrophysical factor. Compilations have collected these results to supply a best estimate of $S(0)$ for astrophysical applications (Angulo *et al* 1999).

Direct data from Engstler *et al* (1992a) are shown in figure 25 as open symbols. They clearly demonstrate the effect of electron screening as the astrophysical factor undergoes a steep increase below ~100 keV. As already discussed, our current limited understanding of the effect of electron clouds on fusion reactions might introduce systematic uncertainties right at astrophysical energies. For this reason, the ^{7}Li(p,α)^{4}He reaction was investigated by means of the THM, selecting the QF yield from the measured ^{2}H(^{7}Li,$\alpha\alpha$)n cross section. The bare-nucleus $S(E)$-factor was extracted in the energy range

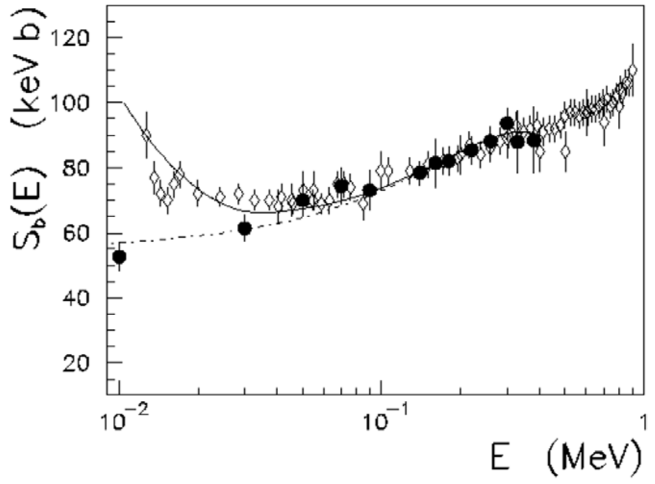

Figure 25. ^{7}Li(p,α)α $S(E)$ factor extracted using the THM (Lattuada *et al* 2001) (full dots), compared with direct data from Engstler *et al* (1992a) (open symbols); a fit to the indirect data with a second-order polynomial is shown as a dotted–dashed line. The fit to determine U_e is also displayed (full line).

$E_{cm} = 10 - 300$ keV and normalized to direct data in Engstler *et al* (1992a). THM data are superimposed on the direct S-factor in figure 25 (black circles). Good agreement is found above $E_{cm} \sim 100$ keV, where the effect of electron screening is negligible, while at low energies THM data departs from the direct ones that are affected by the electron shielding. $S^{THM}(0)$ was deduced by fitting THM data with a polynomial. Since the THM S-factor reaches 10 keV and it is devoid of electron screening effects, $S^{THM}(0)$ can be determined with a much better accuracy, leading to $S^{THM}(0) = 55 \pm 3$ keV b (table7). The fitting curve used to determine $S^{THM}(0)$ is visible in figure 25 as a dotted–dashed line.

The interpolated THM S-factor (dotted–dashed line in figure 25) was introduced into equation (4.9) as it represents the bare-nucleus astrophysical factor $S_{bare}(E_{cm})$; then, equation (4.9) was used to fit direct data to determine the electron screening potential $U_e = 330 \pm 40$ eV (Lamia *et al* 2012a). This result matches the U_e parameter deduced taking as $S_{bare}(E_{cm})$ the extrapolated astrophysical factor, $U_e = 300 \pm 160$ eV (Engstler *et al* 1992a). The advantage of the THM approach is that the uncertainty on the electron screening potential is reduced by a factor 2 to 4 with respect to that obtained from direct measurements (Engstler *et al* 1992a). This is linked to the reduced uncertainty affecting the THM bare-nucleus S-factor. The THM measurement confirms the disagreement of the experimental U_e values and the upper limit of 175 eV set by the adiabatic limit. The electron screening potential obtained from the comparison between THM and direct data is compared with other results in the literature collated in table 8.

Another example is boron abundance, which is a probe of the internal stellar structure, as it allows us to evaluate to what depth mixing extends, in a way similar to what we have briefly mentioned about lithium (Boesgaard 2004). In particular, boron isotopes, ^{11}B (<80%) and ^{10}B (<20%), are mainly destroyed via (p,α) reactions at temperatures of $\sim 5 \times 10^6$ K, corresponding to energies of a few keV (Lamia *et al* 2012a, 2012b, 2012c). The burning cross sections have to be known with good accuracy to implement accurate models of mixing.

Table 8. Summary of the electron screening potentials U_e reported in the literature, obtained from the investigation of the ^{7}Li(p,α)α reaction, compared with the THM value. For reference, the adiabatic limit yields an upper limit $U_e = 175$ eV.

U_e (eV)	Ref.	Method
300 ± 280	Engstler *et al* (1992b)	Extrapolation
300 ± 160	Engstler *et al* (1992b)	Extrapolation
330 ± 40	Lattuada *et al* (2001)	THM
237^{133}_{-77}	Cruz *et al* (2008)	R-matrix
242	Barker (2002)	R-matrix
155	Barker (2002)	R-matrix
300	Engstler *et al* (1992a)	Compilation
245 ± 45	Cyburt (2004)	Compilation

The ^{11}B(p,α)^{8}Be S-factor has been measured from $E_{cm} = 18.73$ keV up to $E_{cm} > 1$ MeV (Segel *et al* 1965, Davidson *et al* 1979, Becker *et al* 1987, Angulo *et al* 1993). However, such measurements do not cover the energy region of interest for astrophysics, the Gamow peak lying at about 10 keV. This energy is much lower than the ^{11}B–p Coulomb barrier, about 1.7 MeV, thus the cross section is vanishingly small and the bare-nucleus astrophysical factor $S_b(0)$ of the ^{11}B(p,α)^{8}Be reaction was obtained through extrapolation from high-energy direct data.

Below 1 MeV, the ^{11}B(p,α)^{8}Be astrophysical factor is characterized by a broad resonance at about 600 keV, due to the 16.57 MeV, $J^\pi = 2^-$ ^{12}C state and by a sharp resonance at about 150 keV, corresponding to the 16.106 MeV level of ^{12}C ($J^\pi = 2^+$, $\Gamma = 5.2 \pm 0.3$ keV) (Lamia *et al* (2012a) and references therein). In the ^{11}B(p,α)^{8}Be reaction the emitted α-particle mostly leaves ^{8}Be in its first excited state, thus α_1 is the main reaction channel, about 100 times more likely than the α_0 one. In the case of ^{11}B(p,α_0)^{8}Be the $S(E)$-factor shows the presence of the 150 keV peak (fed in p-wave) superimposed onto an s-wave non-resonant contribution while the 600 keV level cannot contribute due to its J^π value.

Below about 100 keV, the presence of atomic electrons cannot be neglected as it determines an enhancement of the astrophysical factor and electron screening has to be accounted for in the extrapolation. The extrapolated zero-energy astrophysical factors are $S(0) = 2.1$ MeV b (α_0 channel) and $S(0) = 195$ MeV b (α_1 channel) (Angulo *et al* 1993). By comparing the extrapolated S-factor with the screened one, an electron screening potential $U_e = 430 \pm 80$ eV was found. Such a value is higher than the upper limit provided by the adiabatic model of 340 eV (Angulo *et al* 1993), confirming the systematic discrepancy between experimental and theoretical values for the electron screening potential. The origin of the discrepancy can be traced back both to the trend of low-energy direct data or to extrapolation. The THM approach allows us to determine the trend of the bare-nucleus astrophysical factor down to zero energy, making it possible to independently extract the electron screening potential and the ^{11}B(p,α)^{8}Be reaction rate for astrophysical application.

To extract the ^{11}B + p $\rightarrow \alpha_0 +^8$ Be reaction cross section, two measurements of the QF ^{2}H(^{11}B, α_0^8Be)nreaction were

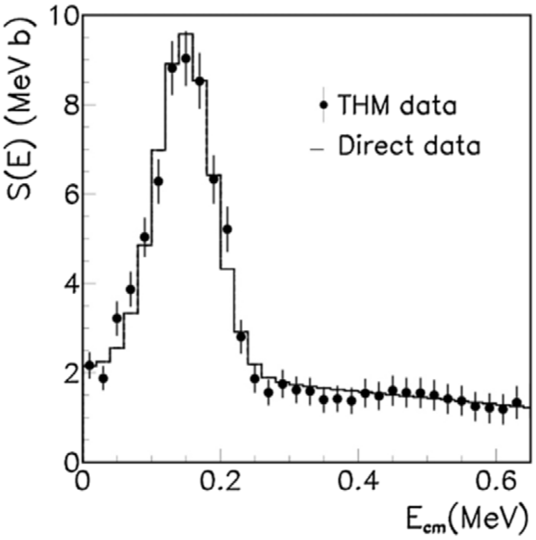

Figure 26. Comparison of the THM ^{11}B(p,α_0)^{8}Be astrophysical factor (full circles) (Lamia *et al* 2012a) with the direct one (Becker *et al* 1987), shown as an histogram, smeared to match the THM data energy resolution.

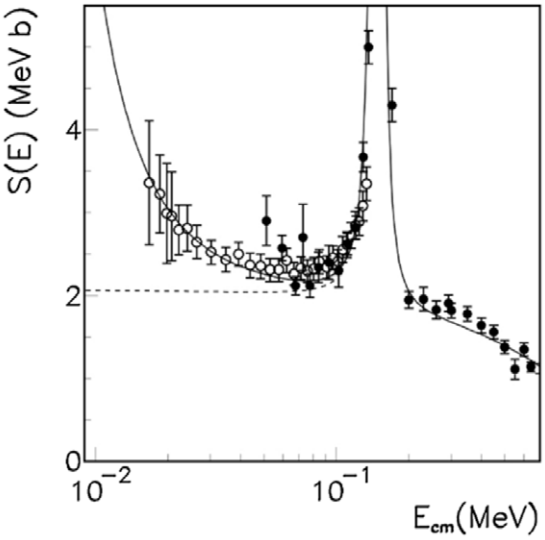

Figure 27. Direct data for the α_1 channel (Angulo *et al* 1993), scaled to match the $\alpha_0 S$-factor (open circles), for the α_0 channel (filled circles) (Becker *et al* 1987) and THM direct contribution (dotted line) (Lamia *et al* 2012a). The solid line is the fit of screened direct data using equation (4.9), where we have taken for S_{bare} the THM direct contribution (dotted line).

carried out via the THM (Spitaleri *et al* 2004, Lamia *et al* 2012a). Both experiments were performed at the Laboratori Nazionali del Sud of Catania (Italy) by using the SMP Tandem Van de Graaf accelerator supplying a 27 MeV^{11}B beam. The detection setup consisted of one dual position sensitive detector (DPSD) and standard, charge-partition, PSDs. Due to its instability against α-decay and the short lifetime (about 10^{-18} s), the ground state of ^{8}Be was selected by reconstructing the relative energies between two alpha particles hitting in coincidence the upper and lower part of the DPSD. The trigger for the event acquisition was given by the triple coincidences between the upper and lower part of the DPSD and one of the three PSDs. This unequivocally led to the identification of the ^{2}H(^{11}B, α_0^8Be)n channel. The second experiment was performed to improve the previous study in the astrophysical region. We focused on the α_0 channel, though it is less favored than the α_1, since the detection efficiency for the latter in the THM measurement strongly suppressed the reaction yield.

Figure 26 shows the extracted S-factor (Lamia *et al* 2012a) (black symbols) superimposed on the direct one (Becker *et al* 1987), smeared to match the THM energy resolution (~100 keV FWHM) and displayed as a histogram. Since two partial waves contribute to the total S-factor, $l = 0$ for the non-resonant part and $l = 1$ for the 150 keV resonance, two normalization constants were necessary to attain the THM astrophysical factor in absolute units. These were deduced by equaling the areas subtended by the 150 keV peak in direct and indirect data for the p-wave contribution, and by scaling the indirect data to the direct ones in the 400–600 keV energy range for the non-resonance contribution. The resulting $S(E)$ agrees very well with the data in the literature (figure 26). The non-resonant part, which is the most important component at astrophysical energies, could then be established and in particular the zero-energy S-factor, 2.07±0.41 MeV b (Lamia *et al* 2012a), is fairly consistent with the extrapolated value of 2.1 MeV b found by Becker *et al* (1987).

The low-energy trend was used to assess the electron screening potential U_e by comparing direct data with the THM S-factor below ~100 keV. However, direct data have poor coverage in this region for the α_0 channel, while the ^{11}B(p,α_1)^{8}Be S-factor has been measured with good accuracy down to ~19 keV (Angulo *et al* 1993). Therefore, the S-factor for the α_1 channel (empty circles in figure 27) has been scaled to match the astrophysical factor of the ^{11}B(p,α_0)^{8}Be reaction (filled circles in figure 27). The electron screening potential was then deduced by fitting the scaled S-factor using equation (4.9), where we assumed the direct component of the THM astrophysical factor (dotted line in figure 27) as the bare-nucleus S-factor. $U_e = 472 \pm 160$ eV (Lamia *et al* 2012a) was then obtained, in good agreement with 430±80 eV, deduced using as bare-nucleus S-factor the extrapolation from higher energies (Angulo *et al* 1993), and overlapping with the upper limit of 340 eV predicted by the adiabatic approximation (Angulo *et al* 1993) because of the large error bar. Even though uncertainties are large, the derived U_e suggests a possible departure from the adiabatic limit, confirming once again the systematic discrepancy between experimental and theoretical values for the electron screening potential.

4.6. THM applications to resonant reactions

Two examples are provided here to show how the THM can be used to study reaction rates that are dominated by low-energy resonances. The abundance of ^{19}F is very important in the Asymptotic Giant Branch (AGB) stage of stellar evolution, which represents the final nucleosynthesis phase for low- and intermediate-mass stars (Herwig 2005). AGB stars play an extremely important role in astrophysics as possible site for stable-, heavy-element production in their interiors through slow-neutron captures (s-process) (Busso *et al* 1999). The

Table 9. Summary of the $S(0)$ factors of the $^{15}N(p,\alpha)^{12}C$ reaction deduced by different authors, compared with the THM results.

$S(0)$ (MeV b)	Ref.	Method
64	Schardt *et al* (1952)	Breit–Wigner extrapolation
78 ± 6	Zyskind and Parker (1979)	Breit–Wigner extrapolation
65 ± 4	Redder *et al* (1982)	Breit–Wigner extrapolation
68 ± 11	La Cognata *et al* (2007)	THM
70 ± 14	La Cognata *et al* (2009)	THM
73 ± 5	La Cognata *et al* (2009)	R-matrix
80	Barker (2008)	R-matrix
65 ± 7	Angulo *et al* (1999)	Compilation
67.5 ± 4	Adelberger *et al* (2011)	Compilation
67 ± 14	Xu *et al* (2013)	Compilation

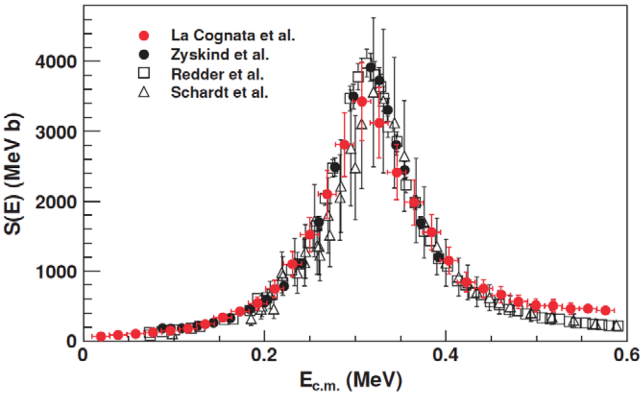

Figure 28. Comparison of the THM $^{15}N(p,\alpha)^{12}C$ astrophysical factor (red circles) with the direct ones, shown as black symbols (black circles (Zyskind and Parker 1979), empty squares (Redder *et al* 1982) and empty triangles (Schardt *et al* 1952)).

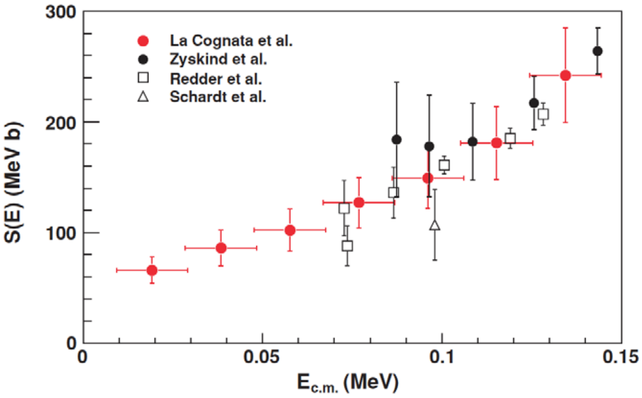

Figure 29. Same as the previous figure, but only the low-energy tail is shown to emphasize the scatter of direct data at low energies.

abundance of ^{19}F is very sensitive to the internal stellar structure and therefore provides a key parameter to constrain AGB-star models, and ultimately the s-process (Lugaro *et al* 2004). However, when theoretical abundances are compared to observed ones, remarkable discrepancies (up to one order of magnitude) emerge, revealing a poor understanding of the physical conditions under which ^{19}F is synthesized (Jorissen *et al* 1992, Abia *et al* 2010, 2011, Lucatello *et al* 2011). Thus, the study of the nuclear reactions involved in the production and destruction of ^{19}F is of critical importance. The $^{15}N(p,\alpha)^{12}C$ reaction removes both ^{15}N and protons from the ^{19}F production chain in AGB stars. The reaction is also a key CNO cycle reaction as it marks the branching between the CN and NO cycles. However, the available reaction rates yield at least an 8% uncertainty on fluorine surface abundance, due to a difference of a factor of 2 between the NACRE (Angulo *et al* 1999) and CF88 (Coughlan and Fowler 1988) rates usually employed in calculations (La Cognata *et al* 2007).

The cross section has been measured down to 70 keV (Schardt *et al* 1952, Zyskind and Parker 1979, Redder *et al* 1982), while only extrapolations are available at lower energies, which are needed for quiescent CNO burning where the Gamow energy can be as small as 26 keV. Extrapolations were performed using both Breit–Wigner functions and R-matrix calculations. For reference, the extrapolated zero-energy S-factors by different authors are listed in table 9. The results show some dispersion between the different extrapolated values, motivating the THM investigation of the $^{15}N(p,\alpha)^{12}C$ reaction.

The THM experiment was performed at the Cyclotron Institute at Texas A&M University (TX, USA) using a 60 MeV ^{15}N beam impinging onto a deuterated polyethylene target about 100 μg cm^{-2} thick (La Cognata *et al* 2007, 2009). The THM $S(E)$ factor is given in figures 28 and 29 as red full symbols. The astrophysical factor is dominated by a resonance lying at about 300 keV due to the 12.44 MeV ^{16}O state, making it necessary to analyze the THM result using the modified R-matrix approach (equation (2.79)). In the case of a single resonance, normalization is achieved by equaling the areas under the same resonance as it appears in direct and indirect data, thus accounting for energy resolution effects that might introduce differences in the resonance shape owing to possible difference in resolution in direct and indirect measurements. From figures 28 and 29, it is clear that the 312 keV resonance is well reproduced by the THM measurement as well as the low-energy tail, where direct data are available (Schardt *et al* 1952, Zyskind and Parker 1979, Redder *et al* 1982). At energies above about 500 keV, beyond the range of astrophysical importance and of normalization, the THM S-factor deviates from the direct one due to the occurrence of sequential decay processes.

As discussed in the theoretical section, the modified R-matrix approach (equation (2.79)) has been developed to account for the off-shell nature of the transferred participant particle (in this case a proton), to extract the resonance parameters from the THM data and to provide rigorous parameterization of the $S(E)$ factor for reaction rate calculations. By means of the modified R-matrix approach, the THM yielded $S(0) = 70.0 \pm 13.5$, in good agreement with previous extrapolations (table 9). Good agreement between the $S_b(0)$ values from different approaches represents a strong validation of the THM when applied to resonant reactions. Moreover, it is worth noticing that the THM has allowed to significantly reduce the scatter of low-energy S-factor data (figure 29), reducing considerably the uncertainty affecting $S(0)$ as no extrapolation or theoretical estimates are needed.

The second example is the ^{18}O(p,α)^{15}N reaction, which is of primary importance to pin down the uncertainties, due to nuclear physics input, affecting present-day models of AGB stars (Lugaro *et al* 2004). Its reaction rate can modify the fluorine yield due to the peculiar nucleosynthesis inside such stars as well as oxygen and nitrogen isotopic ratios, which allow one to constrain the proposed astrophysical scenarios. Since the internal layers of AGB stars are the environment where the s-process takes place, a more accurate measurement of the ^{18}O(p,α)^{15}N reaction cross section might provide a better understanding of the s-process (Nollett *et al* 2003). A more accurate measurement of the ^{18}O(p,α)^{15}N reaction cross section also might provide a better understanding of the so-called R-Coronae Borealis (RCB) stars (Clayton *et al* 2007, Pandey *et al* 2008). In these stars, peculiar ^{18}O and ^{19}F abundances have been observed, for instance ^{16}O/^{18}O $\leqslant 1$ is found, which is about one hundred times smaller than the Galactic ratio. The ^{18}O(p,α)^{15}N reaction cross section has been the subject of several investigations, including direct and indirect measurements, the latter aiming to determine the resonance parameters (Champagne and Pitt 1986, Wiescher and Kettner 1982, Lorentz-Wirzba *et al* 1979).

Below 1 MeV the cross section is dominated by three resonances at 20, 144 and 656 keV, with the one at the lowest energy being known only through spectroscopic measurements. Indeed, the cross section at 20 keV is about 10^{11} times smaller than the one at 70 keV, which is the lowest measured energy, thus making it impossible to observe the 20 keV peak with present-day facilities. Therefore, an indirect measurement of the low-energy region of the ^{18}O(p,α)^{15}N cross section has been performed by means of the THM to extract the resonance strengths of the 20 and 90 keV resonances (La Cognata *et al* 2008a, 2010a). It is important to note that the low-energy resonances at 20, 90 and 144 keV are narrow (their width being much smaller than the resonance energy), calling for the application of the resonant THM approach.

The cross section of the ^{2}H(^{18}O,α^{15}N)n reaction was measured at the Cyclotron Institute, Texas A&M University (La Cognata *et al* 2008a) and at the Laboratori Nazionali del Sud (Italy) (La Cognata *et al* 2008b, 2010a) using a 54 MeV ^{18}O beam impinging on a CD$_2$ target, 100 μg cm^{-2} thick. The α and ^{15}N nuclei were detected in coincidence in PSDs to determine their relative energy spectra. As a first step in the analysis, angular distributions of the ^{18}O(p,α)^{15}N reaction were extracted to establish the spin parity of the 90 keV resonance and to infer the total cross section from the measured $\frac{d^3\sigma}{d\Omega_b\, d\Omega_B\, dE_b}$ triple differential cross section (2.79). The resulting angular distributions are shown in figure 30 as black symbols, as a function of the p–^{18}O center-of-mass angle, superimposed onto the theoretical angular distribution obtained using standard equations given in Blatt and Biedenharn (1952). For the 20 and 144 keV resonances, for which the spin-parities are well known, we found good agreement between experimental and theoretical angular distributions. In the case of the 90 keV peak, coming from the 8.084 MeV state in ^{19}F, we were able to assess its spin parity to be 3/2$^+$.

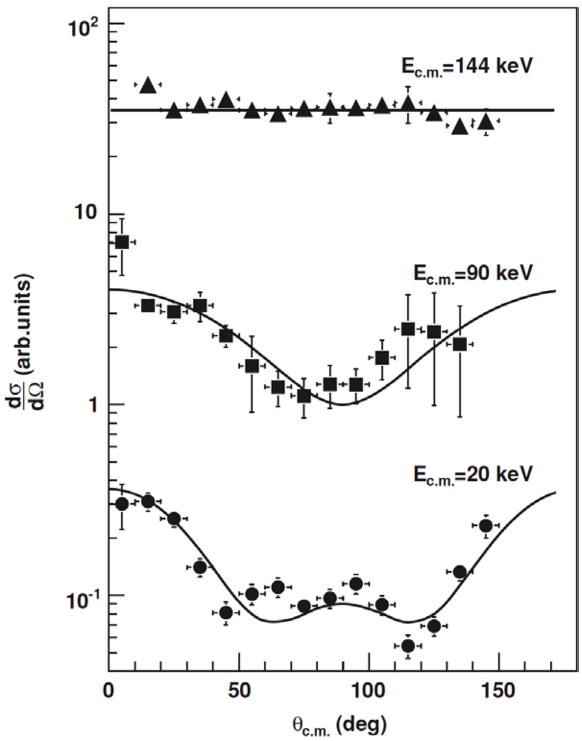

Figure 30. Angular distributions of the ^{18}O(p,α)^{15}N reaction, deduced from the THM reaction yield for the three resonances in the 0–250 keV interval (La Cognata *et al* 2008a, 2010a). The full lines are the theoretical angular distributions for the OES ^{18}O(p,α)^{15}N reaction, calculated according to the equations of Blatt and Biedenharn (1952).

The angle-integrated ^{2}H(^{18}O,α^{15}N)n cross section is shown in figure 31. According to the modified *R*-matrix approach equation (2.79), which can be simplified in the case of narrow resonances, the area under each peak is related to the resonance strength by easily calculable factors (La Cognata *et al* 2010a). Therefore, THM resonance strengths were deduced by fitting the $\frac{d^2\sigma}{d\Omega_n\, dE_{\rm cm}}$ cross section (figure 31) and normalized as discussed in section 4.3 (equation (4.8)). In detail, the strengths of the 20 and 90 keV resonances were scaled to the one of the 144 keV peak, which had been well established in previous experiments (Becker *et al* 1995) to be $(\omega\gamma)_3 = 0.167 \pm 0.012$ eV. The THM leads to $(\omega\gamma)_1 = 8.3^{+3.8}_{-2.6} \times 10^{-19}$ eV for the 20 keV resonance, which is well within the upper and lower limits given by NACRE (Angulo *et al* 1999), $6^{+17}_{-5} \times 10^{-19}$ eV. The THM central value is about 35% larger than the NACRE one, while the uncertainty has been significantly reduced (the upper bound has been lowered by a factor of 4.5) because no SF is needed to evaluate the resonance strength. The largest contribution to the error is due to the uncertainty on the resonance energy, while statistical, systematic, and normalization errors add up to 9.5% (compare Becker *et al* (1995) about the normalization error). The same procedure applied to the 90 keV resonance gives $\omega\gamma = 1.76 \pm 0.33 \times 10^{-7}$ eV, in agreement with the NACRE result, $1.6 \pm 0.5 \times 10^{-7}$ eV, providing for a cross check of the method.

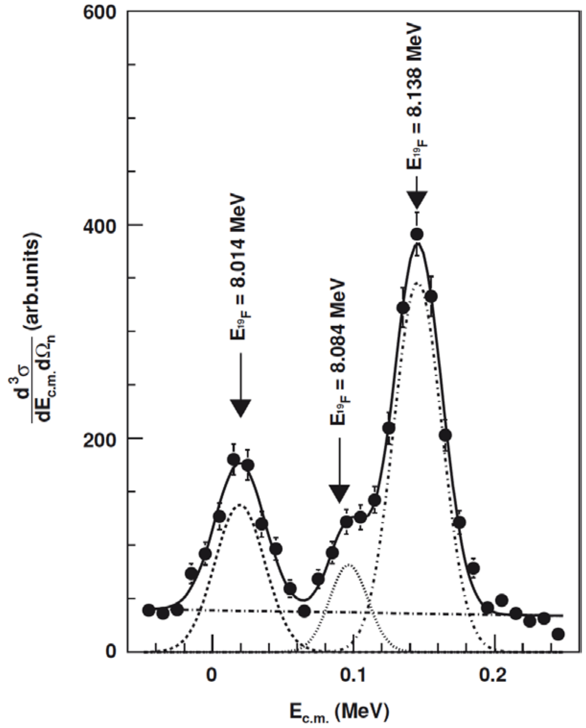

Figure 31. Cross section of the of the TH reaction (full circles) (La Cognata *et al* 2008a, 2010a). The full line represents the result of a fit including three Gaussian curves (short-dashed, dotted, and short-dashed–dotted lines) and a first-order polynomial (long-dashed–dotted line) to take into account the three resonances at 20, 90, and 144 keV and background, respectively. The area subtended by each resonance is proportional to the resonance strength.

4.7. Neutron-induced reactions: the ^{6}Li(n,t)^{4}He process

Neutron-induced reactions play a fundamental role in nuclear astrophysics, in particular in the nucleosynthesis of elements heavier than iron through the s-process or the r-process (Busso *et al* 1999, Käppeler *et al* 1998). However, their measurement is quite complicated because neutron beams are necessary. As an indirect approach, the THM turns out to be very effective since deuterons can act as a virtual neutron source if neutron transfer is selected. Moreover, the THM can be applied also to the investigation of neutron-induced reactions on unstable nuclei, which would be otherwise impossible with present-day facilities. The ^{6}Li(n,α)^{3}H reaction has been chosen to validate the THM in the case of neutron-induced reactions (Tumino *et al* 2005, Gulino *et al* 2010), as direct data are available over a broad energy range, from a few tens of eV up to several MeV (Overley *et al* 1974). At low energies (below ~0.6 keV) the ^{6}Li(n,α)^{3}H cross section is characterized by two contributions, a resonant one due to the formation of the 7.454 MeV 5/2$^-$ ^{7}Li state, leading to a peak at $E_{n^6\mathrm{Li}} = 204$ keV, and a non-resonant contribution showing the typical *1/v* trend of the cross section for slow-neutron capture reactions.

In the experiment (Gulino *et al* 2010), great care was devoted to improve the energy resolution. Beam collimation was carefully implemented, no ΔE detectors were used for particle identification and PSDs were placed at 780 mm from the target. Kinematical conditions were chosen so as to have a very smooth dependence of the α–t relative energy on α and t kinematic energies. Under such assumptions, the contribution to the α–t relative energy resolution due to PSD energy resolution is further reduced (‘magnifying glass’ effect (Baur *et al* 1986)). Taking into account all of the experimental uncertainties, the energy $E_{n^6\mathrm{Li}}$ was measured with an uncertainty of 30 keV (FWHM), of the same order as direct measurement at the energies investigated through the THM (from 30 keV up to about 300 keV).

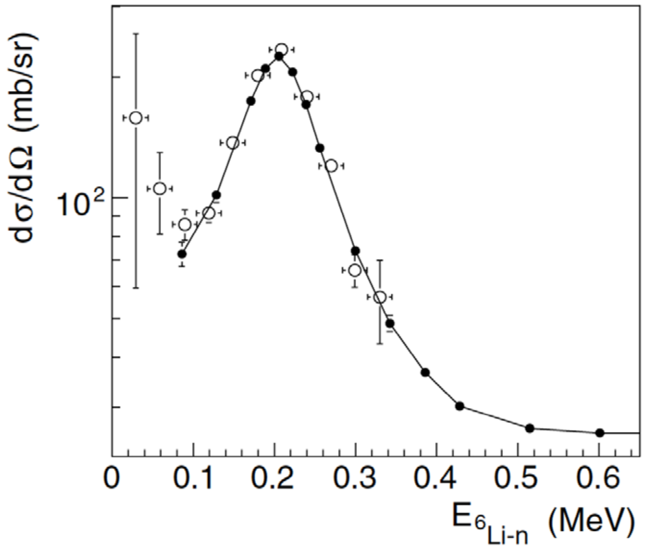

Figure 32. Two-body cross section obtained in Gulino *et al* (2010) (open circles) compared with the directly measured ones (full dots) (Overley *et al* 1974) integrated over the center-of-mass angular region $\theta_{\mathrm{cm}} = 95° - 110°$. The line is just to guide the eye.

Figure 32 shows the comparison between the THM cross section of the ^{6}Li(n,α)^{3}H reaction (open circles) and direct data from Overley *et al* (1974) (full dots). Good agreement corroborates the use of the THM to investigate n-induced reactions leading to results comparable to direct data. The two-body cross section obtained in Overley *et al* (1974) was fitted using a sum of a Breit–Wigner function and of the *1/v* trend that describes the cross section for low neutron energies. The same *1/v* function was added to THM data as in the THM measurement neutrons take part to the reaction as off-energy-shell particles. Moreover, to account for the HOES shell nature of the THM cross section, the indirect data were multiplied by the centrifugal barrier penetration factor (equation (4.2)). Finally, the normalization factor was calculated in the energy region where the 200 keV resonance is present equaling the areas of direct and indirect measured resonance peaks. The THM data were fitted with the sum of a Breit–Wigner function and a *1/v* term to evaluate the resonance properties. The fitting procedure yielded a resonance energy of 204 ± 4 keV with a FWHM of 96 ± 8 keV, in excellent agreement with the fit performed on direct data.

5. Experiments on CD in rare isotope facilities

The experimental advantages of the Coulomb breakup method are: (i) the large number of virtual photons provided by a high-Z target leads to large CD cross sections, (ii) the photoabsorption cross section in equation (2.96) is favored compared to the radiative capture cross section by two to three orders of magnitude, and (iii) thick targets can be used in the regime of fast beams leading to a higher luminosity (Motobayashi 1998). A challenging requirement for experiments, however, is the need for the measurement of angular distributions. The multipolarities have to be disentangled since the electromagnetic multipoles contribute with different strengths to Coulomb excitation and capture processes. Particularly important are the non-negligible contributions and interference of electric dipole ($E1$) and electric quadrupole ($E2$) excitations (Bertulani 1994, Gai and Bertulani 1995, Esbensen and Bertsch 1995, 1996, Bertulani and Gai 1998). The applicability of the CD approach is limited by the fact that preferentially $E1$ modes are excited and that the detailed balance theorem cannot be used for the extraction of the radiative capture cross section in case the capture feeds bound excited states that decay by γ-ray emission with unknown branching ratio (Motobayashi 1998). The main body of experimental work utilizing Coulomb breakup of rare isotopes for nuclear astrophysics has been aimed at exploring radiative proton capture reactions.

5.1. (a) Radiative capture

An extensive experimental program using Coulomb breakup reactions to extract radiative capture cross sections was initiated by Motobayashi *et al* (1991) (see also Motobayashi (2003)). In the pioneering 1991 experiment, the electromagnetic transition strength for the excited 1^- resonance in ^{14}O was determined in the CD, $^{14}\text{O} \rightarrow {}^{13}\text{N} + \text{p}$, induced by 87.5 MeV/nucleon ^{14}O impinging upon a Pb target (Motobayashi *et al* 1991). The CD cross section was determined from coincidence spectroscopy of protons and ^{13}N. The complete kinematics—total energy and relative momentum vectors of the $p+{}^{13}$N system—were determined. The radiative width Γ_γ was deduced and found in agreement with the direct measurement performed at Louvain-la-Neuve by Decrock *et al* (1991). The CD cross sections of $^{14}\text{O} \rightarrow {}^{13}\text{N} + \text{p}$ (Kiener *et al* 1993) and $^{12}\text{N} \rightarrow {}^{11}\text{C} + \text{p}$ were also published by Lefebvre *et al* (1995). Radioactive beams of ^{14}O at 70 MeV/nucleon and ^{12}N at 65.5 MeV/nucleon were used on ^{208}Pb targets, respectively. A test has been done for the CD of ^{15}C into ^{14}C+n, whose inverse reaction ^{14}C(n,γ) has been measured. Summer and Nunes (2008) and Esbensen (2009) have shown that a full dynamical model is needed to reproduce the CD data, and that the ANC extracted from the confrontation between theory and experiment is in excellent agreement with the radiative-capture data.

Experiments aimed at the CD of ^{8}B (Kikuchi *et al* 1997, 1998) to extract the reaction rate of the crucial ^{7}Be(p, γ)^{8}B reaction, which is of great importance for the neutrino production in the Sun through the β decay of ^{8}B. In the first experiment by Kikuchi *et al* (1997), the breakup of a ^{8}B beam of 46.5 MeV/nucleon incident on a ^{208}Pb target was measured. In a second experiment by Kikuchi *et al* (1998), the angular range was extended to cover from 6° to 10° and the fraction of the breakup leading to the 429 keV bound excited state in ^{7}Be was obtained. An assessment of the $E2$ contribution to the breakup process was also obtained. Much higher beam energies available for CD of $^8\text{B} \rightarrow {}^7\text{Be} + \text{p}$ were obtained in two experiments at 254 MeV/nucleon ^{8}B beam energy (Iwasa *et al* 1999, Schümann *et al* 2003). Tracking of the angle of the incoming beam allowed for measuring angular distributions to disentangle contributing multipolarities in the second experiment (Schümann *et al* 2006). Inclusive and exclusive measurements of the $^8\text{B} \rightarrow {}^7\text{Be} + \text{p}$ CD were performed by Davids *et al* (2001, 2003). The longitudinal momentum distributions of ^{7}Be were derived. In comparison to model calculations, a rather high $E2$ contribution to the Coulomb breakup was deduced, which has not been confirmed by any other measurement to date. Gai (2006), Adelberger *et al* (2011) and Bertulani and Gade (2010) summarized the results of the various ^{8}B CD measurements and the extracted the astrophysical $S_{17}(0)$ factor, comparing with direct capture measurements.

The astrophysical S-factor for the reaction ^{7}Be(p,γ)^{8}B was calculated (Navratil *et al* 2006) and excellent agreement was found with the experimental data in both direct and indirect measurements (Navratil*et al* 2006, 2011). The low- and high-energy slopes of the S-factor obtained with a many-body microscopic calculation by Navratil *et al* (2006) is well described by the fit (Bertulani 2013)

$$S_{17}\left(\mathrm{E}_x\right) = (22.109\ \text{eV b})\ \frac{1 + 5.30E + 1.65E^2 + 0.857E^3}{1 + E/0.1375}, \tag{5.1}$$

where E is the relative energy (in MeV) of p+^{7}Be in their center-of-mass. This equation corresponds to a Padé approximant of the S-factor. A sub-threshold pole due to the binding energy of ^{8}B is responsible for the denominator (Jennings *et al* 1998, Williams and Koonin 1981). Figure 4 shows the world data on ^{7}Be(p, γ)^{8}B compared to a few of the theoretical calculations. The recent compilation published by Adelberger *et al* (2011) recommends $S_{17} = 20.8 \pm 0.7(\text{expt}) \pm 1.4(\text{theor})$ eV b.

The reactions ^{8}B(p,γ)^{9}C, ^{11}C(p,γ)^{12}N and ^{12}N(p,γ)^{13}O, important for the hot pp mode nuclear burning in hydrogen-rich, very massive objects (Wiescher *et al* 1989) were studied via Coulomb breakup to extract the reaction rates relevant to explosive hydrogen burning (Motobayashi 2003). Subsequent measurements on sd-shell nuclei aimed at the study of the breakup of ^{23}Al (Gomi *et al* 2005) and ^{27}P (Togano *et al* 2005) into ^{22}Mg+p and ^{26}Si+p. The experimental results in the sd-shell are relevant to the reaction path in Ne novae (Gehrz *et al* 1985), where at high temperature and density many nuclear reactions involving rare isotopes contribute in the hot-CNO cycle and the NeNa- and MgAl-cycles (Champagne and Wiescher 1992). A specific signature is the nucleosynthesis of long-lived galactic γ emitters such as ^{22}Na and ^{26}Al, and nucleosynthesis up to the silicon and calcium range (Starrfield *et al* 2000).

Assuming temperature and density conditions given by nova models (Iliadis *et al* 2002), the radiative width obtained in the study indicates that the main reaction path favors the

β decay rather than the proton capture on ^{22}Mg (Gomi *et al* 2005). For ^{26}Si+p, the preliminary result of the γ-decay width of the first excited state in ^{27}P is ten times smaller than the value estimated based on a shell-model calculation in Caggiano *et al* (2001). This indicates that the ^{26}Si(p,γ)^{27}P reaction does not contribute significantly to the amount of ^{26}Al produced in novae (Togano *et al* 2005).

The neutron capture reaction on ^{14}C has been explored using CD of $^{15}\text{C} \rightarrow {}^{14}\text{C} + \text{n}$ at 69 MeV/nucleon in the field Pb target (Nakamura *et al* 2009). The deduced direct capture cross section agrees with the most recent direct capture measurement and demonstrates that the Coulomb breakup with a neutron in the exit channel is a useful tool to derive the radiative capture cross section. A program aimed at Coulomb breakup of neutron-rich nuclei, not exclusively with an astrophysical background, is also ongoing at higher beam energies (Aumann 2006, Pramanik *et al* 2003, Adrich *et al* 2005, Nociforo *et al* 2005).

The two-neutron capture on ^{4}He could perhaps play a role in the post-collapse phase in type-II supernovae. The bottleneck in this nucleosynthesis scenario is the formation of nuclei with $A \geqslant 9$ from nucleons and α-particles. In principle, the reaction ^{4}He(2n,γ)^{6}He could be relevant in bridging the instability gap at $A = 5$, although it is believed that this reaction cannot compete with the (αn,γ) process in a type-II supernova scenario. Experiments with CD have been used to study this question (Aumann *et al* 1999). From the analysis of this experiment it was found that 10% of the dissociation cross section proceeds via the formation of ^{5}He. A rough estimate yields 1.6 mb MeV for the photoabsorption cross section for ^{6}He(γ,n)^{5}He, which agrees with theoretical calculations (Danilin *et al* 1998, Cobis *et al* 1997, Efros *et al* 1996). From this experiment one concludes that the cross sections for formation of ^{5}He and ^{6}He via one (two) neutron capture by ^{4}He are not large enough to compete with the (αn, γ) capture process (for more details, see Aumann (2006)). This and the previously mentioned examples, show the relevance of the CD method to assess some of the basic questions of relevance for nuclear astrophysics.

A few more recent experiments using the CD method are worth mentioning. The proton-rich nucleus ^{31}Cl was studied experimentally using the CD of a ^{31}Cl beam and the first excited state in ^{31}Cl was observed which is relevant to the resonant capture in the stellar ^{30}S(p,γ)^{31}Cl reaction (Togano *et al* 2011). The determination of the ^{7}Li(n,γ)^{8}Li radiative capture cross section by means of the dissociation of ^{8}Li beams (Izsak *et al* 2013). The deduced (n,γ) excitation function is consistent with data for the direct capture reaction ^{7}Li(n,γ)^{8}Li and with low-energy effective field theory calculations (Rupak and Higa 2011). The astrophysical ^{26}Si(p,γ)^{27}P reaction is studied using the CD of ^{27}P (Beceiro Novo *et al* 2012). Four resonant states measured at 0.36±0.07, 0.88±0.09, 1.5±0.2, 2.3±0.3 MeV and evidence of a higher state at around 3.1 MeV was found. Measurement of the ^{92,93,94,100}Mo(γ,n) reactions by CD (Göbel *et al* 2013). These measurements helped to understand the production of proton-rich nuclei produced under explosive conditions in a sequence of photodissociations of s- and r-process seeds and subsequent decays.

5.2. (b) Pygmy resonances

In neutron-rich nuclei, one expects the appearance of electric-dipole strength at energies near the neutron separation threshold. Located below the well-known giant dipole resonance (GDR), which has already been studied extensively in stable species (Dietrich and Berman 1988), this new low-lying E1 strength distribution is often denoted as pygmy dipole resonance (PDR), referring to its much smaller photoabsorption strength compared to that of the GDR. Pygmy resonances were proposed by Suzuki *et al* (1990), using the hydrodynamical model for collective vibrations. The PDR provides an experimental access to the equation-of-state (EOS) of asymmetric nuclear matter, and thus a link to the neutron skin evolution (Piekarewicz 2011), as well as about the abundance distribution of heavy elements in the universe (Goriely 1988).

The possibility to explain the soft dipole modes in terms of direct breakup, has made it very difficult to clearly identify the signature of pygmy resonances in exotic nuclei. This can be shown by using the electric dipole strength function in the cluster breakup model, namely (Bertulani and Sustich 1992)

$$\frac{\mathrm{d}B\,(\mathrm{E1},\,E)}{\mathrm{d}E} = C\,\frac{3\hbar e^2 Z_{\mathrm{eff}}^2}{\pi^2\mu}\,\frac{\sqrt{S}\,(E-S)^{3/2}}{E^4}, \tag{5.2}$$

where E is the total excitation energy. C is a constant of the order of unity, accounting for the corrections to the wavefunction. This function has a peaks at $E = 3S/5$ which can become very small if the separation energy S is also small. Thus it becomes hard to say if a peak at low energies in the response function of a neutron-rich nucleus is due to direct breakup or to the excitation of a pygmy resonance that subsequently decays by neutron emission. The same conclusion is reached by using a three-body breakup mechanism. As pointed out by Pushkin *et al* (1996), the $E1$ three-body response function can be described by an expression similar to equation (5.2), but with different powers. Explicitly, $\mathrm{d}B(E1)/\mathrm{d}E \propto (E - S_{2n})^3/E^{11/2}$. Instead of S_{2n}, one has to use an effective $S_{2n}^{eff} = aS_{2n}$, with $a \sim 1.5$. The peak of the strength function in the three-body case is situated at about three times higher energy than for the two-body case, equation (5.2). In the three-body model, the maximum is thus predicted at $E \sim 1.8S_{2n}$, which fits the experimentally determined peak position for three-body breakup. For example the ^{11}Li $E1$ strength function is very well reproduced with this direct breakup model (Bertulani 2007). The effect of three-body configurations is to widen and to shift the strength function $\mathrm{d}B(E1)/\mathrm{d}E$ to higher energies, as shown in figure 34.

One of the first PDR observations was realized with CD (γ, xn) of neutron-rich Sn isotopes (Adrich *et al* 2005). The PDR was measured in ^{130}Sn and ^{132}Sn at energies around 10 MeV and exhausted 7(3)% and 4(3)% of the $E1$ energy-weighted sum rule, respectively. The comparison of these results with RPA calculations by Klimkiewicz *et al* (2007) served to constrain the symmetry energy and the symmetry-energy pressure in the EOS, as well as the neutron-skin of Sn isotopes and of ^{208}Pb. The low-lying $E1$ strength in ^{68}Ni was measured with this technique by Wieland *et al* (2009), revealing 5% of the $E1$ energy-weighted sum-rule strength

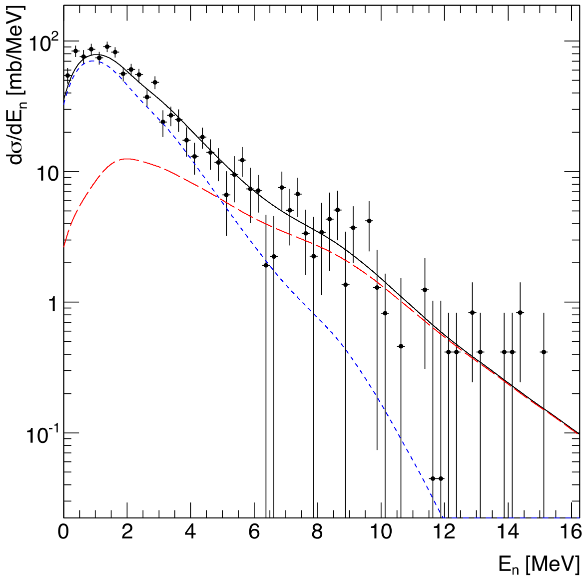

Figure 33. Neutron kinetic energy-differential cross section for the ^{68}Ni(γ,n)^{67}Ni channel. The experimental data (solid points), the total neutron kinetic energy fit (solid line), the statistical decay component (dotted line) and the non-statistical decay component (dashed line) are shown (Rossi *et al* 2013).

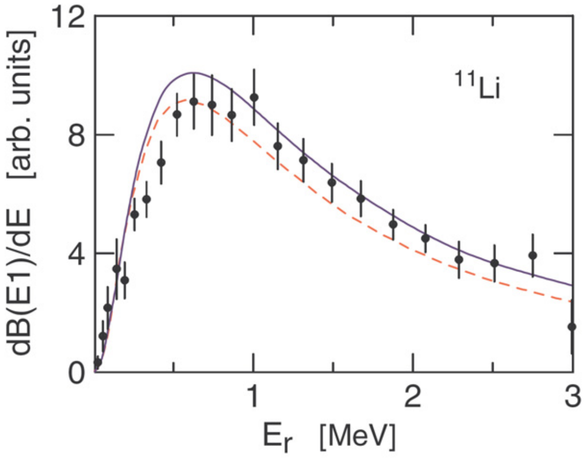

Figure 34. Comparison between the calculation of the response function (in arbitrary units) with a three-body model (dashed line) as reported by Bertulani (2007). The solid curve includes the effects of final state interactions. The experimental data are from Shimoura *et al* (1995).

under the assumption of a branching ratio for the direct γ-decay of 4% in the PDR region. From these results, Carbone *et al* (2010) derived symmetry-energy parameters that are in good agreement with those previously obtained from ^{130,132}Sn. Recently, the GDR and additional low-lying strength have been observed in ^{68}Ni, the latter exhausting 4.1(1.9)% of the $E1$ energy-weighted sum rule (Rossi *et al* 2013). This is shown in figure 33. The branching ratio for the non-statistical decay of the excited ^{68}Ni nuclei was measured as 24(4)%.

5.3. (c) Relativistic Coulomb fission

Relativistic Coulomb fission is an optimum reaction mechanism for the production of medium-mass neutron-rich nuclei. Electromagnetic-induced fission of several neutron-deficient actinides and pre-actinides have been studied at the GSI Darmstadt by use of relativistic secondary beams (Geissel *et al* 1992, Schmidt *et al* 1994, Böckstiegel *et al* 1997, 2008). The cross sections proceed via the excitation of the GDR, but also with a sizable contribution of the double giant dipole resonance (DGDR) as first proposed by Baur and Bertulani (1986). The cross section for the excitation of GDR in a nucleus 1 due to the Coulomb interaction with a nucleus 2 is roughly given by

$$\sigma_{\rm GDR} = \left(3.42 \times 10^{-3}\ {\rm mb}\right) \frac{Z_1 N_1 Z_2^2}{A_1^{2/3}} \ln\left(\frac{2\gamma A_1^{1/3}}{A_1^{1/3} + A_2^{1/3}}\right), \tag{5.3}$$

where γ is the Lorentz factor associated with the relative velocity between the two nuclei. Thus, the cross section increases substantially at very large energies. Much of the excitation cross section goes to the excitation of the DGDR (Baur and Bertulani 1986), responsible for exotic decay modes. The excited nucleus decays mostly by fission leading to neutron-rich fragments.

Figure 35 shows the calculated distribution of fragment yields in relativistic Coulomb breakup of ^{238}U projectiles using the LISE++ code (Tarasov 2012). It is evident that most fragments are neutron rich, many of them having been poorly or never observed by using other techniques. For example, intense beams of ^{238}U at the new Radioactive Ion Beam Factory in RIKEN made possible the production of 45 new medium-mass neutron-rich nuclei in in-flight fission reactions (Ohnishi *et al* 2010). The electromagnetic interaction between fast nuclei allows the study of nuclear properties not accessible via other techniques, also allowing for the production of new isotopes which can further be studied in secondary beam experiments.

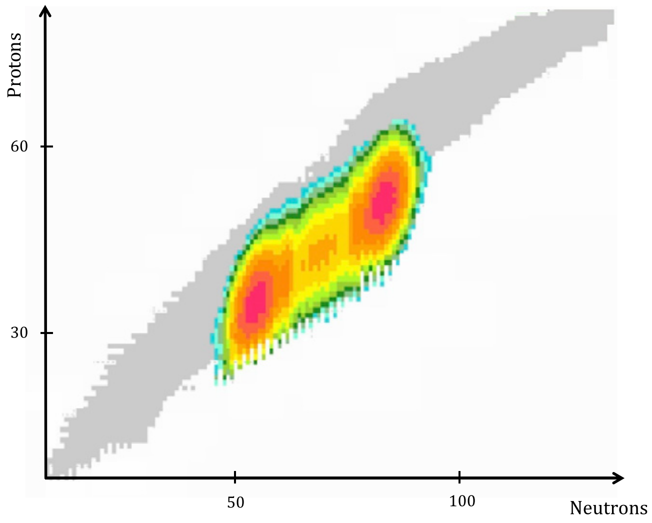

Figure 35. Contour plot on the nuclear chart of calculated distribution of fragment yields in relativistic Coulomb breakup of ^{238}U projectiles (Tarasov 2012).

6. Summary and conclusions

In this review, we have focused on three indirect techniques—the ANC, THM and CD methods—that have been used extensively for determining reaction rates in nuclear astrophysics. The theoretical description of the three techniques has been presented and a review of the use of the techniques with both stable and radioactive-ion beams has been given. The techniques are now well established tools in nuclear astrophysics.

As rare isotope beam facilities are developed around the world, indirect methods will play a major role in determining rates for reactions that occur on short-lived isotopes. The work that has been done to date with rare-isotope beams represents only the first steps in this effort. Beam intensities and beam species will expand dramatically by the end of this decade opening up many new opportunities to further utilize indirect tools to learn about the nuclear reactions that drive the cosmos.

Acknowledgments

AMM and RET acknowledge that this material is based upon work supported by the US Department of Energy, Office of Science, Office of Nuclear Science under Award Numbers DE-FG02-93ER40773, DE-FG52-09NA29467 and the US Department of Energy, National Nuclear Security Administration, under Award Number DE-NA0001785 and DE-NA0001786. AMM is also supported by the US Department of Energy, Office of Science, Office of Nuclear Science under Award DE-SC0004958. CAB and AMM acknowledge support by the US National Science Foundation under Award PHY-1415656. CAB also acknowledges support under US DOE Grants DE-FG02-08ER41533 and DE-SC0004971. ML and CS acknowledge support from the Italian Ministry for University Research grant RBFR082838, and INFN-LNS-Astrofisica Nucleare (fondi premiali).

References

Abia C *et al* 2010 *Astrophys. J.* **715** L94
Abia C*et al* 2011 *Astrophys. J.* **737** L8
Adelberger E G *et al* 1998 *Rev. Mod. Phys.* **70** 1265
Adelberger E G *et al* 2011 *Rev. Mod. Phys.* **83** 195
Adrich P *et al* 2005 *Phys. Rev. Lett.* **95** 132501
Al-Abdullah T *et al* 2010 *Phys. Rev.* C **81** 035802
Al-Abdullah T *et al* 2014 *Phys. Rev.* C submitted
Alder K and Winther A 1975 *Electromagnetic Excitation* (Amsterdam: North-Holland)
Aleixo A N and Bertulani C A 1989 *Nucl. Phys.* A **505** 448
Aliotta M *et al* 2000 *Eur. Phys. J.* A **9** 435
Aliotta M *et al* 2001 *Nucl. Phys.* A **690** 790
Alt E O *et al* 2005 *Phys. Rev.* C **71** 024605
Angulo C *et al* 1993 *Z. Phys.* A **345** 231
Angulo C *et al* 1999 *Nucl. Phys.* A **656** 3
Assenbaum H J *et al* 1987 *Z. Phys.* A **327** 461
Aumann T 2006 *Eur. Phys. J.* A **26** 441
Aumann T *et al* 1999 *Phys. Rev.* C **59** 1252
Azhari A *et al* 1999a *Phys. Rev. Lett.* **82** 3960
Azhari A *et al* 1999b *Phys. Rev.* C **60** 055803
Azhari A *et al* 2001 *Phys. Rev.* C **63** 055803
Baby L T *et al* 2003 *Phys. Rev. Lett.* **90** 022501
Baby L T *et al* 2004 *Phys Rev Lett.* **92** 029901 (erratum)
Balantekin A B *et al* 1997 *Nucl. Phys.* A **627** 324
Banu A *et al* 2009 *Phys. Rev.* C **79** 025805
Banu A *et al* 2012 *Phys. Rev.* C **86** 015806
Barbarino S *et al* 1980 *Phys. Rev.* C **21** 1104
Barker F C 2000 *Phys. Rev.* C **62** 044607
Barker F C 2002 *Nucl. Phys.* A **707** 277
Barker F C 2008 *Phys. Rev.* C **78** 044611
Barker F C and Kajino T 1991 *Aust. J. Phys.* **44** 369
Baye D *et al* 2005 *Phys. Rev. Lett.* **95** 082502
Baur G and Bertulani C A 1986 *Phys. Lett.* B **174** 23
Baur G 1986 *Phys. Lett.* B **178** 135
Baur G *et al* 1986 *Nucl. Phys.* A **458** 188
Baur G *et al* 1992 *Nucl. Phys.* A **550** 527
Beceiro Novo S *et al* 2012 *J. Phys.: Conf. Ser.* **381** 012115
Becker H W *et al* 1987 *Z. Phys.* A **327** 341
Becker H W *et al* 1995 *Z. Phys.* A **351** 453
Bem P *et al* 2000 *Phys. Rev.* C **62** 024320
Bertone P F *et al* 2001 *Phys. Rev. Lett.* **87** 152501
Bertsch G F and Bertulani C A 1993 *Nucl. Phys.* A **556** 136
Bertulani C A 1994 *Phys. Rev.* C **49** 2688
Bertulani C A 1995 *Nucl. Phys.* A **587** 318
Bertulani C A 1996 *Z. Phys.* A **356** 293
Bertulani C A 2002 *Phys. Lett.* B **3** 205
Bertulani C A 2005 *Phys. Rev. Lett.* **94** 072701
Bertulani C A 2007 *Phys. Rev.* C **75** 024606
Bertulani C A 2013 *Acta Phys. Pol.* **44** 531
Bertulani C A and Baur G 1985 *Nucl. Phys.* A **442** 739
Bertulani C A and Bertsch G F 1994 *Phys. Rev.* C **49** 2839
Bertulani C A and Canto L F 1992 *Nucl. Phys.* A **539** 163
Bertulani C A and Gai M 1998 *Nucl. Phys.* A **636** 227
Bertulani C A and Gade A 2010 *Phys. Rep.* **485** 195
Bertulani C A and Nathan A M 1993 *Nucl. Phys.* A **554** 158
Bertulani C A and Sustich A 1992 *Phys. Rev.* C **46** 2340
Bethe H A 1939 *Phys. Rev.* **55** 103
Blatt J M and Biedenharn L C 1952 *Rev. Mod. Phys.* **24** 258
Blokhintsev L D *et al* 1977 *Fiz. Elem. Chastits At. Yadra* **8** 1189
Blokhintsev L D *et al* 1977 *Sov. J. Part. Nucl.* **8** 485
Blokhintsev L D *et al* 1984 *Fiz. Elem. Chastits At. Yadra* **15** 1296–337
Blokhintsev L D *et al* 1984 *Sov. J. Part. Nucl.* **15** 580–99
Böckstiegel C *et al* 1997 *Phys. Lett.* B **398** 259
Böckstiegel C *et al* 2008 *Nucl. Phys.* A **802** 12
Boesgaard A M 2004 The light elements: lithium, beryllium, and boron *Origin and Evolution of the Elements* (*Carnegie Observatories Astrophysics Series* vol 4) ed A McWilliam and M Rauch (Cambridge: Cambridge University Press)
Bracci L *et al* 1990 *Nucl. Phys.* **513** 316
Broggini C *et al* 2007 *Annu. Rev. Nucl. Part. Sci.* **60** 53
Broggini C 2010 *Prog. Part. Nucl. Phys.* **64** 429
Burjan V 2013 private communication
Busso M *et al* 1999 *Annu. Rev. Astron. Astrophys.* **37** 239
Caggiano J A *et al* 2001 *Phys. Rev.* C **64** 025802
Calvi G *et al* 1990 *Phys. Rev.* C **41** 1848
Capel P *et al* 2003 *Phys. Rev.* C **68** 014612
Capel P and Baye B 2005 *Phys. Rev.* C **71** 044609
Carbone A *et al* 2010 *Phys. Rev.* C **81** 041301(R)
Coughlan G R and Fowler W A 1988 *At. Data Nucl. Data Tables* **40** 283
Champagne A E and Pitt M 1986 *Nucl. Phys.* A **457** 367
Champagne A E and Wiescher M 1992 *Annu. Rev. Nucl. Part. Sci.* **42** 39
Cherubini S *et al* 1996 *Astrophys. J.* **457** 855
Cherubini S *et al* 2012 *AIP Conf. Proc.* **1484** 293
Chew G F and Wick G C 1952 *Phys. Rev.* **85** 636
Chow H C *et al* 1975 *Can. J. Phys.* **53** 1672
Clayton G C *et al* 2007 *Astrophys. J.* **662** 1220
Cline D 1988 *Annu. Rev. Part. Sci.* **36** 683
Cobis A *et al* 1997 *Phys. Rev. Lett.* **79** 2411
Constanzo E *et al* 1990 *Nucl. Instrum. Methods* A **295** 373
Cruz J *et al* 2008 *J. Phys. G: Nucl. Part. Phys.* **35** 014004
Cyburt H C 2004 *Phys. Rev.* D **70** 023505
Danilin B V *et al* 1998 *Nucl. Phys.* A **632** 383
Davids B *et al* 2001 *Phys. Rev. Lett.* **86** 2750

Davids B *et al* 2003 *Phys. Rev.* C **63** 065806
Davidson J M *et al* 1979 *Nucl. Phys.* A **315** 253
Decrock P *et al* 1991 *Phys. Rev. Lett.* **67** 808
Dietrich S S and Berman B L 1988 *At. Data Nucl. Data Tables* **38** 199
Dolinsky E I *et al* 1973 *Nucl. Phys.* A **202** 97
Dolinsky E I and Mukhamedzhanov A M 1977 *Izv. A.N. SSR, Ser Fiz* **41** 55
Dombrowski H *et al* 1997 *Nucl. Phys.* A **619** 97
Dunkley J *et al* 2009 *Astrophys. J.* **180** (Suppl.) 306
Efros V *et al* 1996 *Z. Phys.* A **355** 101
Engstler S *et al* 1992a *Z. Phys.* A **342** 471
Engstler S *et al* 1992b *Phys. Lett.* B **279** 20
Esbensen H 2009 *Phys. Rev.* C **80** 024608
Esbensen H and Bertsch G F 1995 *Phys. Rev. Lett.* **359** 13
Esbensen H and Bertsch G F 1996 *Nucl. Phys.* A **600** 37
Esbensen H *et al* 1995 *Nucl. Phys.* A **581** 107
Esbensen H *et al* 2005 *Phys. Rev. Lett.* **94** 042502
Fields B D 2011 *Annu. Rev. Nucl. Part. Sci.* **61** 47
Furic M *et al* 1972 *Phys. Lett.* B **39** 629
Gagliardi C A *et al* 1998 *Phys. Rev. Lett.* **80** 421
Gagliardi C A *et al* 1999 *Phys. Rev.* C **59** 1149
Gai M 2006 *Phys. Rev.* C **74** 025810
Gai M and Bertulani C A 1995 *Phys. Rev.* C **52** 1706
Gehrz R D *et al* 1985 *Astrophys. J. Lett.* **298** L47
Geissel H *et al* 1992 *Nucl. Instrum. Methods* B **70** 286
Göbel K *et al* 2013 arXiv:1310.2165
Goldstein G *et al* 2007 *Phys. Rev.* C **76** 024608
Gomi T *et al* 2005 *J. Phys. G: Nucl. Part. Phys.* **31** S1517
Goriely S 1988 *Phys. Lett.* B **436** 10
Gubler H P *et al* 1977 *Nucl. Phys.* A **284** 114
Gulino M *et al* 2010 *J. Phys. G: Nucl. Part. Phys.* **37** 125105
Gulino M *et al* 2013 *Phys. Rev.* C **87** 012801(R)
Hammache F *et al* 1999 *Phys. Rev. Lett.* **80** 928
Heisenberg W 1946 *Z. Naturf.* **1** 608
Herwig F 2005 *Annu. Rev. Astron. Astrophys.* **43** 435
Hu N 1948 *Phys. Rev.* **74** 131
Igamov S B and Yamukhamedov R 2007 *Nucl. Phys.* A **781** 247
Iliadis C *et al* 2002 *Astrophys. J. Suppl.* **142** 105
Iliadis C 2007 *Nuclear Physics of Stars* (Weinheim: Wiley-VCH)
Iwasa N*et al* 1999 *Phys. Rev. Lett.* **83** 2910
Izsak R *et al* 2013 *Phys. Rev.* C **88** 065808
Jackson J D and Blatt J M 1950 *Rev. Mod. Phys.* **22** 77
Jennings B K *et al* 1998 *Phys. Rev.* C **58** 579
Johnson E D *et al* 2006 *Phys. Rev. Lett.* **97** 192701
Jorissen A *et al* 1992 *Astron. Astrophys.* **261** 164
Junghans A R *et al* 2002 *Phys. Rev. Lett.* **88** 041101
Kadyrov A S *et al* 2009 *Ann. Phys.* **324** 1516
Kamimura M and Kameyama H 1990 *Nucl. Phys.* A **508** 17c
Käppeler F *et al* 1998 *Annu. Rev. Nucl. Part. Sci.* **48** 175
Kasagi J *et al* 1975 *Nucl. Phys.* A **239** 233
Kido T *et al* 1996 *Phys. Rev.* C **53** 2296
Kiener J *et al* 1993 *Nucl. Phys.* A **552** 66
Kikuchi T *et al* 1997 *Phys. Lett.* B **391** 261
Kikuchi T *et al* 1998 *Eur. Phys. J.* A **3** 213
Klimkiewicz A *et al* 2007 *Phys. Rev.* C **76** 051603(R)
Kramers H A 1938 *Hand Jahrbuch der Chem. Phys.* **1** 312
Kunz P D, unpublished, University of Colorado
La Cognata M *et al* 2005 *Phys. Rev.* C **72** 065802
La Cognata M *et al* 2006 *Eur. Phys. J.* A **27** 249
La Cognata M *et al* 2007 *Phys. Rev.* C **76** 065804
La Cognata M *et al* 2008a *J. Phys. G: Nucl. Part. Phys.* **35** 014014
La Cognata M *et al* 2008b *Phys. Rev. Lett.* **101** 152501
La Cognata M *et al* 2009 *Phys. Rev.* C **80** 012801
La Cognata M *et al* 2010a *Astrophys. J.* **708** 796
La Cognata M *et al* 2010b *Astrophys. J.* **723** 1512
La Cognata M *et al* 2010c *Nucl. Phys.* A **834** 658
La Cognata M *et al* 2011 *Astrophys. J. Lett.* **739** L54
La Cognata M *et al* 2012 *Phys. Rev. Lett.* **109** 232701
La Cognata M *et al* 2013 *Astrophys. J.* **777** 143
Lambert J *et al* 1982 *Phys. Rev.* C **26** 357
Lamia L *et al* 2009 *Il Nuovo Cimento* C **31** 423
Lamia L *et al* 2010 *Nucl. Phys.* A **834** 655
Lamia L *et al* 2012a *J. Phys. G: Nucl. Part. Phys.* **39** 015106
Lamia L *et al* 2012b *Phys. Rev.* C **85** 025805
Lamia L *et al* 2012c *Astron. Astrophys.* **541** 158
Lamia L *et al* 2013 *Astrophys. J.* **768** 65
Lane A M and Thomas R G 1958 *Rev. Mod. Phys.* **30** 257
Lattuada M *et al* 1984 *Phys. Rev.* C **30** 531
Lattuada M *et al* 1985 *Nucl. Phys.* A **458** 493
Lattuada M *et al* 2001 *Astrophys. J.* **562** 1076
Le Blanc P J *et al* 2010 *Phys. Rev.* C **82** 055804
Lefebvre A *et al* 1995 *Nucl. Phys.* A **592** 69
Liu W *et al* 1996 *Phys. Rev. Lett.* **77** 611
Locher M P and Mizutani T 1978 *Phys. Rep.* **46** 43
Long W H and Bertulani C A 2011 *Phys. Rev.* C **83** 024907
Lorentz-Wirzba H *et al* 1979 *Nucl. Phys.* A **313** 346
Lucatello S *et al* 2011 *Astrophys. J.* **729** 40
Lugaro M *et al* 2004 *Astrophys. J.* **615** 934
Margaziotis D *et al* 1970 *Phys. Rev.* C **2** 2050
Marta M *et al* 2008 *Phys. Rev.* C **78** 022802(R)
McCleskey M 2013 private communication
Meléndez J *et al* 2010 *Astron. Astrophys.* **515** L3
Melezhik V S 1997 *Phys. Lett.* A **230** 203
Möller C 1946 *Dan. Vid Seisk. Mat. Fys. Medd.* **22**
Morlock R *et al* 1997 *Phys. Rev. Lett.* **79** 3837
Motobayashi T 1998 *Nucl. Phys.* A **630** 328
Motobayashi T 2003 *Nucl. Phys.* A **719** C65
Motobayashi T *et al* 1991 *Phys. Lett.* B **264** 259
Motobayashi T *et al* 1994 *Phys. Rev. Lett.* **73** 2680
Mukhamedzhanov A M 2011 *Phys. Rev.* C **84** 044616
Mukhamedzhanov A M 2012 *Phys. Rev.* C **86** 044615
Mukhamedzhanov A M and Kadyrov A S 2009 *Phys. Rev.* C **82** 051601(R)
Mukhamedzhanov A M and Nunes F M 2005 *Phys. Rev.* C **72** 017602
Mukhamedzhanov A M and Timofeyuk N K 1990 *Yad. Fiz.* **51** 679
Mukhamedzhanov A M and Timofeyuk N K 1990 *Sov. J. Nucl. Phys.* **51** 431
Mukhamedzhanov A M and Tribble R E 1999 *Phys. Rev.* C **59** 3418
Mukhamedzhanov A M *et al* 1995 *Phys. Rev.* C **51** 3472
Mukhamedzhanov A M *et al* 1997 *Phys. Rev.* C **56** 1302
Mukhamedzhanov A M *et al* 2001 *Phys. Rev.* C **63** 024612
Mukhamedzhanov A M *et al* 2002 *Phys. Rev.* C **66** 027602
Mukhamedzhanov A M *et al* 2003a *Phys. Rev.* C **67** 065804
Mukhamedzhanov A M *et al* 2003b *Nucl. Phys.* A **725** 279
Mukhamedzhanov A M *et al* 2006 *Phys. Rev.* C **73** 035806
Mukhamedzhanov A M *et al* 2008a *Phys. Rev.* C **77** 051601(*R*)
Mukhamedzhanov A M *et al* 2008b *Phys. Rev.* C **78** 015804
Mukhamedzhanov A M *et al* 2011 *Phys. Rev.* C **83** 044604
Nakamura T *et al* 2009 *Phys. Rev.* C **79** 035805
Nakatsukasa T *et al* 2008 *Eur. Phys. J.* **156** 249 (special topics)
Navratil P *et al* 2006 *Phys. Lett.* B **634** 191
Navratil P *et al* 2006 *Phys. Rev.* C **73** 065801
Navratil P *et al* 2011 arXiv:1105.5977
Nociforo C*et al* 2005 *Phys. Lett.* B **605** 79
Nollett K M *et al* 2003 *Astrophys. J.* **582** 1036
Nunes F M and Mukhamedzhanov A M 2001 *Phys. Rev.* C **64** 062801
Ogata K *et al* 2003 *Phys. Rev.* C **68** 064609
Ogata K *et al* 2006 *Phys. Rev.* C **73** 024605
Ogata K and Bertulani C A 2009 *Prog. Theor. Phys. (Lett.)* **121** 1399
Ogata K and Bertulani C A 2010 *Prog. Theor. Phys.* **123** 701
Ogata K *et al* 2011 *J. Phys.: Conf. Ser.* **312** 082008
Ohlsen G G 1965 *Nucl. Instrum. Methods* **37** 240
Ohnishi T *et al* 2010 *J. Phys. Soc. Japan* **79** 073201
Overley J C *et al* 1974 *Nucl. Phys.* A **221** 573
Palmerini S *et al* 2013 *Astrophys. J.* **764** 128

Pan J *et al* 1970 *Nucl. Phys.* A **150** 216
Pandey G *et al* 2008 *Astrophys. J.* **674** 1068
Pang D Y *et al* 2007 *Phys. Rev.* C **75** 024601
Perey C M and Perey F G 1976 *At. Data Nucl. Data Tables* **17** 1
Piekarewicz J 2011 *Phys. Rev.* C **83** 034319
Pizzone R G *et al* 2005 *Phys. Rev.* C **71** 058801
Pizzone R G *et al* 2009 *Phys. Rev.* C **80** 025807
Pizzone R G *et al* 2011 *Phys. Rev.* C **83** 045801
Pizzone R G *et al* 2013 *Phys. Rev.* C **87** 025805
Perelomov A M *et al* 1966 *ZhETF* **51** 309
Pramanik U D *et al* 2003 *Phys. Lett.* B **551** 63
Pringle D M *et al* 1986 *Nucl. Instrum. Methods Phys. Res.* A **245** 230
Pushkin A *et al* 1996 *J. Phys. G: Nucl. Part. Phys.* **22** L95
Redder A *et al* 1982 *Z. Phys.* A **305** 32
Reifarth R 2013 The s- and r-process for the synthesis of heavy elements *Erice School/Workshop on Neutrino Astrophysics (Erica, Italy, September 2013)*
Rhoades-Brown M *et al* 1980 *Phys. Rev.* C **21** 2417
Rhoades-Brown M *et al* 1980 *Phys. Rev.* C **21** 2436
Rinollo A *et al* 2005 *Nucl. Phys.* A **758** 146
Rolfs C and Kavenagh R W 1986 *Nucl. Phys.* A **455** 179
Rolfs C and Rodney W S 1988 *Cauldrons in the Cosmos* (Chicago, IL: University of Chicago Press)
Romano S *et al* 2006 *Eur. Phys.* A **27** 221
Rossi D M *et al* 2013 *Phys. Rev. Lett.* **111** 242503
Rupak G and Higa R 2011 *Phys. Rev. Lett.* **106** 222501
Schardt A *et al* 1952 *Phys. Rev.* **86** 527
Schmidt K-H *et al* 1994 *Phys. Lett.* B **325** 313
Schroeder U *et al* 1987 *Nucl. Phys.* A **467** 240
Schümann F *et al* 2003 *Phys. Rev. Lett.* **90** 232501
Schümann F *et al* 2006 *Phys. Rev.* C **73** 015806
Segel R E *et al* 1965 *Phys. Rev.* **139** 818
Sergi M L *et al* 2010 *Phys. Rev.* C **82** 032801
Shapiro I S 1967a *Usp. Fiz. Nauk* **92** 549
Shapiro I S 1967b Interaction of high-energy particles with nuclei *International School of Physics 'Enrico Fermi', Course 38* ed E O Ericson (New York: Academic) p 210
Shapiro I S 1968 *Sov. Phys.—Usp.* **10** 515
Shimoura S *et al* 1995 *Phys. Lett.* B **348** 29
Smith M S and Rhem K E 2001 *Annu. Rev. Nucl. Part. Sci.* **51** 91
Sobotka L G *et al* 2013 *Phys. Rev.* C **87** 05432
Spitaleri C *et al* 1999 *Phys. Rev.* C **60** 055802
Spitaleri C *et al* 2000 *Eur. Phys. J.* A **7** 181
Spitaleri C *et al* 2001 *Phys. Rev.* C **63** 055801
Spitaleri C *et al* 2004 *Phys. Rev.* C **69** 055806
Spitaleri C *et al* 2011 *Phys. At. Nuclei* **74** 1763
Starrfield S *et al* 2000 *Astrophys. J. Suppl.* **127** 485
Strieder F *et al* 2001 *Naturwissenschaften* **88** 461
Summers N and Nunes F 2008 *Phys. Rev.* C **78** 011601
Summers N and Nunes F 2008 *Phys. Rev.* C **78** 069908 (erratum)
Suzuki Y *et al* 1990 *Prog. Theor. Phys.* **83** 180
Tabacaru G *et al* 2006 *Phys. Rev.* C **73** 025808
Tang X *et al* 2003 *Phys. Rev.* C **67** 015804
Tang X *et al* 2004 *Phys. Rev.* C **69** 055807
Tarasov O 2012 *LISE++code* private communication
Thompson I J 1988 *Comput. Phys. Rep.* **7** 167
Timofeyuk N K 1998 *Nucl. Phys.* A **632** 19
Timofeyuk N K *et al* 2003 *Phys. Rev. Lett.* **91** 232501
Timofeyuk N K 2011 *Phys. Rev.* C **84** 054313
Togano Y *et al* 2005 *Nucl. Phys.* A **758** 182
Togano Y *et al* 2011 *J. Phys.: Conf. Ser.* **312** 042025
Trache L *et al* 1998 *Phys. Rev.* C **58** 2715
Trache L *et al* 2002 *Phys. Rev.* C **66** 035801
Trache L *et al* 2003 *Phys. Rev.* C **67** 062801
Trache L *et al* 2004 *Phys. Rev.* C **69** 032802(R)
Tribble R E *et al* 1991 *Nucl. Instrum. Methods Phys. Res.* A **285** 441
Tumino A *et al* 2003 *Phys. Rev.* C **67** 065803
Tumino A *et al* 2004 *Prog. Theor. Phys. Suppl.* **154** 341
Tumino A *et al* 2005 *Eur. Phys. J.* A **25** 649
Tumino A *et al* 2006 *Eur. Phys. J.* A **27** 243
Tumino A *et al* 2007 *Phys. Rev. Lett.* **98** 252502
Tumino A *et al* 2008 *Phys. Rev.* C **78** 015804
Tumino A *et al* 2011 *Phys. Lett.* B **705** 546
Typel S and Baur G 2001 *Phys. Rev.* C **64** 024601
Typel S and Baur G 2003 *Ann. Phys.* **305** 228
Valkovic V *et al* 1971 *Nucl. Phys.* A **166** 547
Vernotte J *et al* 1994 *Nucl. Phys.* A **571** 1
Weizsäcker C F von 1937 *Phys. Z.* **38** 176
Wen Q *et al* 2008 *Phys. Rev.* C **78** 035805
Wieland O *et al* 2009 *Phys. Rev. Lett.* **102** 092502
Wiescher M and Kettner K U 1982 *Astrophys. J.* **263** 891
Wiescher M *et al* 1989 *Astrophys. J.* **343** 352
Williams R D and Koonin S E 1981 *Phys. Rev.* C **23** 2773
Winther A and Alder K 1979 *Nucl. Phys.* A **319** 518
Xu H M *et al* 1994 *Phys. Rev. Lett.* **73** 2027
Xu Y *et al* 2013 *Nucl. Phys.* A **918** 61
Zadro M *et al* 1989 *Phys. Rev.* C **40** 181
Zyskind J L and Parker P D 1979 *Nucl. Phys.* A **320** 404